

# Dynamics of an Arched Magnetically-Twisted Current-Carrying Plasma

Thesis by  
Pakorn Wongwaitayakornkul

In Partial Fulfillment of the Requirements for the  
Degree of  
Doctor of Philosophy

The logo for the California Institute of Technology (Caltech), featuring the word "Caltech" in a bold, orange, sans-serif font.

CALIFORNIA INSTITUTE OF TECHNOLOGY  
Pasadena, California

2020  
Defended February 28, 2020

© 2020

Pakorn Wongwaitayakornkul  
ORCID: 0000-0001-7455-8582

All rights reserved

## ACKNOWLEDGEMENTS

I am incredibly grateful for my wonderful experience at Caltech. The work in this dissertation would not have been possible without the support from the people I have met here. I would like to dedicate this section to thanking them.

I would like to thank Paul Bellan for giving me an opportunity to join the group. He is patient and accessible. His broad expertise helped me tackle problems from several perspectives and his delightful stories always kept our group entertained. I am very fortunate to have worked with him.

I would also like to thank Lynne Hillenbrand, Stevan Nadj-Perge, and Gregg Hallinan for agreeing to be a part of my doctoral dissertation committee. I appreciate their scientific insights and the time they spent on reading the thesis and showing up for the defense.

I thank the Bellan plasma group for providing a great working community. Everyone helped each other and collaborated well, resulting in a positively productive environment. I thank Magnus for his cheerful attitude and excitement for doing research. I appreciate the time in Los Alamos, at conferences, and around pool tables. I thank Young for our many valuable discussions during lunch and Ryan for keeping us on schedule. I thank the seniors in the lab, Bao, Xiang, Vernon, Byonghoon, KB, and Amelia, for their constructive guidance, and the juniors, Yi, Yang, and Andre, for quickly learning the lab work. I thank Connie for the abundant snack supply and Dave for his engineering mastery.

I thank Nicha, Ashish, Karen, and Kosta for many years of joyous gym sessions and outdoor explorations. In addition, I thank Zhewei, Jeff, Ameera, Viv, Sean Min-feng, Bassam, Linhan, Jen, Corwin, and the amazing people from the Caltech Alpine Club for filling my PhD memories with countless adventures of the western U.S.'s finest vertical world.

I thank Sumit, Forte, Silvia, Sunghyuk, Jim, Cathy, Di, Remy, and many others from the Caltech Badminton Club for their friendship, boba, boardgame, and quality badminton games.

I thank the current generation Thai community — Kaew, Pai, Whay, Fah, Fa, Nut, Pond, and Por — for making this place feels like home. I also thank P'Ploy, P'Tee, and P'Tara for helping me get started at this place.

Ultimately, I thank my parents for their unlimited and continuous support.

## ABSTRACT

Experimental and numerical studies of a dense magnetically-twisted plasma and their applications to solar plasmas are the subject of this dissertation. In the corona, plasma lies in a low-beta, high Lundquist number regime, meaning that it is magnetically dominated and the magnetic fields are well frozen into the plasma. Understanding the dynamics of these plasmas help us predict and prevent damage from future catastrophic solar eruption events. In situ measurements from satellite and ground-based observation provide limited information that is not controllable nor reproducible. The research objective in this thesis is to produce a miniature-scaled plasma with the same dimensionless parameters as the space plasmas. Along with numerical simulation, theoretical study, and observational data, the laboratory plasma can give novel insights into the physics of solar plasma.

First, an experimental dip on a flux rope, previously thought to be caused by a kink instability, is discussed and explained. We find that the apex cusp is in fact caused by the differential acceleration due to a non-uniform density. The pileup density results from a nonlinear interaction of the neutral gas. This result introduces a new method to impose effective gravity on the arched plasma and explains the suppression of kink instability. Second, a model for a morphology of CME and its shock driving mechanism is investigated. In the experiment, the chamber is prefilled with neutral gas, leading to an observation of a density cavity. Because the plasma is flux conserving, injecting a current into the plasma induces an opposite eddy current in front of the flux rope. The two opposing currents repel and leave a low density region in between. This feature is often observed in CMEs. We propose this mechanism to be the model of the CME 3-part structure formation. The opposite eddy current acts as a current piston driving an MHD perturbation/shock, which is often observed on the sun as an EUV wave.

A Magnetic Rayleigh-Taylor instability has been observed in the arched plasma loop. For the first time, the magnetic effect of the MRT instability is shown when the wavelength observed depends on the initial magnetic field initially injected into the system. In several years of working with the experiment in the Bellan plasma group, I designed and constructed several diagnostics, such as Langmuir probes, magnetic probes, and a coded aperture camera. Together with fast multi-images camera and spectroscopy techniques, plasma parameters are measured and compared to verify the models.

The 3D MHD numerical simulation was performed using the supercomputer from the Los Alamos National Laboratory. The initial condition and injection routines were modified to appropriately replicate the experiment. The code has been significant in improving our understanding of the physical phenomena we observed in the experiment. We attain a proper initial distribution of the mass density and the initial and injected current density. In addition to simulating an arched flux rope experiment, we use this tool to replicate MHD instabilities detected in the astrophysical jet experiment. Specifically, both a sausage-to-kink and kink-to-Rayleigh-Taylor instability have been reproduced using the numerical simulation. Each process thins the plasma current channel to be below the ion skin depth. The kinetic effect then gives rise to magnetic reconnection. An anomalous resistivity is added to simulate this process.

In conclusion, an interdisciplinary approach, through experimental, numerical, observational, and theoretical studies, is presented. It improves our understanding of the underlying mechanism for solar eruptions. A magnetically-twisted current-carrying flux rope, once formed, could exhibit dips and cavity. Its evolution could drive shock and instabilities, which ultimately cause particle acceleration.

## PUBLISHED CONTENT AND CONTRIBUTIONS

- [1] Pakorn Wongwaitayakornkul, Hui Li, and Paul M Bellan. “3D Numerical Simulation of Kink-Driven Rayleigh-Taylor Instability Leading to Fast Magnetic Reconnection”. In: *Under Review* (2020).  
P.W. performed the simulation and wrote the manuscript.
- [2] Byonghoon Seo, Pakorn Wongwaitayakornkul, Magnus A Haw, Ryan S Marshall, Hui Li, and Paul M Bellan. “Determination of a macro- to micro-scale progression leading to a magnetized plasma disruption”. In: *Physics of Plasmas* 27.2 (2020), p. 022109. DOI: <https://doi.org/10.1063/1.5140348>.  
P.W. performed the simulation, and wrote and discussed the manuscript.
- [3] Yang Zhang, Pakorn Wongwaitayakornkul, and Paul M Bellan. “Magnetic Rayleigh-Taylor Instability in an Experiment Simulating a Solar Loop”. In: *The Astrophysical Journal Letters* 889.2 (2020), p. L32. DOI: <https://doi.org/10.3847/2041-8213/ab6b2d>.  
P.W. performed the initial stage of the experiment and discussed the manuscript.
- [4] Pakorn Wongwaitayakornkul, Magnus A Haw, Hui Li, and Paul M Bellan. “Magnetically Induced Current Piston for Generating Extreme-ultraviolet Fronts in the Solar Corona”. In: *The Astrophysical Journal* 874.2 (2019), p. 137. DOI: <https://doi.org/10.3847/1538-4357/ab09f2>.  
P.W. performed the experiment and simulation and wrote the manuscript.
- [5] Magnus A Haw, Pakorn Wongwaitayakornkul, Hui Li, and Paul M Bellan. “Reverse Current Model for Coronal Mass Ejection Cavity Formation”. In: *The Astrophysical Journal Letters* 862.2 (2018), p. L15. DOI: <https://doi.org/10.3847/2041-8213/aad33c>.  
P.W. performed the experiment and simulation and wrote the manuscript.
- [6] Pakorn Wongwaitayakornkul, Magnus A Haw, Hui Li, Shengtai Li, and Paul M Bellan. “Apex Dips of Experimental Flux Ropes: Helix or Cusp?”. In: *The Astrophysical Journal* 848.2 (2017), p. 89. DOI: <https://doi.org/10.3847/1538-4357/aa8990>.  
P.W. performed the experiment and simulation and wrote the manuscript.

## TABLE OF CONTENTS

Acknowledgements . . . . .	iii
Abstract . . . . .	iv
Published Content and Contributions . . . . .	vi
Table of Contents . . . . .	vii
List of Illustrations . . . . .	ix
List of Tables . . . . .	xvi
Chapter I: Introduction . . . . .	1
1.1 Plasma Physics . . . . .	2
1.2 Solar Physics . . . . .	8
Chapter II: Laboratory Plasma . . . . .	10
2.1 Single Loop Experiment . . . . .	10
2.2 Astrophysical Jet Experiment . . . . .	11
2.3 Diagnostics . . . . .	12
Chapter III: 3D Magnetohydrodynamics Simulation . . . . .	15
3.1 Normalization . . . . .	15
3.2 Arched Configuration . . . . .	16
3.3 Axisymmetric Configuration . . . . .	19
Chapter IV: Apex Dips of Experimental Flux Ropes . . . . .	20
4.1 Introduction . . . . .	20
4.2 Experimental Apparatus . . . . .	22
4.3 Theory . . . . .	25
4.4 Experimental Results . . . . .	27
4.5 MHD Simulation of the Apex Dip . . . . .	28
4.6 Discussion . . . . .	31
Chapter V: Reverse Current Model for Coronal Mass Ejection Cavity Formation . . . . .	35
5.1 Introduction . . . . .	36
5.2 Prefilled Single Loop Experiment . . . . .	37
5.3 Simulation . . . . .	39
5.4 Snowplow Model for Reverse Current . . . . .	42
5.5 Scaling to CMEs . . . . .	45
Chapter VI: Magnetically Induced Current Piston for Generating Extreme-Ultraviolet Fronts in the Solar Corona . . . . .	47
6.1 Introduction . . . . .	48
6.2 Theory . . . . .	49
6.3 Experimental Contour Reconstruction . . . . .	56
6.4 MHD Numerical Simulation . . . . .	58
6.5 Discussion . . . . .	63
Chapter VII: Magnetic Rayleigh-Taylor Instability in an Experiment Simulating a Solar Loop . . . . .	67

7.1 Introduction . . . . .	67
7.2 Experimental Setup . . . . .	69
7.3 Result . . . . .	69
Chapter VIII: Simulation of a sausage-like pinching to kink instability progression leading to a magnetized plasma disruption . . . . .	71
8.1 Introduction . . . . .	72
8.2 Experimental Observation of Sausage-like to Kink Instability . . . . .	73
8.3 Simulation . . . . .	75
Chapter IX: 3D Numerical Simulation of Kink-Driven Rayleigh-Taylor Instability Leading to Fast Magnetic Reconnection . . . . .	79
9.1 Introduction . . . . .	79
9.2 3D Resistive MHD Simulation . . . . .	83
9.3 Conditions for KDRT . . . . .	85
9.4 Effect on $\Phi^2$ . . . . .	87
9.5 Electron Acceleration . . . . .	87
9.6 Discussion . . . . .	91
Chapter X: Summary . . . . .	93
10.1 Future Direction . . . . .	93
Bibliography . . . . .	95
Appendix A: Additional material on dips on flux rope . . . . .	110
Appendix B: Additional material on diamagnetic cavity . . . . .	112

## LIST OF ILLUSTRATIONS

<i>Number</i>	<i>Page</i>
1.1 Illustration for different type of MHD instability . . . . .	8
1.2 Image of a solar prominence and a CME . . . . .	9
1.3 Outline of the topics in the thesis. The associated chapters are labelled in roman numerals. . . . .	9
2.1 Diagram for Caltech Single Loop Experiment . . . . .	11
2.2 Evolution of single loop N <sub>2</sub> plasma without the initially prefilled neutral (#5594). Times after plasma breakdown are labelled in white. . . . .	11
2.3 Evolution of single loop argon plasma with the initially prefilled hydrogen neutral gas. The image series are superimposed from 2 shots with the same experimental settings: with (#3221; red) and without (#3222; cyan) 656 nm filter (H $\alpha$ ). Times after breakdown are labelled in white. . . . .	12
2.4 Diagram for Caltech Jet Experiment . . . . .	13
3.1 Plot of the initial conditions for the simulation. Source currents for the background magnetic field consist of 10 thin loops arranged in a semi-circle (red), B-field lines are shown in blue. The high density plasma wall boundary is shown in black. . . . .	17
3.2 Illustration of spatial profile of the current injection. Each red circle represents a thin circular current loop. (a) The 3 dimensional view showing all 110 loops. (b) The 2 dimensional cross section in $xz$ - plane. (c) The 2 dimensional cross section in $yz$ -plane. The spatial units are in centimeters. . . . .	18
4.1 (a) Side view of lab experiment flux rope showing dip at apex, (b) top view of lab flux rope showing no evidence of helical shape, (c) sketch of side view for helix interpretation, (d) sketch of side view for downward cusp interpretation . . . . .	21
4.2 Schematic diagram of the experimental setup showing cones of neu- tral gas (blue) ejected from holes in electrodes (copper), plasma loop (red), solenoids (green) for providing background magnetic field, and gas injection system. . . . .	23

4.3	Comparison of white light images for arched flux rope experiments with their gas supply. Only experiments with fast-gas valves (FGV) at both footpoints observe dip feature . . . . .	24
4.4	Density profiles for (a) direct superposition of two gas cone profiles and (b) modeled gas profile with finite neutral mean free path (Eq. 4.2)	26
4.5	Photograph of the loop at $1.5 \mu s$ after breakdown. The white dashes mark the bright feature at the loop's apex and pileup cone at the midplane . . . . .	28
4.6	Plot shows the evolution of two different initial density profiles. (a) Standard initial conditions with two colliding cones of gas supplied by nozzles in electrodes. (b) Non-standard conditions with uniform background gas supplied from sources on opposite side of chamber. Without the gas cones from the nozzles, the apex dip feature disappears	29
4.7	Comparison of dip shape for two different gas outputs. Loop axis is manually traced with white lines to highlight differences (Gas = H) .	29
4.8	(top) Plot of vertically integrated pixel values. (bottom) Superimposed images of a shot with higher gas output on the right footpoint (red) and a shot with higher gas output on the left footpoint (cyan) (Gas = He) . . . . .	30
4.9	Comparison of the cusp shape between experiment (left) and simulation (right) . . . . .	31
4.10	Evolution of the loop apex position in 3 stages: (i) the minor radius undergoes pinching before expansion (ii) the loop collides with the pileup region temporarily slowing down (iii) the magnetic curvature forces of the cusp re-accelerate the apex to a terminal velocity . . . .	32
4.11	Magnetic tension forces ( $\mathbf{B} \cdot \nabla \mathbf{B}$ , arrows) plotted for an apex dip of a thin flux rope (blue line). Central cusp area has strong vertical magnetic forces because of the high curvature . . . . .	34

5.1	(a) Image sequence of the three-part CME captured by LASCO-C3 on 2011 October 4. This sequence shows a nearly edge on view of the current channel instead of the perpendicular views shown from the experiment. (b) Image sequence of composite multiwavelength fast camera images of laboratory experiment. Each image consists of two bandwidths: filtered $H\alpha$ in blue (H-dominated) and visible light in red (Ar-dominated). (c) Cross-sectional plots of simulated current density in the horizontal direction ( $J_y$ ) showing the propagation of the main current (red) and an induced reverse current layer (blue). For each case, the height evolution of leading edge/reverse current (blue), core/current channel (red) and cavity width/separation (yellow) are plotted in the last column. . . . .	37
5.2	(a) Schematic diagram of the experimental setup showing the primary current channel (red), the induced reverse current layer (blue), electrodes (copper), solenoid (green), magnetic probe array (yellow), and Langmuir probe (grey). (b) Plot of density from Langmuir probe at three locations shows formation of density cavity . . . . .	38
5.3	(Left) Calculated $J_y(t)$ profiles at three locations show the distribution and propagation of the reverse current and the current channel in the experiment. Inset shows reverse currents in more detail. (Right) The equivalent plot of $J_y$ obtained from the simulation at 3 locations analogous to those in the experiment. . . . .	40
5.4	Illustration of the model. The current $I$ is in the $+y$ direction in the main current channel (red) and in the $-y$ direction in the reverse current shell (blue). The reverse current shell has thickness $\delta$ and expands radially forming a cavity region between $a$ and $b(t)$ . The plot shows the radial dependence of both the normalized axial field ( $B_y$ , blue) and normalized azimuthal field ( $B_\phi$ , red). The table lists radial ranges with their corresponding magnetic fields. . . . .	43

5.5	Comparison of the cavity width for all the different scenarios, taken from the right column of Figure 5.1. Color: (blue) Reverse current, (red) current channel, (yellow) separation, and (black) theory ( $\bar{b}(t) + \bar{\delta}/2$ ). Style: (o) CME on 2011 October 4, (x) laboratory, and ( $\diamond$ ) simulation. In this plot, the separation is defined as the center-to-center distance between the main current and the reverse current layer. Vertical errorbars are $\pm 0.5$ for all traces. The black line represents a numerical solution to Eq. 5.8 with $\bar{\delta} = 0.25$ and $\bar{I} = [\bar{I}_0 + 20 \sin(\pi \bar{t}/60)]$ .	46
6.1	Classification of previous literature by feature speed and driving timescale. The trend of the proposed theories goes from wave, to shock, then to pseudo-wave, and finally to hybrid model. $v_{ms}$ represents the local wave speed. . . . .	49
6.2	Illustration for the analytic model of the current layer generation and propagation. Here, we extend the model so the thickness of current layer $\delta$ and the thickness of plasma mass $\Delta$ could be different. . . . .	52
6.3	The left dark background halves are the image sequence of multi-wavelength fast camera images of the experiment, composing of two band passes: visible (red) and filtered $H_\alpha$ (cyan). The right white background halves are the cross-sectional plots of simulated current density in horizontal direction ( $J_y$ ) of the ideal 3D MHD simulation. The colorbar indicates the value of $J_y$ . In both cases, the snapshots are taken at the same time (labelled in white) after the plasma breakdown. The simulated images are taken at different times from Haw et al. [53]. The temporal and spatial quantities are scaled into solar environment as labelled in the parentheses . . . . .	55
6.4	(a) and (c) show the experimental sample time series of the magnetic and Langmuir probes (solid line) with the reconstructed fitted profiles (dashed line). (b) and (d) plot the space-time profiles of the dashed line of $\bar{J}_y$ and $\bar{\rho}$ in (a) and (c). The normalized parameters for the experiment are $a = 1.1$ cm, $v_A = 0.43$ km s $^{-1}$ , $\tau = a/v_A = 130$ $\mu$ s, $\rho_0 = 9.1 \times 10^{-9}$ kg m $^{-3}$ , $B_0 = 0.46$ G and $J_0 = \sqrt{\rho_0/\mu_0}/\tau = 3.3$ kA m $^{-2}$ . These parameters can be scaled to the solar context using $a = 6.25$ Mm, $v_A = 41.7$ km s $^{-1}$ , $\tau = 135$ s, $\rho_0 = 7.0 \times 10^{-12}$ kg m $^{-3}$ , $B_0 = 1.2$ G, and $J_0 = 16.7$ $\mu$ A m $^{-2}$ . The method for scaling to the solar context is given in Chapter 5. . . . .	56
6.5	Evolution of apex locations of the simulation during the three stages . . . . .	60

6.6	Time evolution of 4 quantities from the MHD simulation in $z$ along the apex. The plots consist of (a) current density, (b) temperature, (c) mass density, and (d) flow speed. For coronal environment, the normalization quantities are $a = 6.25 \text{ Mm} \sim 0.01R_{\odot}$ , $v_A = 41.7 \text{ km s}^{-1}$ , $\tau = a/v_A = 135 \text{ s}$ , $\rho_0 = 7.0 \times 10^{-12} \text{ kg m}^{-3}$ , $B_0 = 1.2 \text{ G}$ , $J_0 = \sqrt{\rho_0/\mu_0}/\tau = 16.7 \text{ } \mu\text{A m}^{-2}$ , and $T_0 = m_H v_A^2/2\kappa = 9.7 \times 10^4 \text{ K}$ ( $m_H = 1 \text{ u}$ ). . . . .	61
6.7	The plot tracks the transition of 4 variables in the MHD simulation: flow velocity in shock frame $\bar{v}'_z = \bar{v}_s - \bar{v}_z$ , mass density $\bar{\rho}$ , pressure $\bar{p}$ , and tangential magnetic field $\bar{B}_t$ across the shock. The $\bar{z}$ range and time for this plot are shown as the magenta line in Fig. 6.6. The background colors represent the three regions in velocity phase space: (i) $v'_z > v_{ms}$ , (ii) $v_{ms} > v'_z > v_A$ , and (iii) $v'_z < v_A$ . The two vertical dash lines indicate the boundaries of the shock. Each parameter is normalized to their upstream value. The expected compression ratios are labelled as $Y$ , $X$ , and $X^{-1}$ on the downstream boundary. $\bar{z}_s$ is the location of shock center and $\bar{\delta}$ is the shock thickness. . . . .	62
6.8	Comparison of (left) the low coronal EUV ( $193 \text{ \AA}$ ) shock wave observed with AIA/SDO on 2010 June 13 (adapted from Ma et al. [88]) and (right) visible emission from the Caltech experiment in reverse grayscale. . . . .	65
6.9	Contour of the compression ratio $X(\mathcal{M}, \beta)$ as determined by Eq. 6.7. The compression ratio of the May 19 <sup>th</sup> , 2007 event in Muhr et al. [100] $X = 1.27$ is plotted as a solid line. The two points corresponding to $\beta = 0.1$ and 136 along $X = 1.27$ are plotted with green and blue markers. The value used in the simulation of this work is plotted with a red marker. . . . .	66
7.1	MRTI in a time series images of $\text{N}_2$ plasma loop evolution. . . . .	69
7.2	Time series images of $\text{N}_2$ plasma loop evolution (upper shot# 7385 and $V_b = 30 \text{ V}$ , lower shot# 7281 and $V_b = 60 \text{ V}$ ). Images were taken by Yang Zhang. . . . .	70
8.1	Time series of a nitrogen plasma shot taken by the fast movie camera. Images were taken by Byonghoon Seo. . . . .	73

8.2	Time sequence of current density iso-surfaces obtained from simulation # 471. The two back planes at each time respectively show cross-sections of the current density at $x = 0$ and at $y = 0$ . The surface plots contain three iso-surfaces at levels 0.19 (blue), 0.32 (green), and 0.41 (red) of the maximum current density at each time.	75
8.3	Time-dependent radial force obtained from numerical simulation. Initially the flux tube is not in equilibrium so the direction of the radial force at $2.3 \mu\text{s}$ is inward. By pinching the flux tube, a temporary radial force balance is established at $2.7 \mu\text{s}$ . Sausage instability occurs at $3.3 \mu\text{s}$ .	77
8.4	Time sequence of $\bar{J}$ , $\bar{\rho}$ , $\bar{B}$ , and $v_d/v_A$ in the $y$ - $z$ ( $x = 0$ ) plane obtained from simulation # 471. The $\bar{J}$ plots are the same as the back right planes in Fig. 5 but are shown with continuous color contours. The flux rope becomes sausage unstable at $3.31 \mu\text{s}$ and then kink unstable so the flux rope kinks into and out of the page after $3.63 \mu\text{s}$ . The regions where the flux rope passes through this plane are indicated by red circles. The ratio $v_d/v_A$ becomes large at the locations indicated by yellow arrows at $3.80 \mu\text{s}$ because $\bar{J}$ becomes large at these locations as indicated by green arrows.	78
9.1	The evolution of KDRT instability development on argon plasma jet (shot#11,225) shows an inner ripple RTI on the inner side of a helical kink. The white label indicates the time after the plasma breakdown.	83
9.2	Simulated KDRT at three different timesteps. $\tau_A$ is the Alfvén time of the simulation. The isosurfaces represent $\{0.2\rho_0, 0.3\rho_0, 0.4\rho_0\}$ with {blue,green,red} respectively.	85
9.3	Isosurfaces snapshot of density in two cases: (a) with uniform $B_z = 0.3$ and (b) with $B_z = 0.3$ only inside the flux rope ( $r < a$ ). Both cases are taken at the same time $t = 1.1\tau_A$ . The colors {blue,green,red} indicate the levels {0.5,0.7,0.9} of the maximum density of that time frame accordingly. The planes show cross-sectional contour of the density in the midplane.	86

9.4	The table shows the two limits of the instability: (a) $\Phi^2 \gg 1$ and (b) $\Phi^2 \ll 1$ . The instability is shown in the Illustration column, where the shape of the instability is calculated analytically. Secondly, the different regimes are captured with fast camera. The right hand column shows the 3D numerical simulation. The numerical plots are isosurfaces of density. The figures in Illustration and Experimental Image columns are adapted from Zhai and Bellan [166]. The Numerical Simulation column is the result of this work. . . . .	88
9.5	(a) Isosurfaces of $E_{  } = \eta \mathbf{J} \cdot \mathbf{B} / B$ . The color {green,blue,red} represents the level {0.1,0.4,0.6} of the maximum value of this time step respectively. The gray lines shows 100 random particle trajectories. The red lines shows the trajectory of the highly accelerated particles. The cube indicates the domain of the initial position. (b) Distribution of the test particles initial and final energies. . . . .	90
A.1	Shapes of the flux rope with the initially prefilled neutral gas of various types. . . . .	110
A.2	Images show different shots of (Ar H) plasma with varying gas injection from the footpoints (#3749-3753). As a result, a dip location on the flux rope is differed. The labels are fast-gas-valve voltages, corresponding to amounts of argon gas injection from the footpoints. White dashed lines indicate the locations of the dip. . . . .	111
A.3	Time sequences of illuminated neutral pileups and their corresponding flux rope with various number of dips: (a) 0, (b) 1, and (c) 2. . . . .	111
B.1	False color images of three cases with different strength of the strapping fields at $t = 10.5 \mu s$ after the breakdown: (a) $B_s = 0$ G, (b) $B_s = 375$ G, and (c) $B_s = 750$ G. The cavity widths are labelled with black lines and the strapping coils are contoured with white lines . . .	112

## LIST OF TABLES

<i>Number</i>		<i>Page</i>
1.1	Lists of parameters in laboratory and corona . . . . .	7
4.1	Parameters for Density Pileup . . . . .	25
4.2	Dimensionless scaling of Caltech parameters to solar loops. $g$ here refers to an actual gravitational acceleration not the effective one. . .	33
6.1	Prediction from this model for properties listed in Long et al. [86]. . .	64

*Chapter 1*

## INTRODUCTION

One of the most significant problems in solar physics is how stationary prominences erupt into Coronal Mass Ejections (CMEs) and accelerate high energy particles. Generally, the solar prominence — a large arched structure on the surface of the sun — stays on the surface for a long time (weeks to months). A CME is a large release of plasma ( $\sim 10^{12}$  kg) and associated magnetic field. It happens quite often, i.e., of the order of 0.2-3 CMEs per day. CMEs are thought to be associated with Solar Energetic Particles (SEPs), which pose a danger to spacecraft, aircraft communications, and the electrical grid. The mechanism that describes the whole process is still debated. Traditionally, theories have been developed from observations and verified via numerical simulation. In the Caltech plasma laboratory, we use a pulsed-power plasma experiment to simulate the plasmas that are observed in space. The comparison is made possible by the equations governing the dynamics of the plasma, i.e., the magnetohydrodynamics (MHD) description. The system of MHD equations has no intrinsic scale and so can be used to explain events in plasma systems having vastly different scales. The control and reproducibility of the plasma shot and possibility of in situ diagnostics makes the laboratory plasma experiment an appealing instrument to research plasma phenomena.

This dissertation includes the work that I have done in the Bellan plasma group at Caltech in my graduate school years. The works, reported in Chapters 4 – 9, were done in collaboration with multiple authors. My contributions are specified at the beginning of each chapter. In Chapter 1, I will briefly go over the basic concepts in plasma physics that will be relevant to understanding this thesis, i.e., Debye shielding, magnetohydrodynamics, frozen-in flux, dimensionless equations, plasma instabilities, and magnetic reconnection. Then, I will provide examples of phenomena observed on the sun that could be described by our understanding of plasma physics. The tools to merge these basic ideas into the actual observable phenomena are presented in Chapters 2 and 3. The dimensionless nature of the MHD description, covered in Chapter 1, allows us to study the physics of the plasma over vastly different scales. This concept permits one to simulate events on the sun in the laboratory experiments at Caltech (Ch. 2) and using 3-dimensional numerical simulation (Ch. 3).

Solar prominences are commonly believed to have inhomogeneous density along the axis and that the highest density is localized near the apex. We explore this feature experimentally in Chapter 4 using the Caltech single loop experiment. The density inhomogeneity plays an important role in the dynamics of the arched flux rope and greatly affects the condition that causes eruption. Once erupted, the plasma is ejected from the sun's surface. A coronal mass ejection has a three-part structure and produces a preceding shock wave. By adding plasma density in the background in the Caltech single-loop experiment, Chapter 5 shows the evidence for a plasma density cavity from current injection. Two possible causes for SEPs are shocks and plasma instabilities; the two phenomena will be discussed in the following chapters. Chapter 6 looks into the formation mechanism of the shock driven by the expanding flux rope. When the plasma leaves the sun's surface, the line-tied magnetic field lines at the footpoint go through magnetic reconnection before the detachment occurs and the plasma launches into space. During this process, when the magnetic field changes topology, charged particles are accelerated to high energy. The magnetic reconnection happens at the micro scale of ion-skin depth; however, at the macro scale, the plasma is governed by MHD equations. There is a path that connects the two phenomena. The following chapters present possible mechanisms observed in both the experiment and simulation of the MHD process that could lead to magnetic reconnection. Chapter 7 documents the first observation of magnetic Rayleigh-Taylor instability on single loop experiment due to the hoop force. Chapter 8 presents a numerical simulation for sausage-like pinching to kink instability progression. Chapter 9 describes the numerical simulation for the kink-driven Rayleigh-Taylor instability occurring when the Caltech plasma jet disrupts from the electrode. Chapter 10 provides the summary of the thesis and the direction for future research.

## 1.1 Plasma Physics

Plasma is an ionized gas that exhibits collective behavior. The ionized gas is composed of electrons, ions, and neutrals, and responds to electromagnetic fields. Researchers started investigation of this substance in the 1920s in the context of ionospheric plasma for sending short-wave radio and gaseous electron tubes for constructing electronic switches. Since then, plasma physics has been researched in various contexts both terrestrial (e.g., thermonuclear fusion and plasma processing) and in space (e.g., solar corona and astrophysical plasma). A comprehensive discussion of plasma physics can be found in Ref. [12]. Here we briefly cover some

topics that will be useful to follow the thesis work.

### Debye Shielding

Many of the plasmas we studied are considered quasi-neutral, meaning that the total number of electrons and ions are approximately equal. If a finite electric field was to be imposed to the plasma, the electrons and ions, which are free to move around, redistribute themselves to cancel out the external electric field. The scale length associated with this shielding is called the Debye length  $\lambda_D$ .

Suppose that the quasi-neutral plasma is in thermal equilibrium and the two plasma species are distributed according to the Maxwell-Boltzmann law,

$$n_\sigma = n_0 \exp\left(-\frac{q_\sigma \phi}{\kappa T}\right), \quad (1.1)$$

where  $\phi$  is the electrostatic potential,  $k_B$  is the Boltzmann's constant,  $q_\sigma$  is the charge of the species  $\sigma$ , and  $T$  is the plasma temperature. A positively charged test ion of charge  $q_T$  is placed inside the plasma. The plasma potential obeys Poisson's equation:

$$\nabla^2 \phi = -\frac{1}{\epsilon_0} \left[ q_T \delta(\mathbf{r}) + \sum_{\sigma} n_\sigma(\mathbf{r}) q_\sigma \right], \quad (1.2)$$

where  $\delta$  is the Dirac delta function. Solving the Equation 1.2, one arrives at

$$\phi(\mathbf{r}) = \frac{q_T}{4\pi\epsilon_0 r} e^{-r/\lambda_D}, \quad (1.3)$$

where the Debye length is defined by  $\frac{1}{\lambda_D^2} = \sum_{\sigma} \frac{1}{\lambda_{\sigma}^2}$  and  $\lambda_{\sigma}^2 = \frac{\epsilon_0 \kappa T}{n_{\sigma 0} q_{\sigma}^2}$ . The plasma potential goes to zero exponentially and  $\lambda_D$  regulates the decay profile.

### Models of Plasma Dynamics

The most elementary way to model the plasma is to simulate each particle's motion individually. As the particles move, the electromagnetic fields are updated using Maxwell's equations. The new fields then cause the particles to move via the Lorentz equation. The interrelation between the two calculations can describe all the dynamics of plasma. However, the number of particles involved is generally too large for a current computer to keep track of every individual particle. We often opt to use a simpler model for plasma dynamics. In this section, we will go over three

descriptions of plasma dynamics, from the most complex to the simplest, namely kinetic, two-fluids, and magnetohydrodynamics (MHD).

### **Kinetic**

A statistical approach that focuses on the distribution function of the plasma is instead employed. At a given moment  $t$ , one could consider grouping all the particles with the position between  $x$  and  $x + dx$  and velocity between  $v$  and  $v + dv$  together. The total number of that group is denoted as  $f(x, v, t)dx dv$ , where  $f$  is the distribution function. Given the acceleration of the particles  $\mathbf{a}$ , we can describe the evolution of  $f$  using the Vlasov equation,

$$\frac{\partial f}{\partial t} + \mathbf{v} \cdot \frac{\partial f}{\partial \mathbf{x}} + \mathbf{a} \cdot \frac{\partial f}{\partial \mathbf{v}} = 0. \quad (1.4)$$

The left-hand-side of the Vlasov equation can be expressed as  $\frac{d}{dt}f(x(t), v(t), t)$  for a given particle orbit. As a result,  $f$  is constant along the particle trajectory, so we can choose  $f$  to depend on any quantities that are constant along the particle trajectory. This is a useful technique for finding the solution to the Vlasov equation.

### **Two-Fluids**

We can define a collision operator  $C_{\sigma\alpha}(f_\sigma)$  as a rate of change of  $f_\sigma$  due to collisions of species  $\sigma$  with species  $\alpha$ . Then by taking moments ( $\int dv, \int v dv$ ) of the distribution function  $f$ , we can derive the fluid equation for species  $\sigma$ ,

$$n_\sigma m_\sigma \frac{d\mathbf{u}_\sigma}{dt} = n_\sigma q_\sigma (\mathbf{E} + \mathbf{u}_\sigma \times \mathbf{B} - \nabla P_\sigma - \mathbf{R}_{\sigma\alpha}), \quad (1.5)$$

where  $n_\sigma = \int f_\sigma dv$ ,  $m_\sigma, q_\sigma$  is the mass and charge of species  $\sigma$ ,  $d/dt = \partial/\partial t + \mathbf{u}_\sigma \cdot \nabla$  is the convective derivative,  $\mathbf{u}_\sigma = \int \mathbf{v} f_\sigma d\mathbf{v} / n_\sigma$ ,  $\mathbf{E}$  and  $\mathbf{B}$  are the electromagnetic fields,  $P_\sigma = \frac{m_\sigma}{3} \int \mathbf{v}' \cdot \mathbf{v}' f_\sigma d\mathbf{v}'$ ,  $\mathbf{v}'$  is the random velocity, and  $\mathbf{R}_{\sigma\alpha} = \nu_{\sigma\alpha} m_\sigma n_\sigma (\mathbf{u}_\sigma - \mathbf{u}_\alpha)$  is the drag force due to collision between species  $\sigma$  and species  $\alpha$ . Traditionally,  $\sigma$  represents electrons and ions; hence, the model is called two-fluids. Occasionally, a third species is included.

### **Magnetohydrodynamics**

One could further combine the two species as a single conducting fluid. By taking moments from the Vlasov equation, multiplying it by  $m_\sigma$ , and summing over the

species, we could derive the continuity equation (Eq. 1.6) and equation of motion (Eq. 1.7) for MHD. The list of MHD equations is

$$\frac{\partial \rho}{\partial t} + \nabla \cdot (\rho \mathbf{U}) = 0, \quad (1.6)$$

$$\rho \left( \frac{\partial}{\partial t} + \mathbf{U} \cdot \nabla \right) \mathbf{U} = \mathbf{J} \times \mathbf{B} - \nabla P, \quad (1.7)$$

$$P \rho^{-5/3} = \text{constant}, \quad (1.8)$$

$$\nabla \times \mathbf{E} = -\frac{\partial \mathbf{B}}{\partial t}, \quad (1.9)$$

$$\nabla \times \mathbf{B} = \mu_0 \mathbf{J}, \quad (1.10)$$

$$\mathbf{E} + \mathbf{U} \times \mathbf{B} = \eta \mathbf{J}, \quad (1.11)$$

where  $\rho = \sum_{\sigma} m_{\sigma} n_{\sigma}$ ,  $\mathbf{U} = \sum_{\sigma} m_{\sigma} n_{\sigma} \mathbf{u}_{\sigma} / \rho$ ,  $\mathbf{J} = \sum_{\sigma} n_{\sigma} q_{\sigma} \mathbf{u}_{\sigma}$ . Equation 1.8 is the equation of state of the fluid in the single adiabatic regime. Faraday's (Eq. 1.9) and Ampere's (Eq. 1.10) law are taken from Maxwell's equations. Ultimately, Ohm's law (Eq. 1.11) can be derived from the two-fluid electron equation of motion. The MHD equations, roughly speaking, are valid when (i) the plasma is quasi-neutral within a sphere of radius Debye length, (ii) the plasma is collisional, (iii) the characteristic velocity is much slower than the speed of light, (iv) the characteristic time is long comparing to the ion cyclotron period, and (v) and the scale length is large comparing to the ion skin depth. Although a number of approximations have to be made to arrive at this most simplified description of the plasma, it is powerful enough to explain numerous natural occurrences. Most of the analysis in this thesis will be in the MHD regime.

### Frozen-in Flux

For *ideal* MHD, the plasma is treated as a perfect conductor, i.e.  $\eta = 0$ . We can combine Eq. 1.9-1.11 to get an induction equation,

$$\frac{\partial \mathbf{B}}{\partial t} = \nabla \times (\mathbf{U} \times \mathbf{B}). \quad (1.12)$$

Consider the rate of change of magnetic flux  $\Phi = \int_{S(t)} \mathbf{B}(\mathbf{x}, t) \cdot d\mathbf{s}$  through a surface  $S(t)$ , bounded by a contour  $C(t)$ . Then,

$$\frac{D\Phi}{Dt} = \lim_{\delta t \rightarrow 0} \frac{\int_{S(t+\delta t)} (\mathbf{B} + \delta t \frac{\partial \mathbf{B}}{\partial t} \cdot d\mathbf{s}) - \int_{S(t)} \mathbf{B} \cdot d\mathbf{s}}{\delta t} \quad (1.13)$$

$$= \lim_{\delta t \rightarrow 0} \frac{\int_{S(t)} (\mathbf{B} + \delta t \frac{\partial \mathbf{B}}{\partial t} \cdot d\mathbf{s}) + \oint_C \mathbf{B} \cdot \mathbf{U} \delta t \times d\mathbf{l} - \int_{S(t)} \mathbf{B} \cdot d\mathbf{s}}{\delta t} \quad (1.14)$$

$$= \int_{S(t)} \frac{\partial \mathbf{B}}{\partial t} \cdot d\mathbf{s} + \oint_C \mathbf{B} \cdot \mathbf{U} \times d\mathbf{l} \quad (1.15)$$

$$= \int_{S(t)} \left[ \frac{\partial \mathbf{B}}{\partial t} + \nabla \times (\mathbf{B} \times \mathbf{U}) \right] \quad (1.16)$$

$$= 0. \quad (1.17)$$

This is called the magnetic flux frozen-in condition and is the essential property for an ideal MHD plasma. Magnetic field lines move together with the plasma without diffusion. A motion of plasma can then be visualized by a moving tube-like region containing magnetic field. Magnetic flux is conserved in a cross section of this region, so-called *flux tube*. A twisted magnetic flux tube is referred to as a *flux rope*.

### Dimensionless MHD

Suppose we make the substitution  $\mathbf{x} = L\bar{\mathbf{x}}$ ,  $\mathbf{U} = v_A \bar{\mathbf{U}}$ ,  $t = (L/v_A)\bar{t}$ ,  $\rho = \rho_0 \bar{\rho}$ ,  $\mathbf{B} = B_0 \bar{\mathbf{B}}$ ,  $\mathbf{J} = (B_0/\mu_0 L)\bar{\mathbf{J}}$ ,  $P = P_0 \bar{P}$ , and  $v_A = B_0/\sqrt{\mu_0 \rho_0}$  to the MHD system of equations (Eq. 1.6-1.11). The normalized MHD equations are

$$\frac{\partial \bar{\rho}}{\partial \bar{t}} + \bar{\nabla} \cdot (\bar{\rho} \bar{\mathbf{U}}) = 0, \quad (1.18)$$

$$\bar{\rho} \left( \frac{\partial}{\partial \bar{t}} + \bar{\mathbf{U}} \cdot \bar{\nabla} \right) \bar{\mathbf{U}} = \bar{\mathbf{J}} \times \bar{\mathbf{B}} - \beta \bar{\nabla} \bar{P}, \quad (1.19)$$

$$-\frac{\partial \bar{\mathbf{B}}}{\partial \bar{t}} + \bar{\nabla} \times (\bar{\mathbf{U}} \times \bar{\mathbf{B}}) = \frac{1}{S} \bar{\nabla}^2 \bar{\mathbf{B}}, \quad (1.20)$$

where  $\beta \equiv 2\mu_0 P_0/B_0^2$  represents the ratio of thermal to magnetic pressure and  $S \equiv \mu_0 L v_A/\eta$ , also known as Lundquist number, represents the relative timescale of magnetic convection to diffusion. Table 1.1 shows the values of the two dimensionless parameters in both solar and Caltech environments. The plasmas in both systems have  $\beta \ll 1$  and  $S \gg 1$  and hence can be approximately modelled using the same normalized MHD equations.

Parameter	Corona	Laboratory
Density ( $\text{m}^{-3}$ )	$10^{15}$	$10^{20-21}$
Temperature (K)	$10^6$	$3 \times 10^4$
Magnetic Field (T)	$10^{-3}$	$3 \times 10^{-2}$
Resistivity ( $\Omega\text{-m}$ )	$8 \times 10^{-7}$	$3 \times 10^{-3}$
Characteristic Length (m)	$10^{6-8}$	$5 \times 10^{-2}$
Characteristic Time (s)	$10^{2-3}$	$10^{-6}$
$\beta \ll 1$	$10^{-3} - 10^{-2}$	$10^{-2} - 10^{-1}$
$S \gg 1$	$10^8 - 10^{12}$	$10^2 - 10^3$

Table 1.1: Lists of parameters in laboratory and corona

### MHD Instabilities

The solutions to the MHD equations when  $\partial/\partial t = 0$  correspond to MHD equilibrium. There are two types of the equilibrium: stable and unstable. The difference lies in the response to a small perturbation. An example of a stable equilibrium is a ball sitting at the bottom of a valley. The perturbed ball experiences a restoring force that pushes it back to equilibrium. On the contrary, a ball on top of a hill experiences the force that pushes the ball further away from equilibrium. The latter case corresponds to instability, where the amplitude grows exponentially from a certain perturbation. In ideal MHD, the plasma is susceptible to two distinct types of instabilities based on two types of forces. Current-driven instability corresponds to the  $\mathbf{J} \times \mathbf{B}$  force and pressure-driven instability corresponds to the  $\nabla P$  force. Figure 1.1a shows a common pressure-driven instability, the Rayleigh-Taylor instability. It refers to an instability that occurs when a heavier fluid sits on top of a light fluid in a gravitational field. Figure 1.1b displays two simplest modes of the current-driven instability: sausage and kink. The sausage mode corresponds to a situation where a cylindrical plasma column with surface current experiences small changes in its minor radius. The kink mode happens when the axis of a cylindrical plasma column becomes helical. Studying the condition when the plasma is prone to these instabilities is a subject of interest for many research fields. Thermonuclear fusion researchers wish to confine a hot-dense plasma by attempting to suppress any instability that might occur. Solar physics community researchers examine these instabilities as a mechanism for driving energetic particles.

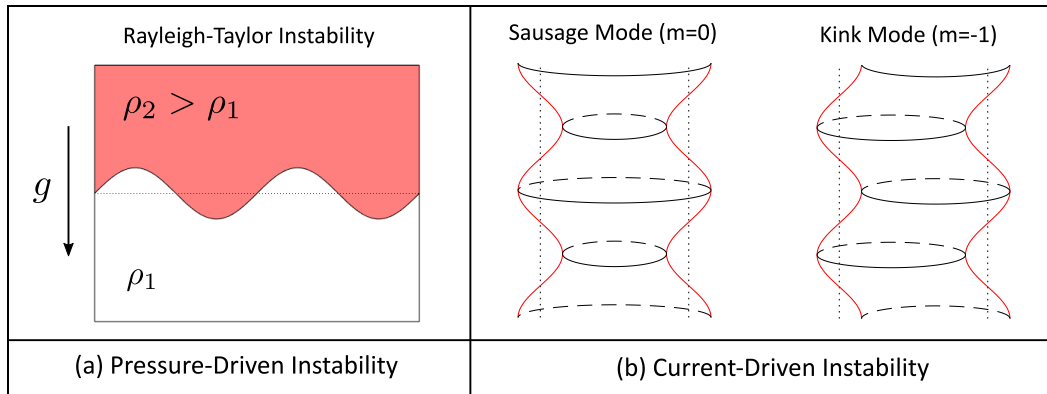


Figure 1.1: Illustration for different type of MHD instability

## 1.2 Solar Physics

The sun is our closest star and has been studied for thousands of years. It is a sphere of hot plasma that produces strong magnetic fields on the surface through internal convective motion. It is composed of mostly hydrogen and gains energy from the nuclear fusion reaction in its core. It is the main source of energy for all life on earth. Although the sun is essential to sustain life, its extensive magnetic activities on the surface could pose dangers to us. We will describe some of these hazardous events in the following sections.

### Coronal Mass Ejections

The sun often ejects a significant mass of plasma ( $\sim 10^{12}$  kg) and associated magnetic fields into the corona, also known as, coronal mass ejections (CMEs). Typical CMEs originated from an eruption of large plasma structures, such as long-standing stationary prominences ( $\sim$  weeks). These features stay in a static equilibrium for many Alfvén crossing times and then abruptly erupt (Figure 1.2). The event is frequent, occurring 0.2-3.0 times per day, and thus it is likely that one would directly hit the earth in a reasonable amount of time.

The mechanism for the eruption is still a subject of a debate. Once erupted, the CMEs show a three-part structure that is associated with (i) the prominence core, (ii) the density cavity, and (iii) the leading edge. On the CME front, MHD shocks are often observed. CMEs affect space weather significantly. A direct hit of Earth by a CME could cause serious damage to spacecraft or electrical grids. We will be studying several components that might affect this event. Figure 1.3 represents the related topics that are explored in more detail in each chapter.

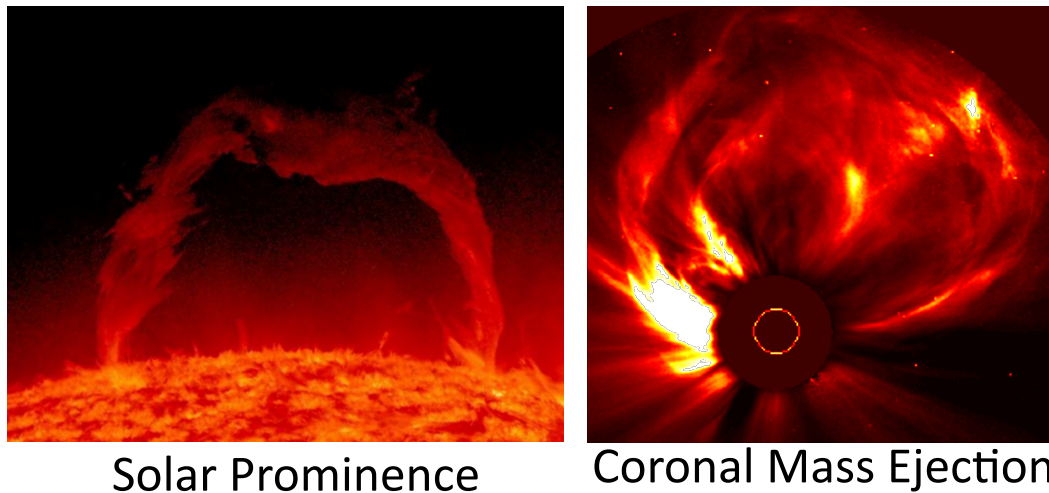


Figure 1.2: Image of a solar prominence and a CME

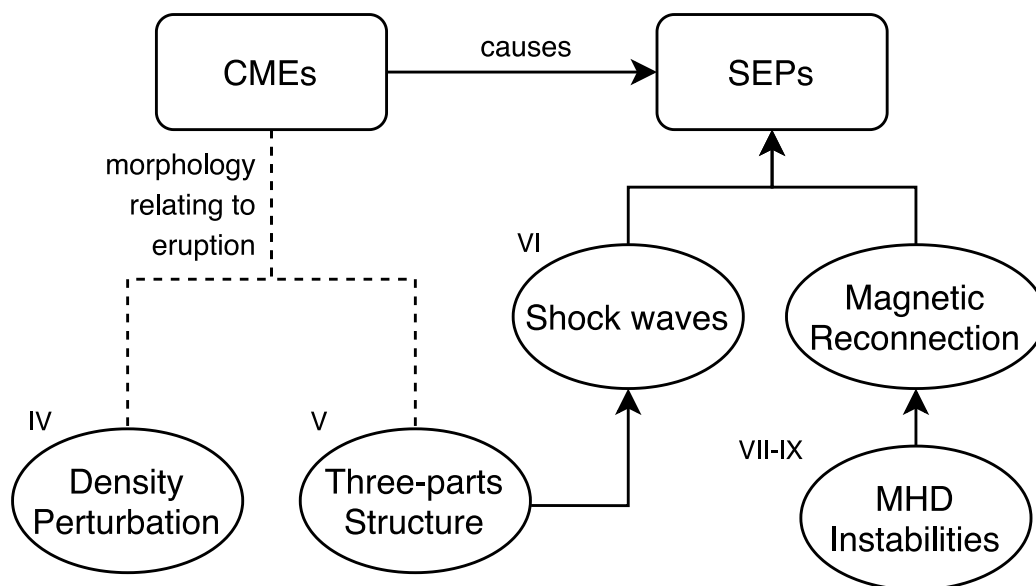


Figure 1.3: Outline of the topics in the thesis. The associated chapters are labelled in roman numerals.

### Solar Energetic Particles

Solar energetic particles (SEPs) are energetic charged particles which consist of mostly proton, electron, and sometimes heavier ions. They are often observed in association with CMEs. The particles are accelerated up to energies between keV to GeV and are believed to be driven to high energy through CME-driven shock acceleration or plasma instabilities. Once these energetic particles reach the earth, the radiation is hazardous to aircraft passengers and spacecraft.

## *Chapter 2*

### LABORATORY PLASMA

As discussed in the previous chapter, the MHD plasma has no intrinsic scale; therefore, the events caused by plasma dynamics on the sun can be reproduced in the laboratory. At Caltech, we simulate those phenomena by operating a pulse-power experiment. The experimental system consists of a vacuum chamber, gas supply systems, solenoids, and electrodes. Each of these systems replicates a fundamental property of solar flux ropes: a vacuum chamber and a controlled gas supply are needed to create plasma of appropriate density, the solenoids recreate the background magnetic fields, and the electrodes drive current through the flux rope, adding the appropriate twist to the magnetic field.

#### 2.1 Single Loop Experiment

The primary experiment for the work in this dissertation is the arched plasma-filled magnetically-twisted flux rope. The experiment is called the *Single Loop Experiment* in contrast to other experiments operated by our group, i.e., double-loop [51] and 8-loop (jet; section 2.2) [13] experiments. It has gone through many iterations in the past [46, 49, 125]. The current version consists of two D-shaped copper electrodes of radius 10 cm, mounted at the end of a 1.5 m long, 0.92 m diameter vacuum chamber with  $10^{-7}$  Torr base pressure. Behind the electrode, two solenoids generate an arched background magnetic field  $\sim 0.1$  T. Two fast gas valves inject cones of neutral particles through the holes in the electrode over 5 ms [165]. A high voltage of 3-5 kV is applied to the electrodes from a 59  $\mu$ F capacitor driving 30 kA current through the arched plasma of density  $10^{21}$  m $^{-3}$ . A sketch of the experimental setup is shown in Figure 2.1. This experimental setup is used for Chapters 4-7.

Two main settings are used in this thesis and they differ by the presence of initially prefilled neutral gas. In the first setting, the chamber is not prefilled with neutral gas; the only gas supply is from the nozzles on the electrodes. This is a traditional setup for single loop experiment and it produces an arched flux rope that evolves into the chamber as shown in Figure 2.2. Chapters 4 and 7 use this first setting.

In the second setting, the chamber is prefilled with a neutral gas of pressure 0.1 Torr. The prefilled gas and the gas injected from the nozzles could be of different types,

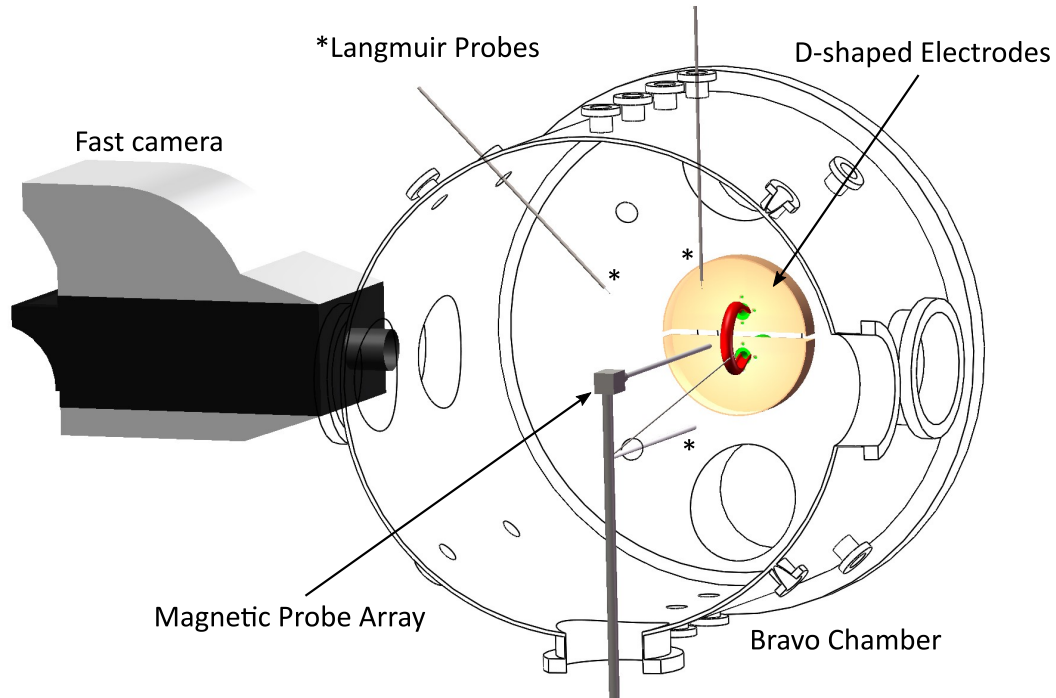


Figure 2.1: Diagram for Caltech Single Loop Experiment

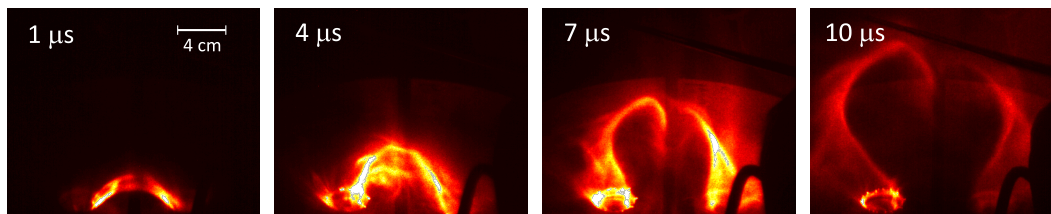


Figure 2.2: Evolution of single loop  $N_2$  plasma without the initially prefilled neutral (#5594). Times after plasma breakdown are labelled in white.

allowing for spectroscopic techniques to identify each component of the plasma. Figure 2.3 shows a typical evolution of the flux rope with injected Ar and prefilled  $H_2$ .

The experiments in Chapters 5 and 6 were performed using this second setting.

## 2.2 Astrophysical Jet Experiment

The jet experiment consists of all the same systems as the single loop with one caveat: instead of one, eight loops are generated. The electrodes are now coaxial and the electric fields are now generated in the radial direction. Each electrode contains 8 holes that let in the neutral gas stream from the fast gas valve. Compared to the single loop experiment, there are minor differences in the experimental parameters. The

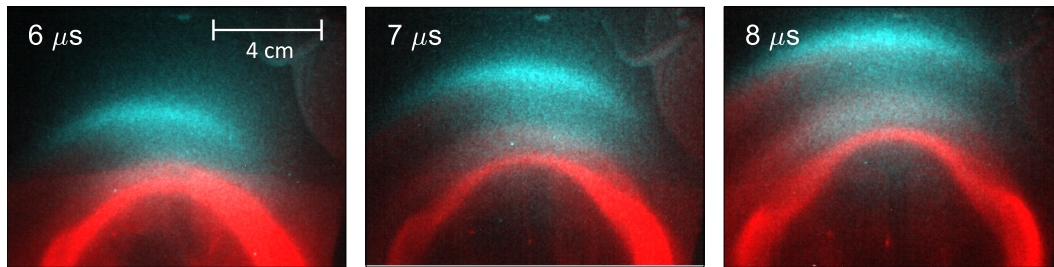


Figure 2.3: Evolution of single loop argon plasma with the initially prefilled hydrogen neutral gas. The image series are superimposed from 2 shots with the same experimental settings: with (#3221; red) and without (#3222; cyan) 656 nm filter ( $H\alpha$ ). Times after breakdown are labelled in white.

electrodes are 0.2 m and 0.5 m in diameter, mounted on one end of a 1.4 m diameter and 1.6 m long cylindrical vacuum chamber. The mass density and magnetic field strength is roughly 8 times larger than that of the single loop experiment. The capacitor bank, charged up to a similar voltage as the single loop experiment, drives 90 kA current through the plasma. This experimental setup simulates not only astrophysical jets, but also solar prominences. This experimental configuration [59, 98, 120, 161] creates an MHD-driven plasma jet which spontaneously develops as a result of magnetic helicity, plasma, and magnetic energy being injected by biased electrodes intercepting poloidal magnetic flux.

The magnetic fields of the axisymmetric jet are topologically similar to that of a footpoint of an arched plasma loop.

Chapters 8 and 9 describe simulations of this experiment.

### 2.3 Diagnostics

The main advantage of laboratory study is the reproducibility and the ability to perform in situ measurement. The following sections display several devices for inferring plasma parameters.

#### Fast Camera Imaging

The visible light emission of the plasma is captured via a DRS Hadland Imacon 200 high speed camera. The camera consists of seven intensified charge-coupled (ICCD) cameras that each take two frames from each shot. A beam splitter is used to direct the incoming light into one of the seven ICCD's. In the usual setting of our experiment, the plasma can be photographed using an exposure time of 20 ns. The interframe time of the camera can be as low as 5 ns. Each ICCD produces a 10 bit

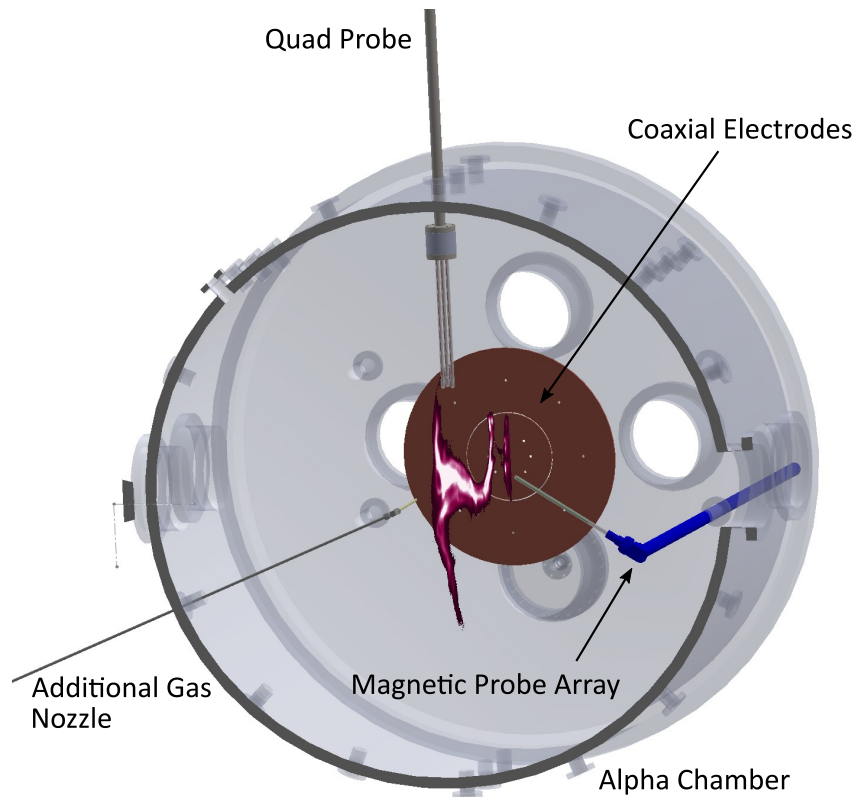


Figure 2.4: Diagram for Caltech Jet Experiment

image with resolution  $1200 \times 980$ .

### Magnetic Probes

Magnetic fields are measured using an array of coils. Changing magnetic field induces electromotive forces across the two ends of a coil according to Faraday's law. Three coils form a cluster and are oriented perpendicularly to each other to measure a vector  $\mathbf{B}(\mathbf{r})$  at a location  $\mathbf{r}$ . Several of these clusters can be put together to form an array. We mount the array on a movable stalk and can scan the probe through the spatial domain  $\mathbf{r}$  to get the time series  $\mathbf{B}$  at different locations. The magnetic field through the coil  $B(t)$ , given the measured voltage across the coil  $V(t)$ , is then

$$B(t) = B_0 - \frac{1}{NA} \int_0^t V(t') dt', \quad (2.1)$$

where  $B_0$  is the initial magnetic field,  $N$  is the number of turns, and  $A$  is the area of the coil.

### Langmuir Probes

The density and temperature of a plasma can be determined locally by a Langmuir probe. One could make such measurement by putting a metal wire into the plasma and biasing it with a certain potential  $\phi$ . If such potential is different from the plasma potential, there would be an imbalance in the ion and electron flux, resulting in the probe picking up a net current. The pickup current  $I$  depends on the probe potential, the plasma density  $n_0$  and electron temperature  $T_e$ .

$$I = n_0 c_s e A - n_0 e A \sqrt{\frac{\kappa T_e}{2\pi m_e}} \exp\{-e|\bar{\phi}(x)|/\kappa T_e\}, \quad (2.2)$$

where  $c_s = \sqrt{\kappa T_e/m_i}$  is the ion acoustic velocity,  $e$  is the elementary charge,  $A$  is the probe area, and  $\bar{\phi} = \phi - \phi_{\text{plasma}}$  is the relative potential.

### Spectroscopy

Since the plasma that we study is generally hot, we observe line emissions from the elements that constitute the plasma. We can collect the light emission from plasma, put it through a spectrometer. The light with different wavelength is diffracted to a different angle and then captured by an ICCD camera. We obtain knowledge of the plasma local state by comparing the spectrum of the emitted light with a thermodynamic model. Doppler shift and Stark broadening can infer the plasma flow velocity and density respectively.

## Chapter 3

### 3D MAGNETOHYDRODYNAMICS SIMULATION

While diagnostics provide us with a real time-series measurement, plasma parameters often are obtained locally. Although total current and voltage across the plasma are the two obtainable global parameters, the associated electric field  $\mathbf{E}$  and current density  $\mathbf{J}$  are unknown in the 3-dimensional space. 3D numerical simulation can help us understand how these parameters evolve in the 3D spatial domain. Numerical simulation alone usually leads to working with the wrong physical assumptions. Therefore, together with the experiment, the simulation betters our understanding to provide a more complete picture.

The 3D MHD numerical simulation was performed on the Los Alamos Turquoise supercomputer cluster using part of the Los Alamos COMPUtational Astrophysical Simulation Suite [80] which is a collection of several modern, high resolution, Godunov-type, MHD codes. The code tracks the evolution of 8 dimensionless parameters namely: density  $\rho$ , velocity  $\mathbf{v}$ , magnetic field  $\mathbf{B}$ , and pressure  $P$  inside a Cartesian box of size  $[-L, L]^3$ .

#### 3.1 Normalization

The dimensionless resistive MHD equations in conservative form are

$$\frac{\partial \bar{\rho}}{\partial \bar{t}} + \bar{\nabla} \cdot (\bar{\rho} \bar{\mathbf{v}}) = 0 \quad (3.1)$$

$$\frac{\partial (\bar{\rho} \bar{\mathbf{v}})}{\partial \bar{t}} + \bar{\nabla} \cdot \left( \bar{\rho} \bar{\mathbf{v}} \bar{\mathbf{v}} + \left( \bar{P} + \frac{\bar{B}^2}{2} \right) \overleftrightarrow{\mathbf{I}} - \bar{\mathbf{B}} \bar{\mathbf{B}} \right) = 0 \quad (3.2)$$

$$\frac{\partial \bar{e}}{\partial \bar{t}} + \bar{\nabla} \cdot \left[ \left( \bar{e} + \bar{P} + \frac{\bar{B}^2}{2} \right) \bar{\mathbf{v}} - \bar{\mathbf{B}} (\bar{\mathbf{v}} \cdot \bar{\mathbf{B}}) \right] = \dot{\bar{e}}_{\text{inj}} \quad (3.3)$$

$$\frac{\partial \bar{\mathbf{B}}}{\partial \bar{t}} - \bar{\nabla} \times (\bar{\mathbf{v}} \times \bar{\mathbf{B}}) - \frac{1}{S} \bar{\nabla}^2 \bar{\mathbf{B}} = \bar{\mathbf{B}}_{\text{inj}}, \quad (3.4)$$

where the total energy density is  $\bar{e} \equiv \bar{\rho} \bar{v}^2 / 2 + \bar{P} / (\gamma - 1) + \bar{B}^2 / 2$  with  $\gamma = 5/3$ .

The normalization constants are chosen to scale the simulation to the desired plasma system. For the reference parameters  $\rho_0$ ,  $L$ , and  $v_A$ , we pick the other reference parameters as  $B_0 = v_A \sqrt{\mu_0 \rho_0}$ ,  $p_0 = \rho_0 v_A^2$ ,  $\tau_A = L / v_A$ ,  $e_0 = p_0 L^3$ , and  $S = \mu_0 v_A L / \eta$ .  $\dot{\bar{e}}_{\text{inj}}$  represents the dimensionless energy injection, i.e.,

$$\dot{e}_{\text{inj}} = \dot{B}_{\text{inj}} \cdot \bar{\mathbf{B}}. \quad (3.5)$$

The following two sections describe the initial conditions and injection profiles for two configurations. Section 3.2 provides the information for the arched flux rope for the simulation of the single loop experiment; this configuration is used in Chapters 4-6. Section 3.3 describes an axisymmetric system. The simulation is used to replicate the astrophysical jet experiment or the footpoint of the single loop experiment. This configuration is used in Chapter 8-9.

### 3.2 Arched Configuration

In an arched flux rope configuration, the nozzles on the electrodes create a constraint for the distribution of plasma. The initial neutral gas density is largest at the nozzle and falls off further away. The current density right after the breakdown is also mostly concentrated since the breakdown condition depends on the plasma density. Moreover, the axial magnetic flux is strongest at the nozzle because of the location of the solenoid and the attenuation from the copper electrodes.

#### Initial Conditions

Previous neutral gas measurements by a fast ion gauge [97, 165] give an empirical density profile as an exponential cone with an expression

$$\rho(x, y, z) = \rho_0 \left( \frac{z_0}{|z| + z_0} \right)^2 \exp \left[ -\frac{K(x^2 + y^2)}{(|z| + z_0)^2} \right], \quad (3.6)$$

where  $K = \tan \alpha \sqrt{\log 2} = 1.1$ ,  $\alpha \approx 54^\circ$  is the half cone angle,  $z_0 = 0.01$  m, and  $\rho_0 = 2 \times 10^{-3}$  kg m<sup>-3</sup> is the density at the footpoints.

The initial background magnetic field (bias field) is generated by specifying a set of loop currents in a half-circle configuration below the electrode plane. This ensures that all field lines emerge and terminate at the footpoints. This topology is closer to that of the experimental field (i.e., where  $B_z$  does not change sign on a given electrode) than a simple dipole and is scaled to match the measured field strength at the loop apex. The resulting initial bias field is shown in Figure 3.1.

#### Injection Routine

Diffuse poloidal flux is continuously injected into the simulation domain corresponding to the electric current measured in the experiment. The diffuse current profile

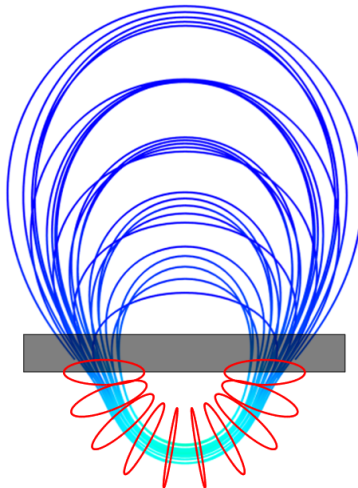


Figure 3.1: Plot of the initial conditions for the simulation. Source currents for the background magnetic field consist of 10 thin loops arranged in a semi-circle (red), B-field lines are shown in blue. The high density plasma wall boundary is shown in black.

is constructed from the superposition of 110 thin circular current loops, where each loop has a simple analytic magnetic field expression [124]. A corresponding vector potential in spherical coordinates  $(r, \theta, \phi)$  is

$$A_\phi(r, \theta) = \frac{\mu_0}{4\pi} \frac{4Ia}{\sqrt{a^2 + r^2 + 2ar \sin \theta}} \left[ \frac{(2 - k^2)K(k^2) - 2E(k^2)}{k^2} \right], \quad (3.7)$$

$$k^2 = \frac{4ar \sin \theta}{a^2 + r^2 + 2ar \sin \theta}, \quad (3.8)$$

where  $I$  is the loop current,  $a$  is the loop radius,  $K$  and  $E$  are the complete elliptic integral of the first and second kind respectively.

To avoid singularities, the elliptic integrals are approximately evaluated using truncated power series. This injected distribution, shown in Figure 3.2a, is physically motivated by experimental current density measurements which indicate that the current profile begins as a flared diffuse structure and maintains this outer diffuse current during helicity injection. Figure 3.2c shows the current path of 10 loops in  $yz$ -plane with apexes equally spaced from  $1.2y_0$  to  $2.6y_0$ , where  $\pm y_0$  are locations of the footpoints and  $y_0 = 4$  cm. Figure 3.2b shows another view of the profile in  $xz$ -plane with 11 sets of 10 current loops distributed over  $\theta_{yz} \in [-54^\circ, 54^\circ]$  with respect to the  $yz$ -plane. The injected current profile is stationary throughout the simulation. Since we are principally interested in the formation phase, we do

not attempt to model the helicity extraction or the decreasing current after  $t_{\text{off}}=20 \mu\text{s}$ . The experimentally measured current undergoes a damped oscillation with the period  $T = 40 \mu\text{s}$ , so we model the temporal dependence of the injection as

$$\frac{d}{dt}B(t) = \dot{B}_0 \cos\left(\frac{2\pi t}{T}\right) H(t_{\text{off}} - t), \quad (3.9)$$

where  $\dot{B}_0$  has only spatial dependency and  $H$  is a Heaviside step function.

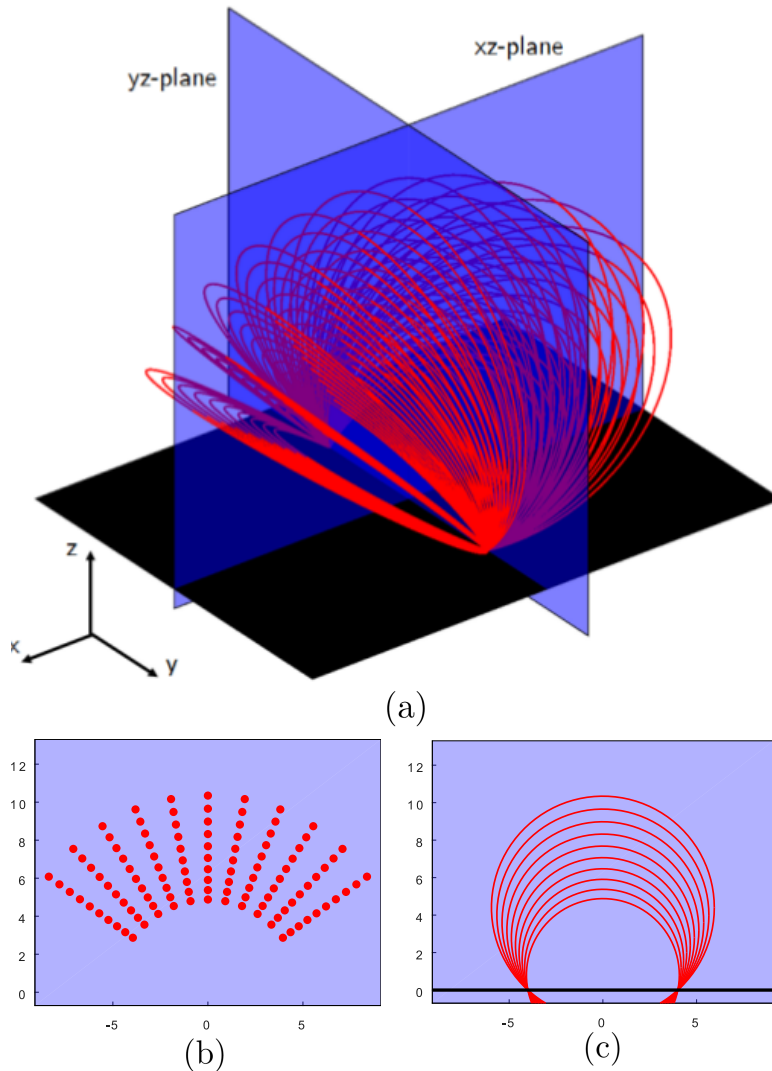


Figure 3.2: Illustration of spatial profile of the current injection. Each red circle represents a thin circular current loop. (a) The 3 dimensional view showing all 110 loops. (b) The 2 dimensional cross section in  $xz$ -plane. (c) The 2 dimensional cross section in  $yz$ -plane. The spatial units are in centimeters.

### 3.3 Axisymmetric Configuration

In this configuration, the spatial domain is still the same as in the previous configuration, i.e., box of size  $[-L, L]^3$ . However expressions for initial parameters are now in cylindrical geometry;  $(x, y, z) \rightarrow (r, \theta, z)$ .

#### Initial Condition

The initial condition is that of an axisymmetric flux rope with uniform axial current density  $J_z = I/(\pi a^2)$  for  $r < a$  and  $J_z = 0$  for  $r > a$ . In one configuration (extreme paramagnetism) a uniform axial magnetic field  $B_z$  exists only inside the current channel ( $r < a$ ) while in another configuration  $B_z$  exists over the entire domain. The code evolves the vector potential  $\mathbf{A} = (A_x, A_y, A_z)$  to maintain the divergenceless condition of the magnetic field,  $\nabla \cdot \mathbf{B} = 0$ . The density is set to have a Gaussian profile that decays radially from the flux rope axis which is located at position  $\mathbf{r}_0$ . A small uniform background density  $\rho_b$  was added to avoid requiring an infinitely small time step. The plasma is initially at rest with a uniform temperature,  $T = P/\rho = 1$ . The initial density, pressure, velocity, and vector potential are specified as

$$\rho = \rho_0 \exp\left(-(\mathbf{r} - \mathbf{r}_0)^2/2\sigma^2\right) + \rho_b \quad (3.10)$$

$$P = \rho, \quad \mathbf{v} = 0, \quad A_x = 0, \quad A_y = B_z x \quad (3.11)$$

$$A_z = \begin{cases} -(I/4\pi)(r/a)^2 & , r < a \\ -(I/4\pi)(1 + 2 \ln(r/a)) & , r > a. \end{cases} \quad (3.12)$$

*Chapter 4*

## APEX DIPS OF EXPERIMENTAL FLUX ROPES

Pakorn Wongwaitayakornkul, Magnus A Haw, Hui Li, Shengtai Li, and Paul M Bellan. “Apex Dips of Experimental Flux Ropes: Helix or Cusp?” In: *The Astrophysical Journal* 848.2 (2017), p. 89. DOI: <https://doi.org/10.3847/1538-4357/aa8990>.

P.W. designed and conducted the experiment. P.W. and M.A.H developed the simulation. H.L. and S.L. provided the simulation source code. P.W., M.A.H., and P.M.B discussed and wrote the manuscript.

We present a new theory for the presence of apex dips in certain experimental flux ropes. Previously such dips were thought to be projections of a helical loop axis generated by the kink instability. However, new evidence from experiments and simulations suggest that the feature is a 2D cusp rather than a 3D helix. The proposed mechanism for cusp formation is a density pileup region generated by nonlinear interaction of neutral gas cones emitted from fast-gas nozzles. The results indicate that density perturbations can result in large distortions of an erupting flux rope, even in the absence of significant pressure or gravity forces. The density pileup at the apex also suppresses the  $m=1$  kink mode by acting as a stationary node. Consequently, more accurate density profiles should be considered when attempting to model the stability and shape of solar and astrophysical flux ropes.

**4.1 Introduction**

Several experiments in the past decades [46, 48, 49, 101, 125, 133, 141] have sought to improve understanding of solar flux ropes by recreating scale models in the laboratory. Experiments are relevant because the MHD equations have no intrinsic length scale and can be expressed in a non-dimensional fashion. Many mechanisms for flux rope stability [46, 49, 101], formation [7, 125, 141], particle acceleration [140], and reconnection [48] have been discovered and tested in these experiments.

However, a particular feature common to several of these experiments [46, 49, 125, 133] has not been well understood: this feature is a downward dip present at the loop apex as shown in Fig. 4.1a. The interpretation until now has been that the dip seen in images is the projection of a helical loop axis generated by the kink instability

[3, 49, 125]. However, there are several problems with this interpretation. First, the observed dip is always downwards, whereas the kink instability should generate both upward and downward helical perturbations. Second, images from other angles show no evidence for helical structure in the third dimension (Fig. 4.1b). Third, kink modes should grow but the dip remains a constant size. Lastly, the dip feature only appears in certain experiments [3, 46, 49, 125] but not others with similar physics [101, 141]. Alternative to the helical interpretation is that the dip is a sharp downward cusp, but this interpretation has no obvious formation mechanism and has consequently not been considered until now.

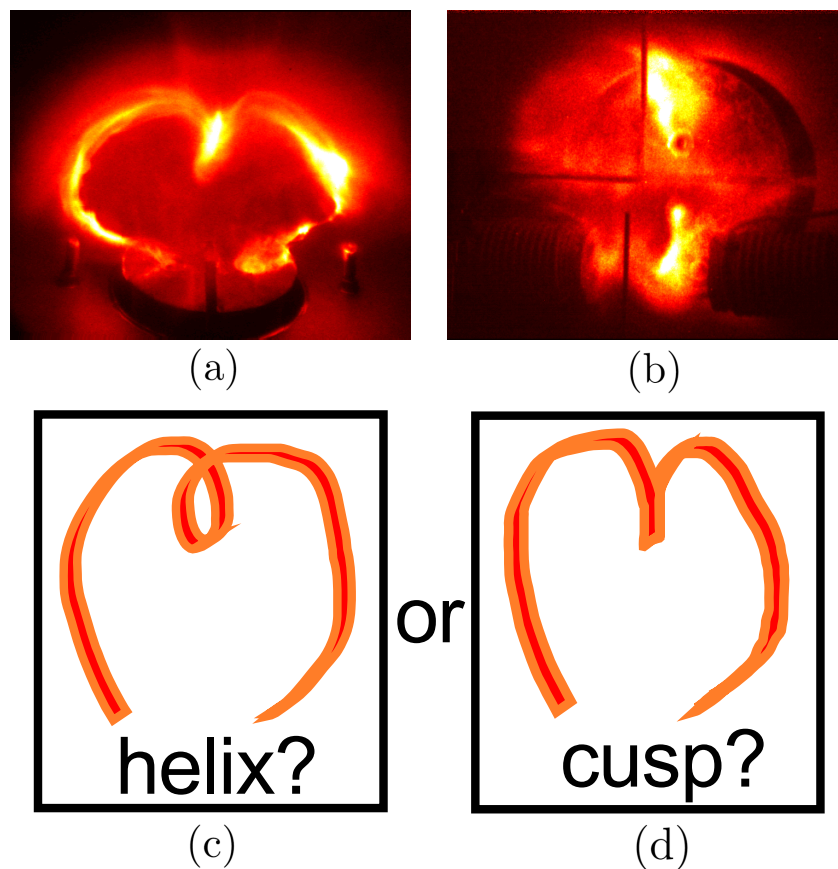


Figure 4.1: (a) Side view of lab experiment flux rope showing dip at apex, (b) top view of lab flux rope showing no evidence of helical shape, (c) sketch of side view for helix interpretation, (d) sketch of side view for downward cusp interpretation

This chapter identifies a formation mechanism for the cusp shape sketched in Figure 4.1d and provides detailed evidence from theory, experiment, and simulation supporting the cusp interpretation. The proposed mechanism is that neutral gas, injected from fast-gas valves at both footpoints, collides at the loop midplane cre-

ating a density pileup region. This causes the loop apex to have a greater linear mass density than the rest of the loop and, since the apex and the rest of the loop experience equivalent forces, the apex will have a slower acceleration, leading to the formation of a downward cusp during expansion. This theory explains why the dip is always downward, why there is no helical structure or dip growth, and why the feature only appears in experiments with gas injection from both footpoints. The results indicate that density perturbations can greatly distort the shape of an erupting flux rope and that introducing such perturbations may suppress external kink modes. These results are applicable to all MHD flux ropes with density perturbations (solar prominences, tokamaks, astrophysical jets etc.) and are especially relevant to the morphology of solar eruptions. Furthermore, other plasma experiments which use fast-gas valves [46, 49, 84, 96, 107, 111, 125, 127, 133] should be aware of the potential for non-linear interaction between multiple gas valves.

## 4.2 Experimental Apparatus

Experiments simulating solar flux ropes all share certain systems: a vacuum chamber, gas supply systems, solenoids, and electrodes. Each of these systems replicates a fundamental property of solar flux ropes: a vacuum chamber and a controlled gas supply are needed to create plasma of appropriate density, the solenoids recreate the background magnetic fields, and the electrodes drive current through the flux rope, adding the appropriate twist to the magnetic field.

### Caltech Single Loop Experiments

The primary experiments of interest are the different iterations [46, 49, 125] of the Caltech single loop experiment, introduced in Section 2.1. All of these experiments exhibit the apex dip feature and have similar designs. The latest incarnation of the Caltech single loop experiment [46] has a single pair of electrodes with internal solenoids and fast-gas valves [160]. The system is mounted at the end of a 1.5 m long, 0.92 m diameter vacuum chamber with  $10^{-7}$  Torr base pressure. The solenoids, located behind the electrodes, generate an arched background magnetic field ( $< 0.1$  T). Fast valves then release cones of neutral particles over 5 ms [165] through holes in the electrodes into the vacuum chamber. High voltage applied to the electrodes by a 59  $\mu$ F capacitor ionizes the gas to form an arched plasma of density  $n \sim 10^{21}$   $\text{m}^{-3}$ . The capacitor is typically charged to 2.5-5 kV driving 30 kA of current for 10  $\mu$ s. The schematic diagram of the experimental setup is shown in Figure 4.2.

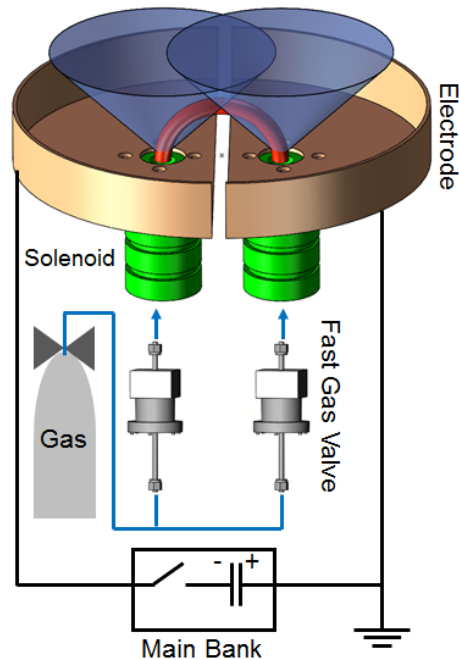


Figure 4.2: Schematic diagram of the experimental setup showing cones of neutral gas (blue) ejected from holes in electrodes (copper), plasma loop (red), solenoids (green) for providing background magnetic field, and gas injection system.

### Other Experiments

The FlareLab experiment at Ruhr University Bochum was designed based on the Caltech apparatus and has similar gas supply, timescales, electrodes, and magnetic fields [133]. This experiment also observes a downward apex dip.

The PPPL apparatus is located in the MRX facility [101]. It uses uniform background gas injection as well as fast-gas valve injection at a single footpoint. Plasma is also generated via high voltage breakdown from the electrodes. However, the timescale for this experiment is  $\sim 1$  ms, 100 times longer than the Caltech loop, and is comparable to the gas diffusion time. This experiment does not observe apex dips.

The UCLA single loop experiment [141] is generated in a uniform pre-ionized plasma and utilizes  $\text{LaB}_6$  electrodes with much lower currents (600 A). Additional density is added from laser ablation of targets at the footpoints to trigger eruptions. No apex dips are observed in this experiment.

For comparison, Figure 4.3 shows the white light images for the solar flux rope in all 4 experiments.

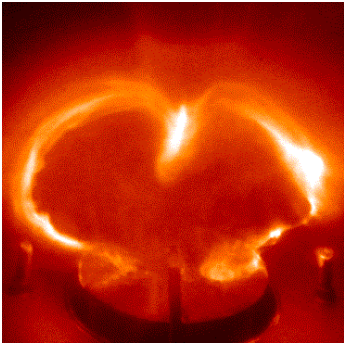
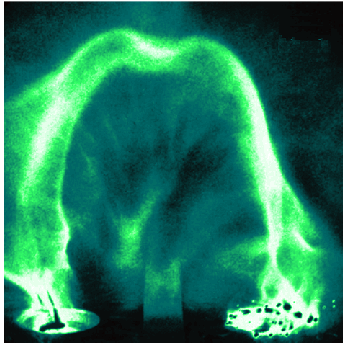
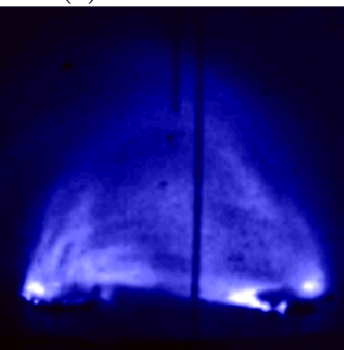
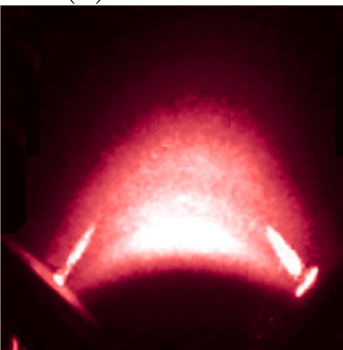
Dip Observed	<p>(a) Caltech Single-loop</p>  <p>FGV at both footpoints</p>	<p>(b) FlareLab</p>  <p>adapted with permission from Tenfelde et al. (2012)</p> <p>FGV at both footpoints</p>
Dip not Observed	<p>(c) PPPL MRX</p>  <p>provided by Clayton Myers</p> <p>neutral pre-fill and FGV at single footpoint</p>	<p>(d) UCLA SPD</p>  <p>adapted with permission from Tripathi &amp; Gekelman (2010)</p> <p>background plasma</p>

Figure 4.3: Comparison of white light images for arched flux rope experiments with their gas supply. Only experiments with fast-gas valves (FGV) at both footpoints observe dip feature

### 4.3 Theory

#### Single Gas Valve

The Caltech experiment has detailed measurements of the neutral density profile emerging from a single footpoint [97, 165]. This measured profile is that of an exponential cone:

$$\rho(x, y, z) = \rho_0 \left( \frac{z_0}{|z| + z_0} \right)^2 \exp \left[ -\frac{K(x^2 + y^2)}{(|z| + z_0)^2} \right], \quad (4.1)$$

where  $K = \tan \alpha \sqrt{\log 2} = 1.1$ ,  $\alpha \approx 54^\circ$  is the half cone angle,  $z_0 = 0.01$  m, and  $\rho_0 = 2 \times 10^{-3}$  kg m<sup>-3</sup> is the density at the footpoints.

#### Two Gas Nozzles

The two gas nozzles (1 cm apertures) are equally spaced in the  $y$  direction ( $y_0 = \pm 4$  cm) and point in the  $z$  direction. This gas injection from both nozzles creates overlapping gas cones. If the mean free path is large, the neutral gas in the two cones will not interact and the final distribution is simply a linear superposition of two cones (Figure 4.4a). However, if the neutral gas has a mean free path comparable to the system size ( $\sim 10$  cm), the gases will interact and a density pileup will form between the two cones. The mean free path is defined as:  $\ell_{\text{mfp}} = (\sigma n)^{-1}$  where  $\sigma$  is the cross-section and  $n$  is the number density. Calculations of  $\ell_{\text{mfp}}$  for the three main gases used in the experiment are shown in Table 4.1.

Under standard experimental conditions all three gases have a mean free path less than 3 mm. Since the overlap region is several centimeters wide, there should be significant interaction between the two cones.

	H <sub>2</sub>	He	N <sub>2</sub>
$n$ (m <sup>-3</sup> )	10 <sup>20</sup> -10 <sup>21</sup>	10 <sup>20</sup> -10 <sup>21</sup>	10 <sup>20</sup> -10 <sup>21</sup>
$\sigma$ (10 <sup>-19</sup> m <sup>2</sup> )	2.62	2.35	4.16
$\ell_{\text{mfp}}$ (m)	0.0027-0.027	0.003-0.03	0.0017-0.017

Table 4.1: Parameters for Density Pileup

#### Pileup Region Model

Estimating the extent and magnitude of the pileup involves evaluating how the density from cone 1 penetrates into cone 2. To first order, this pileup should be confined to the scale of the mean free path,  $\ell_{\text{mfp}}$  and conserve mass. To satisfy these basic constraints, the pileup model is constructed such that the interpenetrating

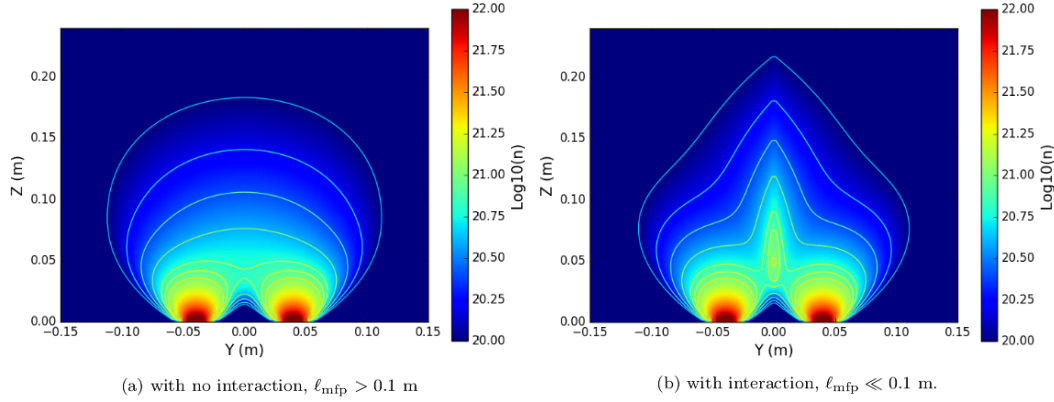


Figure 4.4: Density profiles for (a) direct superposition of two gas cone profiles and (b) modeled gas profile with finite neutral mean free path (Eq. 4.2)

density is compressed to an exponential profile with local characteristic length,  $\ell_{\text{mfp}}(z)$ :

$$\rho_{\text{pileup}}(x, y, z) = M(x, z) \frac{e^{-|y|/\ell_{\text{mfp}}}}{\ell_{\text{mfp}}} \quad (4.2)$$

$$M(x, z) = \int_0^{\infty} \rho(x, y' + y_0, z) dy'. \quad (4.3)$$

This corresponds to integrating the density from cone 1 (e.g. left cone at  $y = -y_0$ ) that penetrates the  $XZ$ -plane at each height, and redistributing it in an exponential profile with characteristic length,  $\ell_{\text{mfp}}(x, 0, z)$ . The process is mirrored for cone 2. The estimated density pileup from this exponential profile increases the apex density by a factor of 1.6 relative to the non-interacting case. Figure 4.4 highlights the difference between the case of no interaction  $\ell_{\text{mfp}} > 0.1$  m, and the pileup region model,  $\ell_{\text{mfp}} \ll 0.1$  m: a pileup region creates peaked density contours as distinct from the flat profile of a direct superposition. For the gas cones and densities described here, this model predicts that the pileup effect is only significant for valve separation distances less than 12 cm.

Although this is an ad hoc model, 2D measurements of the FlareLab initial density profile [89, 90, 132] show a peaked density distribution, with contours very similar to Figure 4.4b, indicating a comparable pileup region at the loop apex. This pileup model is used in Section 4.5 for the initial conditions of a 3D MHD simulation of the experiment.

## Hoop Force

The hoop force is an outward radial force present in all curved current channels. This force exists because the internal magnetic pressure of a current loop is greater than the exterior magnetic pressure. The equation of motion for an infinitesimal segment of a circular current (length  $ds$ , major radius  $R$ , minor radius  $a$ , and average mass density  $\bar{\rho}$ ) is given by

$$F_{\text{hoop}} ds = \ddot{R} \bar{\rho} \pi a^2 ds \quad (4.4)$$

$$F_{\text{hoop}} = \frac{\mu_0 I^2}{4\pi R} \left[ \ln \left( \frac{8R}{a} \right) - 2 + \frac{l_i}{2} \right], \quad (4.5)$$

where  $I$  is the current flowing through the plasma loop, and  $l_i$  is a constant of order unity related to the internal current distribution [46, 125]. Approximating the term in square brackets in Eq. 4.5 as constant and assuming a linearly rising current, the major radius expands quadratically with time:  $R(t) \propto t^2/\sqrt{\bar{\rho}}$  [125]. However, sections of the loop with higher density will accelerate more slowly and lag behind the global expansion.

## 4.4 Experimental Results

Several observed features on the Caltech experiment indicate the presence of a density pileup at the loop apex. The first of these is the presence of a localized bright region at the loop apex; this bright region can be detected from fast camera images as early as 500 ns after the breakdown. Since the apex is 6 cm away from each footpoint, the plasma at the footpoints does not have time to travel to the apex in 500 ns ( $v_A = 3 \cdot 10^4$  m/s,  $6 \text{ cm}/v_A = 2 \mu\text{s}$ ). Consequently, this feature must already be present in the neutral density. Figure 4.5 shows an image of this bright apex feature for a Nitrogen loop 1.5  $\mu\text{s}$  after breakdown. This bright feature at the loop apex extends beyond the major radius in an expanding cone. This expansion of the pileup region width at greater heights is consistent with the increasing mean-free path further away from the fast-gas nozzles.

The second observation is that the loop apex always lags behind during expansion, forming a heart-shaped dip. This expansion is driven by the hoop force described in Section 4.3. This dip is unusual as it is a large, extremely reproducible feature. It is always pointed downward, remains a similar size, and appears consistently for all gases used ( $\text{H}_2$ , He, Ar,  $\text{N}_2$ ). The dip moves slower than the leading edge of the loop and creates a significant deformation from circular expansion. Figure 4.6a shows the evolution of this apex dip for a  $\text{N}_2$  loop.

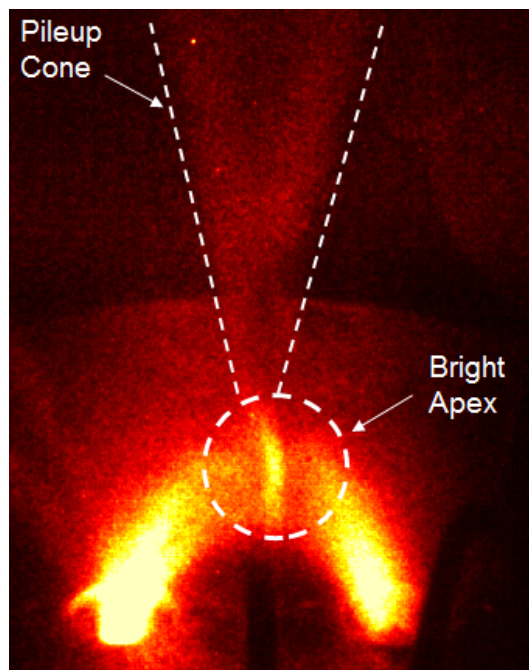


Figure 4.5: Photograph of the loop at  $1.5 \mu s$  after breakdown. The white dashes mark the bright feature at the loop's apex and pileup cone at the midplane

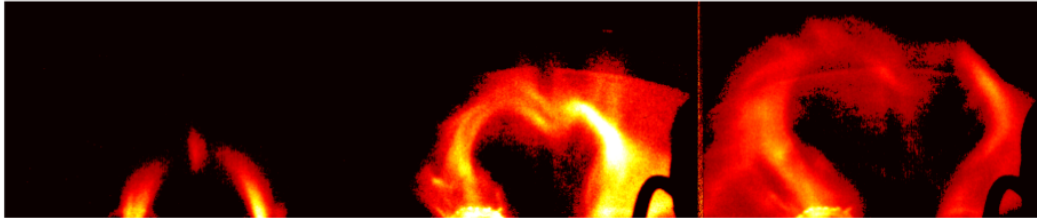
We can also control the shape and location of this apex dip by varying the gas output of each fast-gas valve. For the symmetric gas output, the dip appears to be sharper and larger when the gas density output is higher, as shown in Figure 4.7. If the output of the fast-gas valves differ significantly, the pileup region is shifted away from the footpoint with greater gas output and towards the footpoint with weaker gas output. Figure 4.8 shows superimposed images of a shot with higher gas output on the right footpoint (red) and a shot with higher gas output on the left footpoint (cyan). The shift of the bright apex feature is about 3 cm and highly reproducible.

Lastly, when creating plasma loops from a uniform gas backfill, both the bright apex feature and the heart shape are not observed. Figure 4.6b shows the evolution of a loop created with uniform Hydrogen backfill.

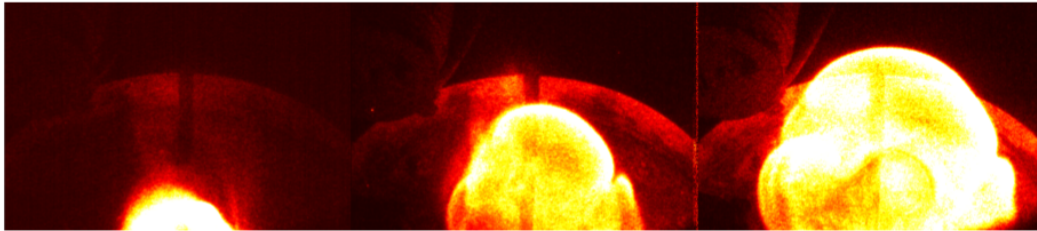
These observations demonstrate that the apex dip depends strongly on the initial neutral gas profile.

#### 4.5 MHD Simulation of the Apex Dip

Simulations of density profiles with a pileup region were performed to confirm that this perturbation would reproduce the shape and velocity of the experimental loop.

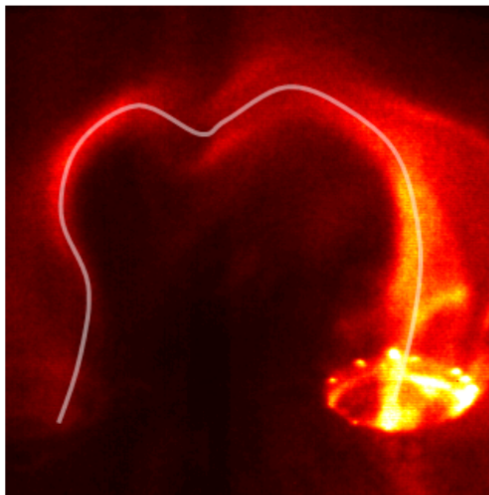


(a) Using fast-gas valves (Gas = N)

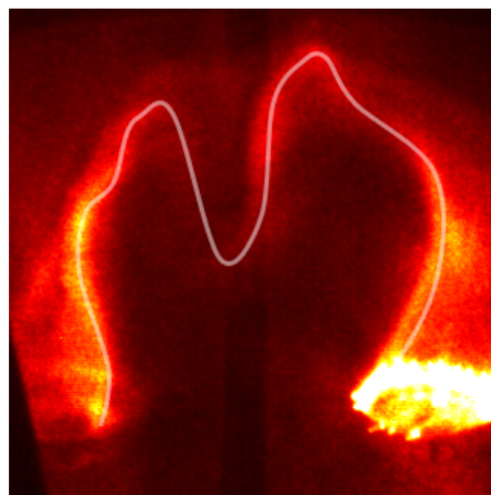


(b) Using uniform background gas (Gas = H)

Figure 4.6: Plot shows the evolution of two different initial density profiles. (a) Standard initial conditions with two colliding cones of gas supplied by nozzles in electrodes. (b) Non-standard conditions with uniform background gas supplied from sources on opposite side of chamber. Without the gas cones from the nozzles, the apex dip feature disappears



(a) Smooth dip from low gas density output



(b) Sharp dip from high gas density output

Figure 4.7: Comparison of dip shape for two different gas outputs. Loop axis is manually traced with white lines to highlight differences (Gas = H)

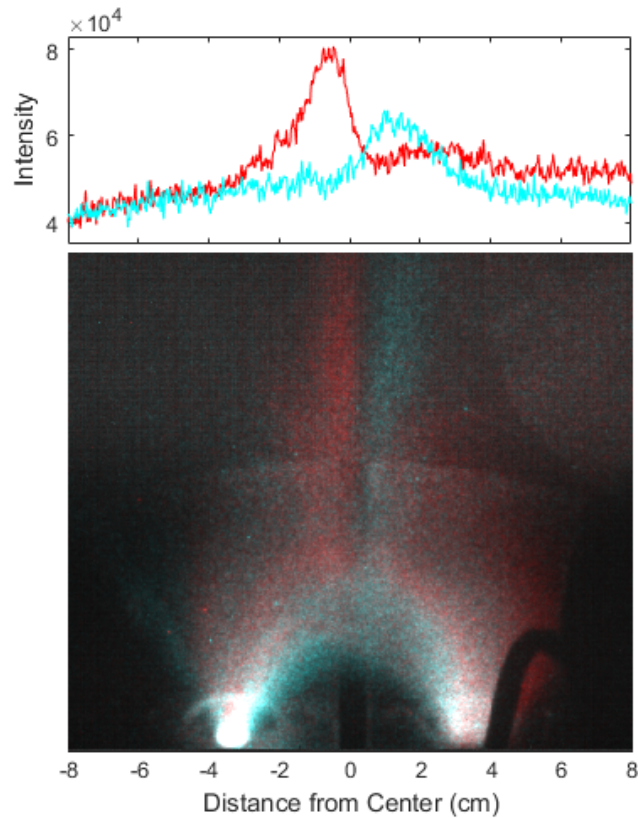


Figure 4.8: (top) Plot of vertically integrated pixel values. (bottom) Superimposed images of a shot with higher gas output on the right footpoint (red) and a shot with higher gas output on the left footpoint (cyan) (Gas = He)

The spatial domain is a mesh cube with 96 grid points in each Cartesian dimension and non-reflecting outflow boundary conditions. The description of the simulation can be found in Section 3.2.

The simulation uses the initial density profile shown in Figure 4.4. In addition to the two gas cones, a high density wall region is added below the footpoints to simulate the anchoring effects of the electrodes. The initial background magnetic field (bias field) is generated by specifying a set of loop currents in a half-circle configuration below the electrode plane. Diffuse poloidal flux is continuously injected into the simulation domain corresponding to the electric current measured in the experiment. A detail of the initial magnetic field and the current injection were described in Section 3.2.

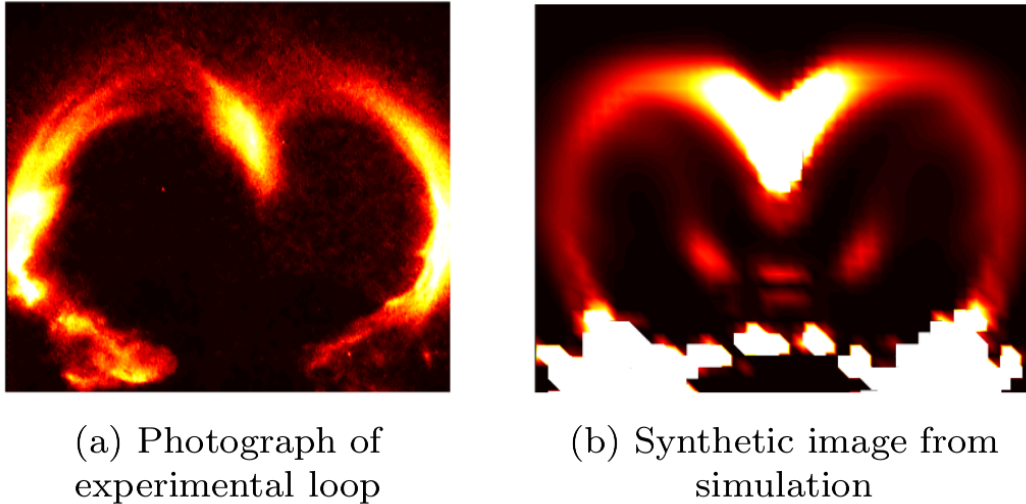


Figure 4.9: Comparison of the cusp shape between experiment (left) and simulation (right)

### Simulation Results

Using an initial density with a pileup region, the simulation replicates the shape and expansion velocity of the loop. Figure 4.9a shows the image of the loop with the dip at the apex and Figure 4.9b shows a synthetic image from the simulation where intensity is proportional to current density and number density squared ( $I \propto J\rho^2$ ). Figure 4.10 shows that the apex position of the simulated loop also closely matches that of the experiment. The evolution comprises of three stages. First, after the initial brightening of neutral gas as shown in Figure 4.5, magnetic forces generate axial flow and pinch to form a collimated loop [7], resulting in the initial decrease in apex height. Subsequently, the apex is accelerated by the hoop force [125], colliding with the neutral pileup region. Lastly, the apex is accelerated to its terminal velocity from the high magnetic curvature forces, illustrated in Figure 4.11, present in the cusp.

Given the good match in shape and velocity, the simulation demonstrates that a pileup region is consistent with the observed loop evolution.

### 4.6 Discussion

The data presented provide strong evidence that the dip feature is in fact a cusp rather than a helix. The proposed cusp formation mechanism (a neutral pileup region) resolves all of the inconsistencies with the helical interpretation and achieves excellent agreement with observation and simulation. This new understanding of

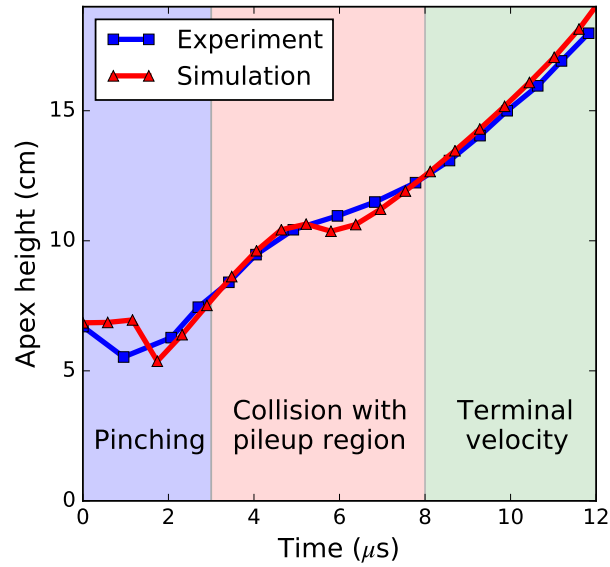


Figure 4.10: Evolution of the loop apex position in 3 stages: (i) the minor radius undergoes pinching before expansion (ii) the loop collides with the pileup region temporarily slowing down (iii) the magnetic curvature forces of the cusp re-accelerate the apex to a terminal velocity

the experiment has implications for both future experiments and solar flux ropes.

### Neutral Pileup Regions

Most other experiments with fast-gas valves do not have the appropriate densities or length scales necessary to create density pileup regions. However, as in our experiments, such an effect can greatly perturb the initial conditions and should be considered in the design of future plasma experiments. The high reproducibility and simple control of the feature suggests that future experiments could utilize such pileup regions to study the effect of density perturbations, instabilities, or localized collisions between plasma and neutral gas.

### Relevance of Dip Feature in Solar Context

Since the plasma loop can be described by ideal MHD, its behavior can be scaled. This scaling allows for three free parameters  $a_1$ ,  $a_2$ ,  $a_3$  with the following invariant transformations:  $L_0/a_1 \rightarrow L'$ ,  $\rho_0/a_2 \rightarrow \rho'$ ,  $B_0/\sqrt{a_3} \rightarrow B'$ ,  $P_0/a_3 \rightarrow P'$ ,  $\frac{1}{a_1}\sqrt{\frac{a_3}{a_2}}t_0 \rightarrow t'$ ,  $\sqrt{\frac{a_2}{a_3}}v_0 \rightarrow v'$ ,  $\frac{a_1a_2}{a_3}g \rightarrow g'$  [116]. These transformations provide a one-to-one correspondence between systems allowing simulated and experimental

plasmas to be scaled to an equivalent system at the space plasma scale. Table 4.2 shows the characteristic parameters of the experiment, typical coronal loop parameters, and experimental parameters scaled to the solar environment using  $a_1 = 2.5 \cdot 10^{-8}$ ,  $a_2 = 10^8$  and  $a_3 = 10^4$ . With the notable exception of gravity, the experimental parameters scale well to the solar case. However, the effective gravity associated with the acceleration provides useful insight into gravitational effects.

Experiment	$B = 3000 \text{ G}$	$L = 0.5 \text{ m}$
	$\rho = 10^{-4} \text{ kg m}^{-3}$	$\tau = 20 \mu\text{s}$
	$g = 10 \text{ m s}^{-2}$	$P = 300 \text{ Pa}$
	$v_A = 3 \times 10^4 \text{ m s}^{-1}$	$\beta = 0.01$
Scaled Exp.	$B = 30 \text{ G}$	$L = 2 \times 10^7 \text{ m}$
	$\rho = 10^{-12} \text{ kg m}^{-3}$	$\tau = 7 \text{ s}$
	$g = 3 \times 10^{-3} \text{ m s}^{-2}$	$P = 0.03 \text{ Pa}$
	$v_A = 3 \times 10^6 \text{ m s}^{-1}$	$\beta = 0.01$
Coronal Loop	$B = 50 \text{ G}$	$L = 2 \times 10^7 \text{ m}$
$T = 1.5 \text{ MK}$	$\rho = 10^{-12} \text{ kg m}^{-3}$	$\tau = 5 \text{ s}$
	$g = 300 \text{ m s}^{-2}$	$P = 0.01 \text{ Pa}$
	$v_A = 4 \times 10^6 \text{ m s}^{-1}$	$\beta = 0.002$

Table 4.2: Dimensionless scaling of Caltech parameters to solar loops.  $g$  here refers to an actual gravitational acceleration not the effective one.

The presence of a dense, cusp feature in the experimental flux rope is similar to common features of solar prominences. It is well established that solar prominences have inhomogeneous density along their axis and that the highest density is localized near the apex [4, 77, 110]. Despite these measurements of density modulation, many models of coronal structures assume constant density [3, 60, 62, 137, 151]. The experimental results indicate that density perturbations can result in large distortions of an erupting flux rope, even in the absence of significant pressure or gravity forces. Consequently, a more realistic density profile should be considered when attempting to precisely model erupting flux ropes or CME's.

Furthermore this denser apex material is thought to sit in a shallow magnetic dip [45, 54], a similar but less extreme version of the experimental cusp. Many of the models simulating this apex density are purely hydrodynamic [1] and ignore magnetic effects from changes in minor radius. In future experiments, these theories could be tested by appropriate acceleration of the loop apex, imposing an effective gravity with

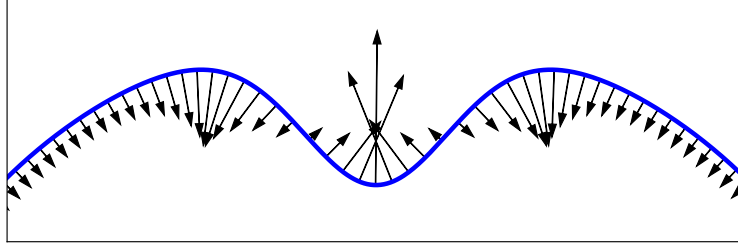


Figure 4.11: Magnetic tension forces ( $\mathbf{B} \cdot \nabla \mathbf{B}$ , arrows) plotted for an apex dip of a thin flux rope (blue line). Central cusp area has strong vertical magnetic forces because of the high curvature

appropriate scaling to solar gravity. The acceleration from loop expansion with current parameters ( $5 \cdot 10^7 \text{ m/s}^2$ ) scales to an effective gravity of  $10^4 \text{ m/s}^2$  at the coronal scale, 40 times larger than solar gravity ( $270 \text{ m/s}^2$ ).

### Suppression of Kink Instability

The last mechanism of interest is the effect of the pileup region on the kink instability. The kink instability is a current-driven instability which drives exponential growth of long-wavelength helical perturbations. The instability threshold is reached when the magnetic field lines complete more than one twist around the major axis. The kink stability is usually defined with respect to the safety factor,  $q$ :

$$q = \frac{2\pi a B_\phi}{L B_\theta}, \quad (4.6)$$

where  $q$  is the safety factor,  $L$  is the length of the major axis,  $a$  is the minor radius,  $B_\phi$  is the toroidal field, and  $B_\theta$  is the poloidal field. Full toroids and other line-tied flux-rope experiments [15, 108], become unstable for  $q < 1$ . B-field measurements of the loop from  $t = 10 - 14 \mu\text{s}$  give  $B_\phi(a) = 250 - 560 \text{ G}$ ,  $B_\theta(a) = 200 - 350 \text{ G}$ ,  $a = 2 - 4 \text{ cm}$ . From images we know that the length of the loop is between 40-56 cm in this time-frame. These values imply an unstable safety factor,  $q \approx 0.5$ . Consequently, it is surprising that the loop does not exhibit more violent kinking behavior.

We propose that the high density region at the loop apex suppresses the kink since the unstable kink mode has an anti-node at the apex and the high density region acts like a stationary node. This effectively halves the axial length available to kink and doubles the safety factor. Similar suppression of the longest wavelength kink modes by high density regions has been seen before in astrophysical jet simulations [103] and experiments [59].

*Chapter 5***REVERSE CURRENT MODEL FOR CORONAL MASS  
EJECTION CAVITY FORMATION**

Magnus A Haw, Pakorn Wongwaitayakornkul, Hui Li, and Paul M Bellan. “Reverse Current Model for Coronal Mass Ejection Cavity Formation”. In: *The Astrophysical Journal Letters* 862.2 (2018), p. L15. DOI: <https://doi.org/10.3847/2041-8213/aad33c>.

M.A.H. proposed the initial idea of the model inspired by the simulation. P.W. and M.A.H developed the simulation. P.W. designed and conducted the experiment. H.L. provided the simulation source code. P.W., M.A.H., and P.M.B discussed and wrote the manuscript.

We report here a new model for explaining the three-part structure of coronal mass ejections (CMEs). The model proposes that the cavity in a CME forms because a rising electric current in the core prominence induces an oppositely directed electric current in the background plasma; this eddy current is required to satisfy the frozen-in magnetic flux condition in the background plasma. The magnetic force between the inner core electric current and the oppositely directed induced eddy current propels the background plasma away from the core creating a cavity and a density pileup at the cavity edge. The cavity radius saturates when an inward restoring force from magnetic and hydrodynamic pressure in the region outside the cavity edge balances the outward magnetic force. The model is supported by (i) laboratory experiments showing development of a cavity as a result of the repulsion of an induced reverse current by a rising inner core flux rope current, (ii) 3D numerical MHD simulations that reproduce the laboratory experiments in quantitative detail, and (iii) an analytic model that describes cavity formation as a result of the plasma containing the induced reverse current being repelled from the inner core. This analytic model has broad applicability because the predicted cavity widths are relatively independent of both the current injection mechanism and the injection timescale.

## 5.1 Introduction

Coronal cavities were first observed in white light images in the late 1960's as dark, croissant shaped regions above stable and erupting solar prominences [118, 148, 150]. These density cavities are of significant interest because they are observable features that could give insight into the magnetic structure of prominences and so provide better predictability for coronal mass ejections (CMEs). Understanding and predicting CMEs is of increasing importance given the potential danger they pose to spacecraft, aircraft communications, and the electrical grid. Despite limited magnetic measurements, there exist extensive white light observations of CMEs from satellite coronagraphs. These images consistently display a three-part structure: (i) a bright shock-like leading edge followed by (ii) a dark, croissant-shaped density cavity and (iii) a bright core corresponding to the core prominence [25, 26, 38, 118]. The second frame of Figure 5.1a identifies these parts on a typical CME. Although several numerical simulations of CMEs have successfully reproduced a three-part structure [32, 63, 87, 137, 138], it is still unclear how and why the cavity structure forms [41].

The formation of a similar density cavity structure was evident in cylindrical shock tube experiments [58, 144]. In these experiments, an increasing axial current induces a reverse current shell, which expands outwards due to the mutual repulsion of the anti-parallel currents, leaving behind a density cavity between the core and reverse currents. This induced reverse current layer is a consequence of the frozen-in condition of MHD: the increasing azimuthal field from the current channel necessarily induces an equal and opposite shell of reverse current to preserve the magnetic flux in the background plasma. This reverse current mechanism was first described in Greifinger and Cole [44] but has never before been applied to CMEs.

In this chapter, we present measurements of this reverse current mechanism in arched flux rope experiments and 3D MHD flux rope simulations which dimensionlessly scale to CMEs. These results show the formation of a density cavity between an increasing core current and a reverse current shell. A simple analytic model for the cavity formation is derived by extending the shock solution from Greifinger and Cole [44] to a layer of finite width. This model is then shown to be in good agreement with experiment, simulation, and CME observations.

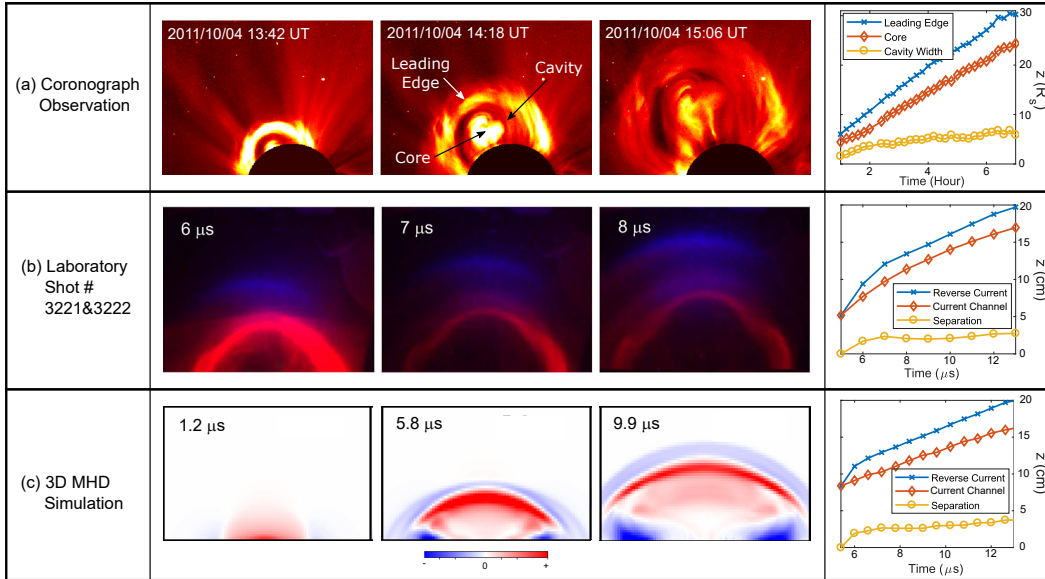


Figure 5.1: (a) Image sequence of the three-part CME captured by LASCO-C3 on 2011 October 4. This sequence shows a nearly edge on view of the current channel instead of the perpendicular views shown from the experiment. (b) Image sequence of composite multiwavelength fast camera images of laboratory experiment. Each image consists of two bandwidths: filtered  $H\alpha$  in blue (H-dominated) and visible light in red (Ar-dominated). (c) Cross-sectional plots of simulated current density in the horizontal direction ( $J_y$ ) showing the propagation of the main current (red) and an induced reverse current layer (blue). For each case, the height evolution of leading edge/reverse current (blue), core/current channel (red) and cavity width/separation (yellow) are plotted in the last column.

## 5.2 Prefilled Single Loop Experiment

The experiment generates an expanding flux rope (argon) which collides with a background plasma (hydrogen). The apparatus consists of a magnetized plasma gun mounted at the end of a 1.6 meter-long, 0.92 meter-diameter vacuum chamber [8, 46, 125, 157]. Figure 5.2a shows the apparatus and Cartesian coordinate system. Two solenoids, one beneath each electrode, are pulsed to produce an arched magnetic field, similar to a horseshoe magnet. This background field ranges from 0.3 T at the footpoints to 0.06 T at the loop apex. Above each solenoid there are gas nozzles connected to fast valves. These valves are pulsed, releasing diverging flows of argon neutral gas in two expanding cones with number density  $10^{19} - 10^{22} \text{ m}^{-3}$ . A neutral hydrogen prefill,  $n = 3 \times 10^{21} \text{ m}^{-3}$ , is added to provide a background gas. Finally, a 59  $\mu\text{F}$  capacitor charged to 3.6 kV is discharged across the electrodes, ionizing the neutral gas and driving up to 30 kA for  $\sim 10 \mu\text{s}$  through the plasma. Less than 2 kA is carried by the bright collimated loop structure with the remainder of

the current traveling in a broad, diffuse outer envelope. The collimated loop has  $\beta = 2\mu_0 n_i \kappa T / B^2 \sim 0.1$ , for  $n_i = 5 \times 10^{19} \text{ m}^{-3}$ ,  $\kappa T = 2 \text{ eV}$ , and  $B = 200 \text{ G}$ .

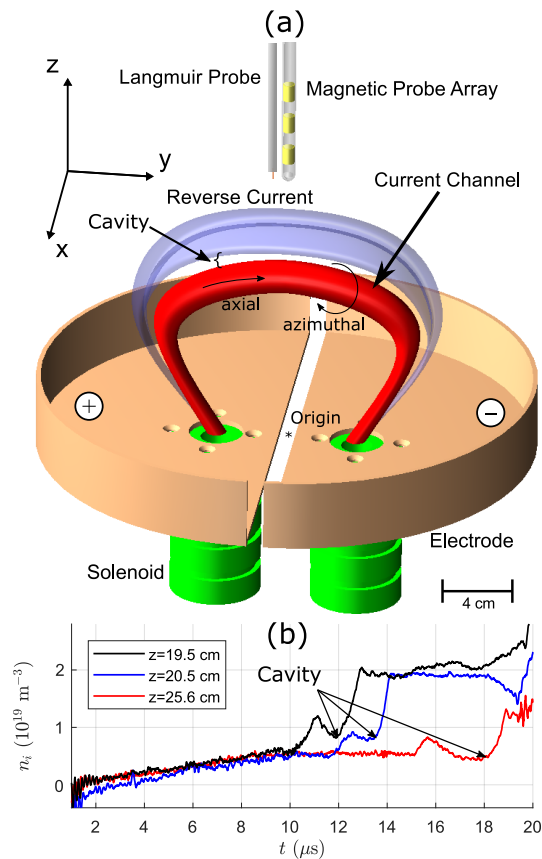


Figure 5.2: (a) Schematic diagram of the experimental setup showing the primary current channel (red), the induced reverse current layer (blue), electrodes (copper), solenoid (green), magnetic probe array (yellow), and Langmuir probe (grey). (b) Plot of density from Langmuir probe at three locations shows formation of density cavity

The dynamics of the current channel and the reverse current are captured by correlating a sequence of visible light images using a multiple-frame fast camera with measurements made by Langmuir probes and magnetic probes. The false color images are superimposed with filtered  $H\alpha$  in blue (H-dominated) and visible light in red (Ar-dominated). Using hydrogen gas for the expanding flux rope produced equivalent cavity structures (i.e.,  $\sim 2 \text{ cm}$  separation) but argon was chosen due to its slower expansion speed and better imaging properties. Figure 5.1b shows the formation and subsequent separation of the reverse current layer from the driving current channel. Langmuir probe measurements shown in Fig. 5.2b confirm that the dark cavity region in the experimental images is a region of density depletion

(30-50% lower than the core and reverse current layer). Magnetic measurements from B-dot probes show that the blue feature in Figure 5.1b contains a current oppositely directed to that of the primary injected current channel (red feature). The time dependence of apex positions of the current channel and reverse current layer are tracked from the images and plotted in the far right of Figure 5.1b and are labelled as current channel (i.e., core as in Fig. 5.1a) and reverse current (i.e., leading edge as in Fig. 5.1a). Since these features have a non-negligible thickness, the locations of the apexes are chosen to be at the center of the feature on the  $z$ -axis. The separation (i.e., cavity width as in Fig. 5.1a) between the two features is also plotted. The cavity width, defined by the distance between the two apexes, grows quickly and reaches an asymptotic value of  $2 \pm 0.5$  cm. The projected emission in the  $yz$ -plane shows that the curvature of the reverse current layer is similar to that of the current channel. The following paragraph describes how the reverse current is calculated from magnetic probe data.

The time dependence of  $\mathbf{B}$  seen by the probe is from convection rather than diffusion and images show little change in the different features as they move by the probes, i.e.,  $\partial/\partial z \leftrightarrow v_z^{-1}\partial/\partial t$ . The horizontal current density can therefore be estimated from the time dependence of the magnetic field, i.e.,  $J_y = (\nabla \times \mathbf{B}) \cdot \hat{y}/\mu_0 = (\partial_z B_x - \partial_x B_z)/\mu_0 \approx (\partial_t B_x)/(\mu_0 v_z)$  where  $v_z \approx 13 - 15$  km s<sup>-1</sup> as measured from feature tracking in fast camera images. Additional magnetic measurements in the  $xz$ -plane confirm that the center of the flux rope has spatial variation principally in the  $z$ -direction with much less variation in the  $x$ -direction ( $\partial_x B_z \ll \partial_z B_x$ ). Figure 5.3 shows experimental  $J_y$  profiles calculated from  $B_x(t)$  measurements at 3 locations ( $x, y = 0, z = 17.5, 19.5,$  and  $21.5$  cm); the inset shows a zoomed-in view of the reverse current, and indicates that this reverse current layer appears spatially ahead of the main current. The spatial distribution and motion of the primary and reverse currents match the features observed in the fast camera images.

The current channel in the experiment expands due to the hoop force, a consequence of greater magnetic pressure on the inboard side of the loop than on the outside [125]. During this expansion, the current channel collides with the background gas, inducing a reverse current layer of ionized hydrogen.

### 5.3 Simulation

To gain further insight into this reverse current layer, the experimental setup was simulated using a 3D MHD equation solver code, a subset of the Los Alamos

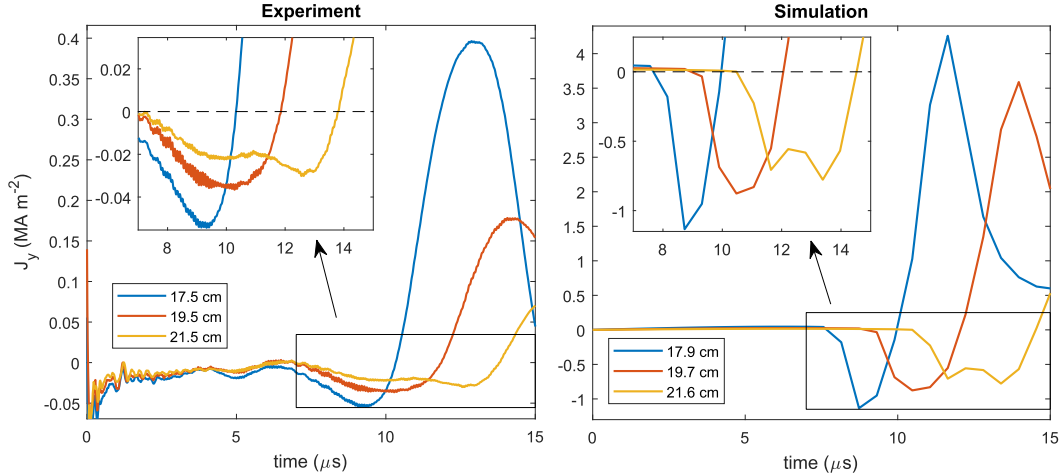


Figure 5.3: (Left) Calculated  $J_y(t)$  profiles at three locations show the distribution and propagation of the reverse current and the current channel in the experiment. Inset shows reverse currents in more detail. (Right) The equivalent plot of  $J_y$  obtained from the simulation at 3 locations analogous to those in the experiment.

COMPUTational Astrophysics Simulation Suite (LA-COMPASS) [80]. This code is described in previous papers simulating the Caltech plasma jet experiment [167] and the arched flux rope experiment [157]. The ideal MHD code evolves a set of dimensionless parameters: density  $\rho$ , pressure  $P$ , magnetic field  $\mathbf{B}$ , and velocity  $\mathbf{v}$  on a Cartesian grid with non-reflecting outflow boundary conditions.

The initial density profile consists of (i) exponential cones emerging from the gas nozzles at each footpoint<sup>1</sup>, (ii) a uniform background gas  $\rho_b = 1.0 \times 10^{-5} \text{ kg m}^{-3}$ , and (iii) a high density region below  $z = 0$  to simulate the anchoring effect of the electrode boundary. The neutral density in the  $z > 0$  region is

$$\rho(x, y, z) = \rho_0 \left( \frac{z_0}{z + z_0} \right)^3 \left( \sum_{i=-1,1} \exp \left\{ \left[ -\frac{K(x^2 + (y - (-1)^i y_0)^2)}{(z + z_0)^2} \right] \right\} \right) + \rho_b, \quad (5.1)$$

where  $\rho_0 = 4.8 \times 10^{-3} \text{ kg m}^{-3}$  is the density at the footpoint,  $K = \tan \alpha \sqrt{\log 2} = 1.1$ ,  $\alpha \approx 54^\circ$  is a half cone angle,  $y_0 = 0.04 \text{ m}$  is the footpoint location,  $z_0 = 0.01 \text{ m}$  is an offset to avoid singularities, and  $\rho_b = 1.0 \times 10^{-5} \text{ kg m}^{-3}$  is the background density. Initial pressure is defined such that  $P = (\rho - \rho_b) \kappa T / m_i$  where  $m_i =$  mass of hydrogen ion, and  $\kappa T = 2 \text{ eV}$ ; the term  $\rho_b$  is subtracted because the background plasma is cold. The plasma is assumed to be initially at rest.

<sup>1</sup>Without background gas, the cone density decays as  $z^{-2}$  [165]. The presence of background gas impedes the expansion of gas exiting from the nozzles so the gas cone density decays more rapidly with increasing  $z$ ; this more rapidly decaying density was modeled as having a profile scaling as  $z^{-3}$ .

The background magnetic field is constructed from a set of 10 current loops arranged in a half-circle below the footpoints, each with a current of  $I = 631$  kA (see Figure 9 of Wongwaitayakornkul et al. [157]). This arrangement produces a horseshoe-magnet field topology with a magnitude ranging from 0.2 T at the footpoints to  $10^{-3}$  T at the upper edge of the simulation. The field from each current loop is calculated from a truncated series approximation for the vector potential of an infinitely thin loop [124]. This truncation gives an analytic expression for a current loop which is non-singular and divergence-free.

From  $t = 0$  to  $t = 10 \mu\text{s}$ , azimuthal flux is added to the domain to match the rising experimental current,  $I_{\text{exp}}(t) \approx I_0 \sin(2\pi t/T)$  where  $T = 40 \mu\text{s}$  and  $I_0 = 30$  kA. This azimuthal magnetic field corresponds to a diffuse arched current constructed from the superposition of 110 current loops and conforms roughly to the shape of the gas cones (i.e., a  $54^\circ$  flared angle at the footpoints). The spatial distribution of the injected current was selected to match the experimental initial conditions, but due to the self-collimating property of parallel currents, the precise spatial profile of the injected current is not critical. The diffuse current is injected via a source term added to the induction equation [80, 167]. This incremental addition of flux does not significantly perturb the system at a given time step but slowly increases the poloidal flux, corresponding to a rising current. This is the same injection profile as mentioned in 3.2.

This setup simulates a flux rope with increasing current that expands into a background plasma. As observed in the experiment, the simulated current channel produces a reverse current layer as the current channel collimates and expands outward. Figure 5.1c plots a time series of  $J_y$  from the numerical simulation in the  $yz$ -plane, showing a reverse current layer propagating in front of the main current. The shape and position of the main current and reverse current layer are in reasonable agreement with the experiment ( $\pm 20\%$ ) as can be seen by comparing Figure 5.1b and 5.1c. Figure 5.3 compares the current density  $J_y$  in the simulation and in the experiment at the three magnetic probe locations. The experimental current density  $J_y$  (left) is broader than in the simulation (right) because of magnetic diffusion from finite resistivity in the experiment. However, the morphology of the profiles are quite similar, as both show a reverse current layer propagating ahead of the core current channel.

#### 5.4 Snowplow Model for Reverse Current

This model extends the infinitely thin snowplow analysis from Greifinger and Cole [44] to a finite-width reverse current layer and has three key features: an increasing current channel, an expanding reverse current layer, and a density cavity between the current channel and the reverse current layer.

##### Assumptions

Figure 5.4 illustrates the model. The configuration consists of a vertical ( $\hat{y}$ ) cylindrical current channel with finite radius  $a$  and increasing total current  $I(t)$  in a uniform plasma of density  $\rho_0$ , magnetic field  $B_0\hat{y}$ , and pressure  $P_0$ . The current channel is surrounded by a shell/layer of induced reverse current at position  $b(t)$ , corresponding to the shielding effect of the background plasma. The inner radius of this shell of reverse current is initially at position  $b(0) = a$  and the shell is assumed to have a constant thickness  $\delta$  and a uniform current density  $J_y = -I/\sigma$  across its width, where  $\sigma = \pi(2\delta b + \delta^2)$  is the cross-sectional area of the shell. The motion of the reverse current shell is governed by an expansive force resulting from the mutual repulsion of the oppositely directed currents competing with a restoring force from the background pressure and background magnetic field external to the shell. The cavity region is assumed to have negligible density and pressure (i.e., snowplow assumption). Consequently, there is no outward force on the reverse current from pressure inside the cavity.

The total expansive force-per-length  $f_e$  is obtained by integrating  $-J_y B_\phi$  over the reverse current layer:

$$\begin{aligned}
 f_e &= - \int_{r=b}^{r=b+\delta} J_y B_\phi 2\pi r dr \\
 &= - \frac{2\pi}{\mu_0} \int_{r=b}^{r=b+\delta} B_\phi \frac{\partial}{\partial r} (r B_\phi) dr \\
 &= \frac{\mu_0 I^2}{\sigma} \int_{r=b}^{r=b+\delta} \left( 1 - \frac{\pi(r^2 - b^2)}{\sigma} \right) dr \\
 &= \frac{\mu_0 I^2}{3\pi} \frac{3b + 2\delta}{(2b + \delta)^2}. \tag{5.2}
 \end{aligned}$$

Taking the limit  $\delta \rightarrow 0$  recovers the expression from Greifinger and Cole [44], i.e.,

$$\lim_{\delta \rightarrow 0} f_e = \frac{\mu_0 I^2}{4\pi b}. \tag{5.3}$$

The total confining force  $f_c$  is calculated as the product of the background pressure

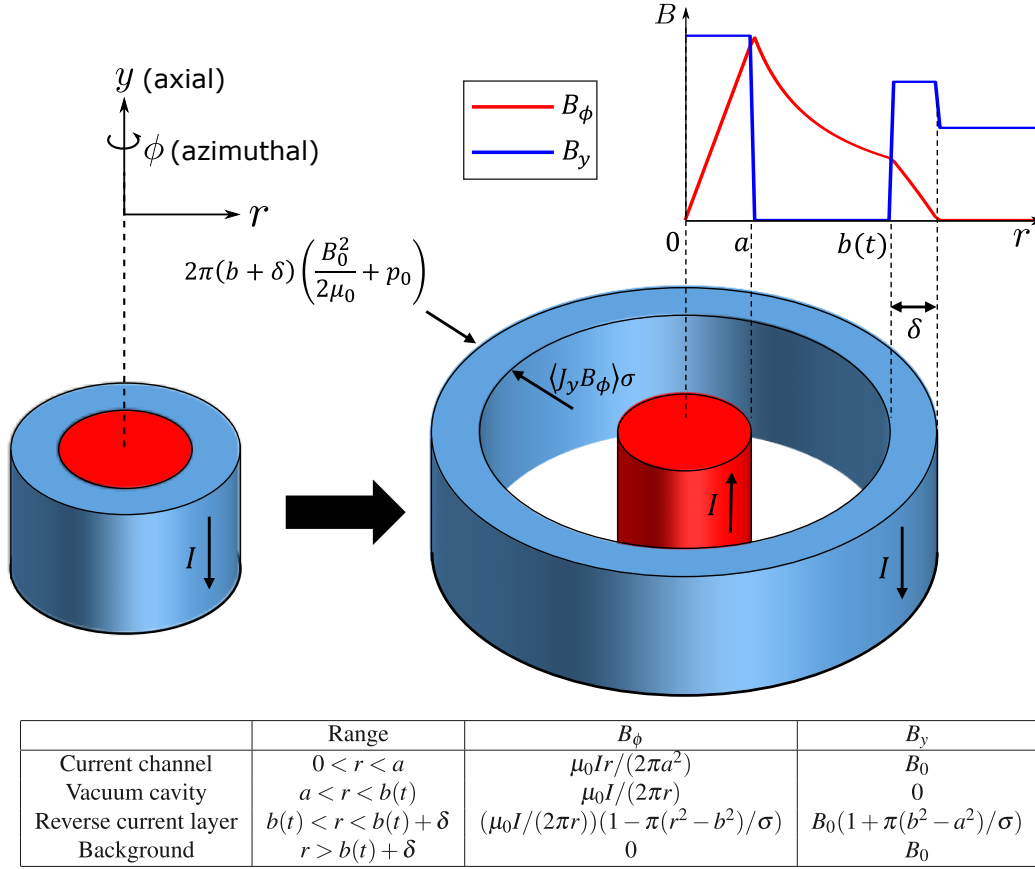


Figure 5.4: Illustration of the model. The current  $I$  is in the  $+y$  direction in the main current channel (red) and in the  $-y$  direction in the reverse current shell (blue). The reverse current shell has thickness  $\delta$  and expands radially forming a cavity region between  $a$  and  $b(t)$ . The plot shows the radial dependence of both the normalized axial field ( $B_y$ , blue) and normalized azimuthal field ( $B_\phi$ , red). The table lists radial ranges with their corresponding magnetic fields.

and the shell outer perimeter:

$$f_c = 2\pi(b + \delta) \left[ \frac{B_0^2}{2\mu_0} + P_0 \right]. \quad (5.4)$$

This gives the equation of motion for the expansion of the current layer to be

$$\frac{d}{dt} \left( M \frac{db}{dt} \right) = f_e - f_c. \quad (5.5)$$

Using the "snowplow" assumption, the mass-per-length  $M$  scales with the swept area, so

$$M = \rho_0 \pi \left( (b(t) + \delta)^2 - a^2 \right). \quad (5.6)$$

The full equation of motion for the current layer can therefore be written as

$$M\ddot{b} = \frac{\mu_0 I(t)^2}{3\pi} \frac{3b + 2\delta}{(2b + \delta)^2} - 2\pi(b + \delta) \left[ \frac{B_0^2}{2\mu_0} + P_0 \right] - \dot{M}\dot{b}. \quad (5.7)$$

The last term on the right hand side is a consequence of momentum conservation from the increasing mass of the layer. A complete void with  $B_y = 0$  and zero plasma pressure is not observed in the experiment. However, even without many of the features present in the continuous 3D system, the analytic model can characterize the bulk forces and predict cavity widths and internal currents for the experiment and simulation.

### Non-Dimensional Form and Equilibrium

Equation 5.7 can be put in dimensionless form to compare plasmas having different scales. The characteristic velocity is chosen to be the Alfvén speed  $v_A = B_0/\sqrt{\mu_0\rho_0}$  and the characteristic time is chosen to be the Alfvén crossing time  $\tau = a/v_A$ . This choice of normalization has three free parameters:  $B_0$ ,  $a$ , and  $\rho_0$  so Eq. 5.7 becomes

$$\bar{M}\ddot{\bar{b}} = \frac{\bar{I}^2}{3\pi} \frac{3\bar{b} + 2\bar{\delta}}{(2\bar{b} + \bar{\delta})^2} - \pi(\bar{b} + \bar{\delta}) [1 + \beta] - \dot{\bar{M}}\dot{\bar{b}}, \quad (5.8)$$

where normalized values are indicated with a bar, (i.e.,  $\bar{I} = I/I_0 = I\mu_0/(B_0a)$ ,  $\bar{M} = M/(\rho_0 a^2)$ ) and  $\beta = 2\mu_0 P_0/B_0^2$ ). In both the experiment and the simulation, the cavity width prescribed by Eq. 5.8 reaches equilibrium within a few Alfvén crossing times (i.e.,  $t \sim 5a/v_A$ ). This fast equilibration time implies that cavity widths are relatively independent of the current injection timescale. Solving for this equilibrium ( $\dot{\bar{b}} = 0$ ,  $\ddot{\bar{b}} = 0$ ) gives

$$\pi(\bar{b}_{eq} + \bar{\delta}) [1 + \beta] = \frac{\bar{I}^2}{3\pi} \frac{3\bar{b}_{eq} + 2\bar{\delta}}{(2\bar{b}_{eq} + \bar{\delta})^2}, \quad (5.9)$$

$$\bar{b}_{eq} = \frac{\bar{I}}{2\pi\sqrt{1+\beta}} - \frac{2}{3}\bar{\delta} + \left( \frac{\pi\sqrt{1+\beta}}{12\bar{I}} \right) \bar{\delta}^2 + O[\bar{\delta}^3]. \quad (5.10)$$

For  $\delta \ll b_{eq}$ , the solution is a simple pressure balance where  $B_\phi(b_{eq}) = B_0\sqrt{1+\beta}$ . In dimensioned quantities, the equilibrium cavity size is  $b_{eq} = \mu_0 I/(2\pi B_0\sqrt{1+\beta})$  where  $I$  is the main current and  $B_0$  is the background field. Since the dependence on plasma  $\beta$  is weak, and the mechanism is independent of the collisional mean free path, the effects should be similar across a wide range of plasma parameters.

### Core Acceleration

The effects of an accelerating frame can be quantified by substituting  $[b(t) - h(t)]$  for  $b(t)$  in the expansive term, where  $h(t)$  represents the height of the loop apex as a function of time, so Eq. 5.2 becomes

$$f_e = \frac{\mu_0 I^2}{3\pi} \frac{3[b(t) - h(t)] + 2\delta}{(2[b(t) - h(t)] + \delta)^2}. \quad (5.11)$$

This substitution effectively shifts the central current channel (the red cylinder in Figure 5.4) off-axis with speed  $\partial_t h(t)$ . However, for speeds  $\partial_t h(t) \ll v_A$ , the cavity width is not significantly affected and the cavity again reaches an equilibrium width within a few Alfvén crossing times. Equivalently, the system reaches a similar equilibrium width in a moving frame if the momentum conservation term  $\dot{M}\dot{b}$  is small compared to the magnetic terms. This limit is a reasonable approximation for the cases of interest and the next section will show that the cavity widths predicted by the stationary model agree well with the experiment, simulation, and CME observations. Consequently, the model can be used to infer the internal current  $I \approx 2\pi b_{eq} B_0 \sqrt{1 + \beta} / \mu_0$  from cavity width for both stationary flux ropes and flux ropes moving at sub-Alfvénic speeds.

### 5.5 Scaling to CMEs

The understanding gained from the experiment, simulation, and theory provide new insights for interpreting the three-part structure of CMEs. The leading edge, cavity, and core elements of a CME respectively correspond to the reverse current layer, the cavity and the central current channel of the model. This new interpretation is a flux rope model which identifies where currents are flowing: the main current channel is the core, the cavity is a region of expanding azimuthal flux around the main current channel, and the leading edge corresponds to a compressed reverse current layer between the core current and background plasma.

It is important to evaluate how the experiment and simulation scale to the solar situation. To do this, we follow the MHD scaling method in Ryutov, Drake, and Remington [116] and so normalize each system using the current channel minor radius  $a$  as a reference length, a reference magnetic field  $B_0$ , and a reference density  $\rho_0$ . The reference time for normalization is then given by  $\tau_0 = a\sqrt{\mu_0\rho_0}/B_0$ . The reference parameters for both the simulation and experiment are  $a = 5.0 \times 10^{-3}$  m,  $B_0 = 0.01$  T,  $\rho_0 = 2 \times 10^{-7}$  kg m<sup>-3</sup>,  $\tau_0 = 2.5 \times 10^{-7}$  s. The reference parameters for the 2011 October 4 CME event are  $a = 1.0 \times 10^9$  m,  $B_0 = 1.0 \times 10^{-5}$  T [6, 91],  $\rho_0 = 3.0 \times 10^{-17}$  kg m<sup>-3</sup>,  $\tau_0 = 710$  s. The density is estimated from a typical CME

mass  $M = 10^{12}$  kg [145] divided by the core volume,  $\pi a^2 \pi R$ , using major radius  $R = 5a$ . The laboratory, simulation and CME event can then all be expressed in terms of the same dimensionless variables.

Figure 5.5 compares the scaled height and time of the leading edge and core, as well as the separation between the leading edge and core, for theory, simulation, experiment, and CME observations. Separation is defined as the center-to-center distance between the main current channel and the reverse current shell. The center of the reverse current shell is at  $\bar{b} + \bar{\delta}/2$ . The theoretical black line is calculated by solving Equation 5.8 with  $\bar{\delta} = 0.25$ ,  $\bar{b}(\bar{t} = 0) = 1$ ,  $\dot{\bar{b}}(\bar{t} = 0) = 0$ , and a sinusoidal ramping current,  $\bar{I} = [\bar{I}_0 + 20 \sin(\pi \bar{t}/60)]$ , where  $\bar{I}_0 \sim 2\pi\sqrt{1 + \beta}$  is set such that the system is initially at equilibrium. This dimensionless current corresponds to an experimental current of 1 kA and a solar current of  $\sim 5 \times 10^{12}$  A. This agreement of normalized parameters in Figure 5.5 indicates that the reverse current mechanism can reproduce the observed three-part structure at the solar scale.

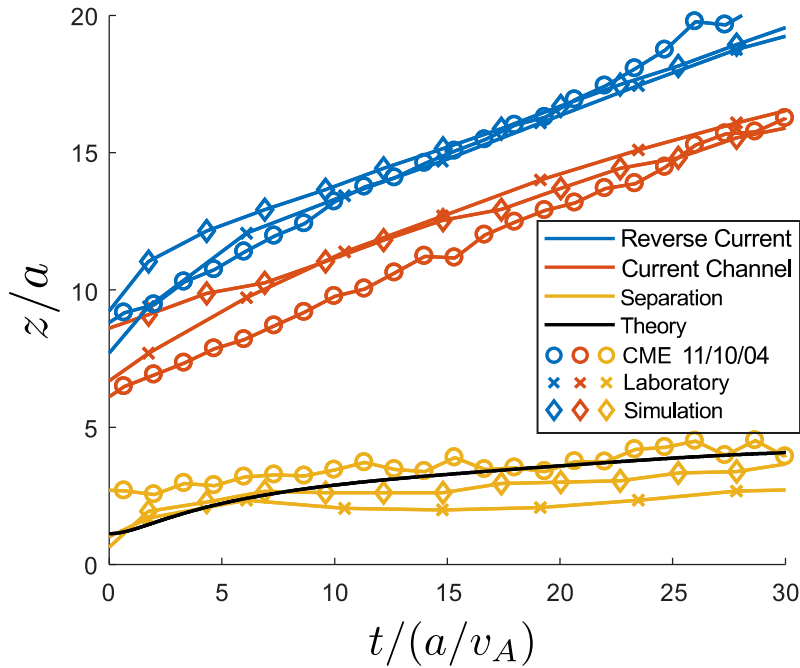


Figure 5.5: Comparison of the cavity width for all the different scenarios, taken from the right column of Figure 5.1. Color: (blue) Reverse current, (red) current channel, (yellow) separation, and (black) theory ( $\bar{b}(t) + \bar{\delta}/2$ ). Style: (o) CME on 2011 October 4, (x) laboratory, and ( $\diamond$ ) simulation. In this plot, the separation is defined as the center-to-center distance between the main current and the reverse current layer. Vertical errorbars are  $\pm 0.5$  for all traces. The black line represents a numerical solution to Eq. 5.8 with  $\bar{\delta} = 0.25$  and  $\bar{I} = [\bar{I}_0 + 20 \sin(\pi \bar{t}/60)]$ .

*Chapter 6***MAGNETICALLY INDUCED CURRENT PISTON FOR  
GENERATING EXTREME-ULTRAVIOLET FRONTS IN THE  
SOLAR CORONA**

Pakorn Wongwaitayakornkul, Magnus A Haw, Hui Li, and Paul M Bellan. “Magnetically Induced Current Piston for Generating Extreme-ultraviolet Fronts in the Solar Corona”. In: *The Astrophysical Journal* 874.2 (2019), p. 137. DOI: <https://doi.org/10.3847/1538-4357/ab09f2>.

P.W. designed and conducted the experiment. P.W. and M.A.H developed the simulation. H.L. provide the simulation source code. P.W., M.A.H., and P.M.B discussed and wrote the manuscript.

In this chapter, we generalize the model from Chapter 5 by letting the plasma mass thickness  $\Delta$  be different from the current layer thickness  $\delta$ . This study emphasizes the relationship between the reverse current layer motion and the properties of the plasma density shock.

Single-pulse, globally-propagating coronal fronts called EUV (or EIT) waves were first observed in 1995 by the Extreme-ultraviolet Imaging Telescope (EIT) and every observed EUV wave since has been associated with a coronal mass ejection (CME). The physical mechanism underlying these waves has been debated for two decades with wave or pseudo-wave theories being advocated. We propose a hybrid model where EUV waves are compressional fronts driven by a reverse electric current layer induced by the time-dependent CME core current. The reverse current layer flows in a direction opposite to the CME core current and is an eddy current layer necessary to maintain magnetic flux conservation above the layer. Repelled by the core current, the reverse current layer accelerates upwards so it acts as a piston that drives a compressional perturbation in the coronal regions above. Given a sufficiently fast piston speed, the compressional perturbation becomes a shock that separates from the piston when the piston slows down. Since the model relates the motion of the EUV front to CME properties, the model provides a bound for the core current of an erupting CME. The model is supported and motivated by detailed results from both laboratory experiments and ideal 3D MHD simulations. Overlaps and differences with other models and spacecraft observations are discussed.

## 6.1 Introduction

Globally-propagating coronal fronts, were first observed in 1995 by the Extreme-ultraviolet Imaging Telescope (EIT) on the Solar and Heliospheric Observatory (SOHO). These ‘wave’-like structures, now called EIT waves or EUV waves, exhibit bright, nearly-circular fronts in the EUV spectrum, with velocities in the range 200-500 km s<sup>-1</sup> [71, 99, 134]. In this work, we will follow the convention of Cohen et al. [30] and describe these features as EUV waves. Spectral observations across a large temperature range (1-4 MK) indicate that these fronts are compressive perturbations [73, 88, 149]. Additionally, there is evidence for adiabatic heating implying modest temperature increases of 5-10% [43, 119, 142, 154]. To date, every observed EUV wave has been associated with a coronal mass ejection (CME) [18, 143, 149]. Since failed eruptions and non-eruptive flares do not produce these fronts, the generation mechanism must be related to the CME expansion. EUV waves are also occasionally coincident with Type II radio bursts indicating the presence of a shock [21].

Reviews of EUV waves [28, 86, 155] have divided the proposed theories into two groups: wave theories and pseudo-wave theories. A pseudo-wave is a phenomenon that behaves similarly to a wave, but is not prescribed by a wave equation. This separation characterizes a fundamental physical difference: waves are self-propagating and pseudo-waves require a driving mechanism. In the wave interpretation, EUV waves are commonly thought to be fast mode Alfvén waves/shocks [135, 146] or some form of slow-mode soliton [153]. The three pseudo-wave theories propose that the bright front is either (i) a current shell [32], (ii) the wake of a Moreton wave [27], or (iii) reconnection at the expanding CME surface [5]. The different theories are categorized in Figure 6.1, based on feature speed and timescale of the driver.

Unfortunately, none of the wave or pseudo-wave theories are consistent with all of the observed properties of EUV waves [86, 153]. A suitable theory must explain why EUV waves (1) are observed as single pulses, (2) propagate at sub-Alfvénic speeds, (3) have coherence across solar diameter scales, and (4) can produce shocks. Due to these varied properties, many papers [29, 30, 34, 83, 106] have called into question the stark separation between the wave and pseudo-wave theories, instead calling for a hybrid model where both pseudo-wave and wave components are present.

The work in this chapter is an extension of the cavity model in Chapter 5 with an emphasis on the piston-driven shock mechanism. We describe in Section 6.2 a simple analytic model for an expanding compressional current layer at the surface of a CME and show that this model is consistent with all the observed properties

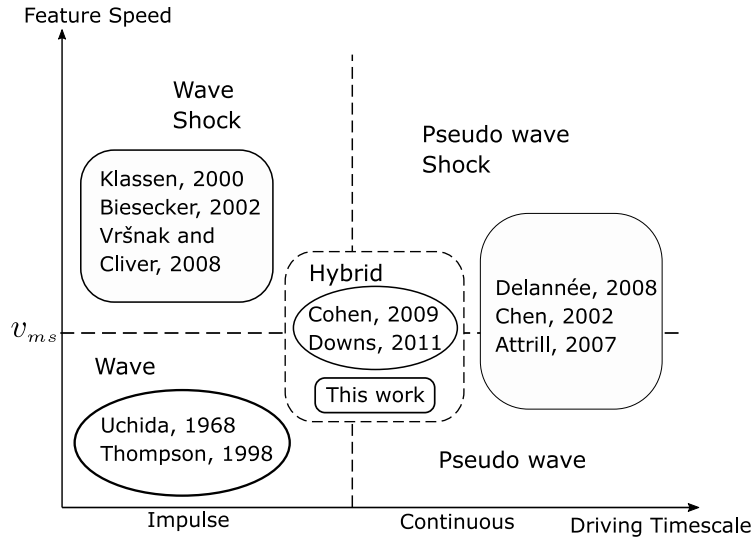


Figure 6.1: Classification of previous literature by feature speed and driving timescale. The trend of the proposed theories goes from wave, to shock, then to pseudo-wave, and finally to hybrid model.  $v_{ms}$  represents the local wave speed.

of EUV waves. This hybrid model quantifies the magnetic driving mechanism, the dynamical evolution of the compressional front, and the generation of fast mode waves/shocks. The model is supported and motivated by an experiment of an erupting flux rope and by a 3D MHD simulation of this experiment, described in Sections 5.2 and 6.4 respectively. The experiment shows a visible  $H_\alpha$  front with associated reverse current layer propagating ahead of the main current channel. The simulation shows the generation of a propagating compressional layer which can be simultaneously classified as a fast mode shock, a current shell, and the expanding surface of the CME. Section 6.5 discusses the degree to which the competing EUV wave theories are physically equivalent.

## 6.2 Theory

### Piston-Driven Shock

A shock is a discontinuity in plasma parameters which occurs when the plasma flow velocity exceeds the characteristic wave speed. In the frame moving with the shock, the plasma conserves mass flux, momentum, magnetic flux, and energy, while entropy increases across the shock. Equating the conserved quantities across the shock yields the Rankine-Hugoniot (R-H) jump conditions. In magnetohydrodynamic (MHD) fluids, information can be carried via three possible waves: (i) shear Alfvén wave, and (ii) fast and (iii) slow branch of magnetosonic wave, which result in three different shock types according to the associated wave. The fast magnetosonic

shock is the only possible type for a configuration with magnetic field perpendicular to the shock normal. In this case, the characteristic velocity of a perpendicular fast magnetosonic wave is  $v_{ms} = \sqrt{c_s^2 + v_A^2}$ , where  $c_s = \sqrt{\gamma P/\rho}$  and  $v_A = B/\sqrt{\mu_0\rho}$  are respectively the local sound and Alfvén speeds. Consider a 1D planar shock and suppose a tangential magnetic field  $B_t$  is perpendicular to the normal flow velocity  $v_n$ ; the following 4 quantities are conserved across the shock so their upstream (u) and downstream (d) values in the shock frame are equal: (i) mass, (ii) flux, (iii) momentum, and (iv) energy. Using  $[Q]_u^d$  to denote the difference of a quantity  $Q$  at upstream and downstream locations, the conservation equations can be written as

$$[\rho v_n]_u^d = 0 \quad (6.1)$$

$$[B_t v_n]_u^d = 0 \quad (6.2)$$

$$\left[ \rho v_n^2 + p + \frac{B_t^2}{2\mu_0} \right]_u^d = 0 \quad (6.3)$$

$$\left[ \frac{1}{2} \rho v_n^3 + \frac{\gamma}{\gamma - 1} p v_n + v_n \frac{B_t^2}{\mu_0} \right]_u^d = 0. \quad (6.4)$$

Solving the system of equations above [37] gives the relations

$$\frac{\rho_d}{\rho_u} = \frac{v_{n,u}}{v_{n,d}} = \frac{B_{t,d}}{B_{t,u}} = X \quad (6.5)$$

$$\frac{p_d}{p_u} = Y = 1 + \gamma \mathcal{M}^2 (1 - X^{-1}) + \beta^{-1} (1 - X^2), \quad (6.6)$$

where  $X$  is the positive root of

$$2(2 - \gamma)X^2 + (2\beta + (\gamma - 1)\beta\mathcal{M}^2 + 2)\gamma X - \gamma(\gamma + 1)\beta\mathcal{M}^2 = 0, \quad (6.7)$$

where  $\mathcal{M} = v_{n,u}/\sqrt{\gamma p_u/\rho_u}$  is the upstream acoustic Mach number, and  $\beta = 2\mu_0 p_u/B_{t,u}^2$  is the ratio of the gas pressure to the magnetic pressure of the unshocked plasma. The expression for compression ratio simplifies to  $X = (\gamma + 1)\mathcal{M}^2/[2 + (\gamma - 1)\mathcal{M}^2]$  for a hydrodynamic shock ( $\beta \gg 1, \mathcal{M}$ ) and  $X = (\gamma + 1)/(\gamma - 1)$  for a strong shock ( $\mathcal{M} \gg 1, \beta$ ).

We can also show that the change of entropy, defined by  $S = \ln(p/\rho^\gamma)$ , can be expressed as  $[S]_u^d = \ln Y - \gamma \ln X$ . The second law of thermodynamics requires  $[S]_u^d > 0$ . Since  $d[S]_u^d/dX \geq 0$  everywhere and  $[S]_u^d = 0$  when  $X = 1$ , it follows that  $X > 1$ , i.e. the shock has to be compressive. Consequently,  $B_{t,d} > B_{t,u}$  always, implying the existence of a current sheet.

The large amplitude wave driven by the piston steepens into a shock due to nonlinear evolution of the wavefront [92, 147]. The large amplitude wave continues to steepen until the width of the discontinuity reduces to either a dissipative or a dispersive length scale. The steepening and dissipative (or dispersive) effects balance out each other and the shock is formed. This implies that the shock will ultimately be formed in every wave with decreasing density in the direction of propagation [78]. The shock can form even when the piston moves below the characteristic wave speed [171], but it might not be observable due to the formation time being larger than the time of observation. When the piston travels at a speed above the characteristic wave speed, the shock is guaranteed to occur. When the piston decelerates, the shock retains its shape and propagation, separating from the piston.

### **Return Current Layers as Magnetic Pistons**

This section outlines a simple analytic model for the generation and expansion of a compressional current layer at the surface of a CME. Consider a stable flux rope in the solar corona and suppose that, through some form of photospheric driving, the net current through this flux rope is increasing. This increasing current will also induce a thin anti-parallel current in the background plasma to shield the increasing azimuthal flux of the rising flux rope (Fig. 6.2). This induced reverse current effectively creates a coaxial current distribution. Reverse currents are generated for all simulation boundary driving mechanisms including flux injection, shearing motion, and rotational motion [24, 32, 87, 137].

Any coaxial current distribution tends to have separation between the forward and reverse currents since anti-parallel currents repel. Consequently, the return current layer will be forced away from the core current, forming a cavity region in between [53]. The expanding reverse current layer effectively serves as a magnetic piston pushing background plasma out in the radial direction (Fig. 6.2). If the expansion velocity of the current layer approaches the magnetosonic speed, the layer can develop a shock front. This mechanism was used in shock tube experiments in the 1960's to study high-Mach number shocks [44, 58] and is sometimes referred to as the inverse-pinch effect.

The inverse-pinch mechanism can be analytically modeled as a vertical ( $\hat{y}$ ) increasing current  $I(t)$  of radius  $a$  in a uniform plasma of density  $\rho_0$ , magnetic field  $B_0\hat{y}$ , and pressure  $P_0$ . This rising current induces an anti-parallel shell current of width  $\delta$ , total current  $-I$ , and a constant current density  $J_y = -I/[\pi(2b + \delta)\delta]$  across its

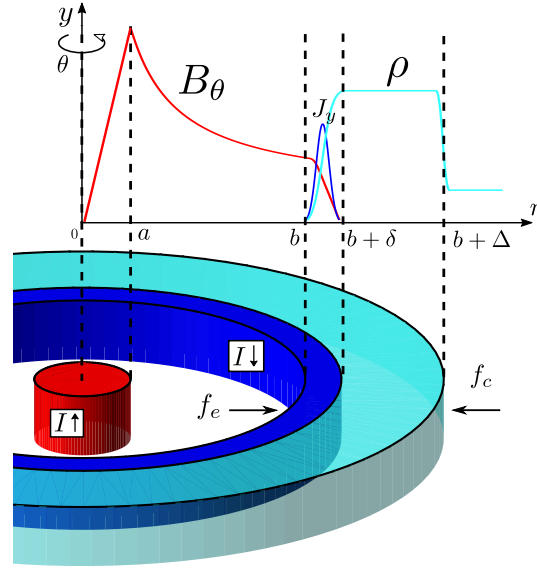


Figure 6.2: Illustration for the analytic model of the current layer generation and propagation. Here, we extend the model so the thickness of current layer  $\delta$  and the thickness of plasma mass  $\Delta$  could be different.

width. The central and return currents correspond to the respective red and dark blue features in Fig. 6.2. The current shell (dark blue) pushes out plasma that is compressed into a density shell (light blue) of thickness  $\Delta$ , bounded by a shock front at  $b + \Delta$ .

The motion of the plasma density shell is controlled by two opposing forces: an expansive magnetic force ( $f_e$ ) which is proportional to the square of the central current  $I$  and a confining force from background pressure ( $f_c$ ). Assuming an axisymmetric expansion of the current layer, we can express the 1D equation of motion in units of force-per-length as

$$\frac{d}{dt} \left( M \frac{d}{dt} b(t) \right) = f_e - f_c, \quad (6.8)$$

where  $M = \rho_0 \pi ((b(t) + \Delta)^2 - a^2)$  is the total mass per-length compressed into the reverse current annulus,  $b(t)$  is the inner radius of the reverse current annulus,  $f_c$  is the confining force-per-length, and  $f_e$  is the expansive force-per-length. The compression of all mass in the swept area into a dense exterior layer is called the “snowplow assumption” (i.e.,  $\delta, \Delta \rightarrow 0$ ) and represents the limiting behavior at high Mach number.

For a more general case comparing to the Chapter 5, we differentiate the thickness of the current layer  $\bar{\delta}$  and the thickness of the plasma mass  $\bar{\Delta}$ . The total expansive force

and confining force can be calculated as shown in Eq. 5.7 giving the normalized integrable equation of motion for the magnetic piston to be

$$\bar{M}\ddot{\bar{b}} = \frac{\bar{I}^2}{3\pi} \frac{3\bar{b} + 2\bar{\delta}}{(2\bar{b} + \bar{\delta})^2} - \pi(\bar{b} + \bar{\Delta})[1 + \beta] - \dot{\bar{M}}\dot{\bar{b}}, \quad (6.9)$$

where normalized values are indicated with a bar i.e.  $\bar{b} = b/a$ ,  $\bar{\delta} = \delta/a$ ,  $\bar{\Delta} = \Delta/a$ ,  $\bar{t} = (B_0/a\sqrt{\mu_0\rho_0})t$ ,  $\bar{I} = I/I_0 = I\mu_0/(B_0a)$ ,  $\bar{M} = M/(\rho_0a^2) = \pi((\bar{b} + \bar{\Delta})^2 - 1)$ , and  $\beta = 2\mu_0P_0/B_0^2$ . This choice of normalization has three free parameters: background magnetic field  $B_0$ , core current radius  $a$ , background plasma density  $\rho_0$ .

In this form, the values of  $\bar{I}$ ,  $\bar{\delta}$ ,  $\bar{\Delta}$ ,  $\beta$ , and  $\gamma$  fully determine the evolution. For  $\bar{\delta}, \bar{\Delta} = 0.2$ ,  $\beta = 136$ , and  $\gamma = 5/3$ , numerical solution of Eq. 6.9 shows that the peak velocity is reached early in the evolution and then quickly decays. For a constant current  $\bar{I}(t) = \bar{I}_c$ , the dynamics of the reverse current layer depends on how  $\bar{I}_c$  compares to two critical values  $\bar{I}_e$  and  $\bar{I}_s$ . When  $\bar{I}_c = \bar{I}_e = \pi(\bar{\delta} + 2)\sqrt{3(\bar{\Delta} + 1)(1 + \beta)/(2\bar{\delta} + 3)} \sim 83$ ,  $\bar{b}(t)$  stays stationary, i.e.  $\ddot{\bar{b}} = 0$  and  $\dot{\bar{b}} = 0$  at  $\bar{b} = 1$ . Below this value, the reverse current layer radially collapses inward due to insufficient internal magnetic pressure to balance out the external one. Above this value, the current piston pushes out the plasma and drives the compressional front. The internal magnetic pressure is initially larger than the external one and decreases as the piston expands. Let the two pressures be equal at  $\bar{b} = \bar{b}_0$ ; at that location,  $\dot{\bar{b}}$  reaches maximum ( $\ddot{\bar{b}} = 0$ ). When  $\bar{I}_c = \bar{I}_s = \pi(2\bar{b}_0 + \bar{\delta})\sqrt{3(\bar{b}_0 + \bar{\Delta})(3 + (\gamma + 1)\beta)/(3\bar{b}_0 + 2\bar{\delta})} \sim 161$ , the maximum speed of piston exceeds the normalized magnetosonic speed,  $v_{ms}/v_A = \sqrt{1 + (c_s/v_A)^2} = \sqrt{1 + \gamma\beta/2}$ , and the piston generates a travelling shock wave, i.e.  $\ddot{\bar{b}} = 0$  and  $\dot{\bar{b}} = \sqrt{1 + \gamma\beta/2}$  at  $\bar{b} = \bar{b}_0$ .  $\dot{\bar{M}} = 2\pi(\bar{b} + \bar{\Delta})\dot{\bar{b}}$  is used for the third term of the right hand side of Eq. 6.9. Numerical solution shows that  $\bar{b}_0 \sim 1.3$  for  $100 < \bar{I}_c < 200$ . Given the expression for the total mass of the density shell, the compression ratio can be expressed as  $X = \bar{\rho} = ((\bar{b} + \bar{\Delta})^2 - 1)/((\bar{b} + \bar{\Delta})^2 - \bar{b}^2)$ .

This hybrid model exhibits both wave and pseudo-wave characteristics. Since the feature motion is determined by physical forces rather than by a dispersion relation, the layer will move at a range of possible speeds depending on the driving current and the local background conditions. The model also generates shocks for initial conditions (namely  $\bar{I}_c > \bar{I}_s$ ) where the driving velocity exceeds the magnetosonic speed at early times. Thus, if  $\bar{I}_e < \bar{I}_c < \bar{I}_s$  the phenomenon will be wave-like and sub-Alfvénic whereas if  $\bar{I}_c > \bar{I}_s$  the phenomenon will be shock-like and super-Alfvénic. This range of possible behaviors from low speed (sub-Alfvénic) to high speed (shock)

satisfies the major observational constraint that sometimes sub-Alfvénic wave-like behavior is observed and sometimes, as manifested by Type II radio bursts, fast shock-like behavior is observed.

The theory in the previous section is motivated by measurements of a plasma flux rope experiment. This experiment was designed to produce an arched flux rope with dimensionless parameters similar to those of solar prominences ( $\mu_0 L v_A / \eta \gg 1$ ,  $\beta \sim 0.1$  inside the loop and  $\beta \sim 100$  in the background) [46, 125, 157]. This dimensionless equivalence allows solar prominences to be simulated in the lab with high repetition and control. A description of free parameters and constraints on dimensionless scaling in MHD is given in Ryutov, Drake, and Remington [116]; this shows that the experiment can be readily scaled to solar situations.

The experiment combines three subsystems to generate flux ropes: solenoids to provide a background bipolar magnetic field, gas ports to supply neutral argon gas, and electrodes which drive current through the plasma (Fig. 5.2a). The resulting arched flux rope then expands outwards due to the hoop force. For a more detailed description of the experimental apparatus see Ha and Bellan [46], Stenson and Bellan [125], and Wongwaitayakornkul et al. [157].

The experiments described in this chapter use an additional hydrogen background prefill ( $n \sim 10^{21} \text{ m}^{-3}$ ) not present in previous experiments [46, 125, 157]. This background gas serves two purposes: it creates a background hydrogen plasma for the flux rope to interact with and it enables distinguishing the motion of the flux rope (Ar) and background plasma (H) from each other through spectroscopic filtering of images. This technique is exhibited in the left halves of the image sequence shown in Figure 6.3. This sequence shows the formation and propagation of a density front in the background hydrogen plasma. This layer (cyan) propagates ahead of the flux rope (red) with an increasing separation over time.

A fast ICCD movie camera, a magnetic probe array and Langmuir probes are used to diagnose spatial and temporal characteristics of the plasma. The optically filtered fast ICCD camera provides the series of spectroscopic images shown in the left half of Figure 6.3. The magnetic probe array measures the magnetic field along the  $z$  axis from voltages induced by changing magnetic fields. Assuming that the internal evolution is much slower than the global expansion, the time evolution can be converted [53] to spatial position with  $\partial/\partial z \leftrightarrow v_z^{-1} \partial/\partial t$ , with  $v_z = 15 \text{ km s}^{-1}$ . Then  $J_y = (\nabla \times \mathbf{B}) \cdot \hat{y} / \mu_0 = (\partial_z B_x - \partial_x B_z) / \mu_0 \approx (\partial_t B_x) / (\mu_0 v_z)$ , since spatial variation of the flux rope is mostly in  $z$  direction ( $\partial_z B_x \gg \partial_x B_z$ ). Negatively biased

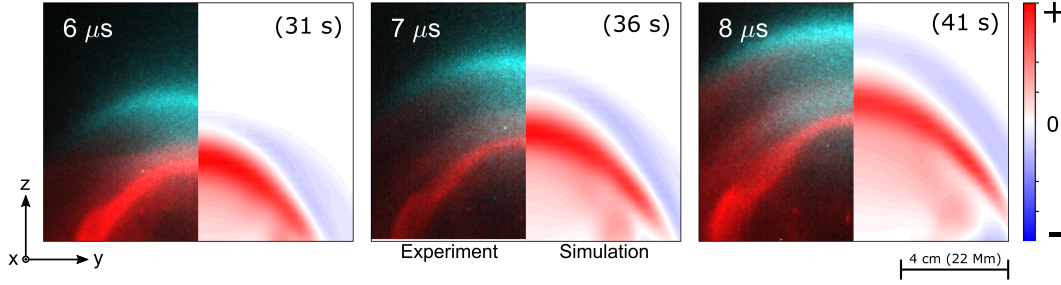


Figure 6.3: The left dark background halves are the image sequence of multiwavelength fast camera images of the experiment, composing of two band passes: visible (red) and filtered  $H_{\alpha}$  (cyan). The right white background halves are the cross-sectional plots of simulated current density in horizontal direction ( $J_y$ ) of the ideal 3D MHD simulation. The colorbar indicates the value of  $J_y$ . In both cases, the snapshots are taken at the same time (labelled in white) after the plasma breakdown. The simulated images are taken at different times from Haw et al. [53]. The temporal and spatial quantities are scaled into solar environment as labelled in the parentheses

Langmuir probes measured ion saturation current from the plasma at a given time along the  $z$  axis. The ion density can be inferred from ion saturation current  $I_{\text{sat}}$ , with an isothermal assumption, i.e.,  $n_i = I_{\text{sat}} / (0.6eAc_s)$  with  $c_s = \sqrt{2\kappa T_e / m_i} = 20 \text{ km s}^{-1}$  and probe tip area  $A = 7.6 \times 10^{-6} \text{ m}^2$ .

The solid lines in Figs. 6.4a and 6.4c are example plots of the measured time dependence of probes at three different values of  $\bar{z}$ . This data was fitted with analytic functions which are plotted as dashed lines in Figs 6.4a and 6.4c.  $\bar{J}_y(\bar{t})$  was modeled as two Gaussian peaks and  $\bar{\rho}(\bar{t})$  was modeled as a piecewise function that increases linearly and decreases exponentially. The Langmuir probe data was taken from 164 shots at 24 different locations ( $\bar{z} = 10\text{--}30$ ). The magnetic data was taken from 83 shots at 4 different locations ( $\bar{z} = 16\text{--}22$ ). Space-time contour plots of  $\bar{J}_y(\bar{z}, \bar{t})$  and  $\bar{\rho}(\bar{z}, \bar{t})$  were constructed from the measurements and are shown in Figs. 6.4b and 6.4d. The positive and negative component of  $\bar{J}_y$  contour are scaled differently to enhance the negative component. A detailed description of the method for construction of these contour plots is given in Section 6.3. These measurements along with the lower brightness of optical line emission in between the two opposite current features from the images imply that there is a depletion in density in the region between the two opposite currents. The Langmuir probe signals show a clear jump in density indicating a shock in ion density with thickness  $\delta = 0.8 \pm 0.3 \text{ cm}$  and compression ratio  $X = 1.8 \pm 0.4$ . Let  $t_0$  and  $t_1$  be the time in which Langmuir probe data first increase from the background level and reach the peak respectively.

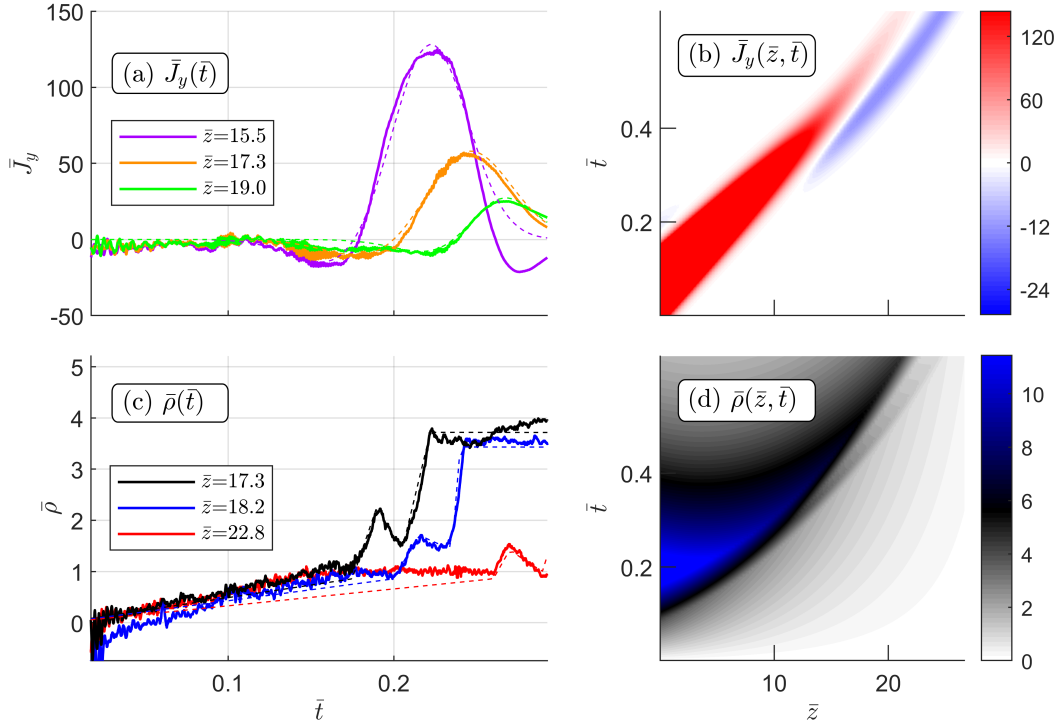


Figure 6.4: (a) and (c) show the experimental sample time series of the magnetic and Langmuir probes (solid line) with the reconstructed fitted profiles (dashed line). (b) and (d) plot the space-time profiles of the dashed line of  $\bar{J}_y$  and  $\bar{\rho}$  in (a) and (c). The normalized parameters for the experiment are  $a = 1.1$  cm,  $v_A = 0.43$  km s<sup>-1</sup>,  $\tau = a/v_A = 130$   $\mu$ s,  $\rho_0 = 9.1 \times 10^{-9}$  kg m<sup>-3</sup>,  $B_0 = 0.46$  G and  $J_0 = \sqrt{\rho_0/\mu_0}/\tau = 3.3$  kA m<sup>-2</sup>. These parameters can be scaled to the solar context using  $a = 6.25$  Mm,  $v_A = 41.7$  km s<sup>-1</sup>,  $\tau = 135$  s,  $\rho_0 = 7.0 \times 10^{-12}$  kg m<sup>-3</sup>,  $B_0 = 1.2$  G, and  $J_0 = 16.7$   $\mu$ A m<sup>-2</sup>. The method for scaling to the solar context is given in Chapter 5.

Then  $\delta$  is deduced from the difference in the arrival times and from the speed of the feature as  $\delta = v_z(t_1 - t_0)$ .  $X$  is determined by the ratio of the signal at those two times,  $X = \bar{\rho}(t_1)/\bar{\rho}(t_0)$ .

The following section describes results from a 3D ideal MHD numerical simulation of the experiment. This numerical simulation confirms that the reverse current mechanism can generate shocks and also allows a shock analysis with high spatial resolution.

### 6.3 Experimental Contour Reconstruction

The following steps are used to create the space-time contour plots shown in Figs. 6.4b and 6.4d:

1. A single point measurement at location  $\bar{z} = z_j^*$  and  $z_\rho^*$  gives experimental time series  $\bar{J}_{y,\text{exp}}(\bar{t})$  and  $\bar{\rho}_{\text{exp}}(\bar{t})$  respectively.
2. A constructed time series profile for both parameters are defined as two Gaussian peaks for  $\bar{J}_{y,\text{con}}(\bar{t})$  and a piecewise function that increases linearly and decreases exponentially for  $\bar{\rho}_{\text{con}}(\bar{t})$ . The analytic expressions are given by Eqs. 6.10 and 6.11.

$$\bar{J}_{y,\text{con}}(\bar{t}; J_\pm, t_\pm, \tau_\pm) = J_+ \exp\left(-\frac{(\bar{t} - t_+)^2}{2\tau_+^2}\right) - J_- \exp\left(-\frac{(\bar{t} - t_-)^2}{2\tau_-^2}\right), \quad (6.10)$$

$$\bar{\rho}_{\text{con}}(\bar{t}; \rho_i, t_i, \lambda)_{i=0,1,2,3} = \begin{cases} (\rho_0/t_0)\bar{t} & , \bar{t} < t_0 \\ (\rho_1 - \rho_0)(\bar{t} - t_0)/(t_1 - t_0) + \rho_0 & , t_0 < \bar{t} < t_1 \\ \rho_1(\rho_2/\rho_1)^{(\bar{t}-t_1)/(t_2-t_1)} & , t_1 < \bar{t} < t_2 \\ (\rho_3 - \rho_2)(\bar{t} - t_2)/(t_3 - t_2) + \rho_2 & , t_2 < \bar{t} < t_3 \\ \rho_3 \exp(-(\bar{t} - t_3)/\lambda) & , \bar{t} > t_3. \end{cases} \quad (6.11)$$

3. For a given pair of  $(z_j^*, z_\rho^*)$ , the comparison between the experimental and constructed profile gives fitting parameters for this particular pair of  $\bar{z}$ .

$$\left\{ \begin{array}{l} \bar{J}_{y,\text{exp}}(\bar{t}) \leftrightarrow \bar{J}_{y,\text{con}}(\bar{t}; J_\pm, t_\pm, \tau_\pm) \\ \bar{\rho}_{\text{exp}}(\bar{t}) \leftrightarrow \bar{\rho}_{\text{con}}(\bar{t}; \rho_i, t_i, \lambda) \end{array} \right\} \xrightarrow{\text{extract}} \left\{ \begin{array}{l} J_\pm, t_\pm, \tau_\pm \\ \rho_i, t_i, \lambda \end{array} \right\} \quad , \text{ at } \bar{z} = z_j^* \text{ or } z_\rho^*. \quad (6.12)$$

4. The pair  $(z_j^*, z_\rho^*)$  is varied through its domain to determine the  $\bar{z}$  dependency of each parameter. The  $C_j$ 's are determined by best fit to the measured data. The models are chosen as follows:

- a)  $J_\pm$  is modeled as an exponential decay, i.e.  $J_\pm(\bar{z}) = C_1 \exp(-C_2\bar{z})$ . The current is assumed to decay exponentially due to the magnetic diffusion. The extrapolation of  $\bar{J}_y(\bar{z})$  to small  $\bar{z}$  is consistent with the expected value, i.e.  $J_{y,\text{expected}} = 1 \text{ kA}/(\pi(0.5 \text{ cm})^2) \sim 40 \text{ MA m}^{-2} \rightarrow \bar{J}_{y,\text{expected}} \sim 8 \times 10^3$ .
- b)  $\rho_i$  and  $t_i$  for  $i = 0, 1, 2, 3$  are fitted as second degree polynomials with respect to  $\bar{z}$ , for example,  $t_0(\bar{z}) = C_3\bar{z}^2 + C_4\bar{z} + C_5$ . The Langmuir probe data covers most of the range of  $\bar{z}$ . Therefore, we choose the simplest

smooth curve function to fit these parameters.  $t_{\pm}$  lie well with the best fit of  $t_1$  and  $t_3$  within their domain, so we set  $t_{-}(\bar{z}) = t_1(\bar{z})$  and  $t_{+}(\bar{z}) = t_3(\bar{z})$ .

- c)  $\tau_{\pm}$  and  $\lambda$  are chosen to be constants, i.e.  $\tau_{\pm}(\bar{z}) = 0.01$  and  $\lambda(\bar{z}) = 0.1$ . From observations, the widths do not change with  $\bar{z}$  as much as the other parameters. Thus, for simplicity, the widths are assumed to be constant for all  $\bar{z}$ .

5. Figures 6.4b and 6.4d are obtained by plotting contours in the space-time domain using the constructed functions.

$$\bar{J}_y(\bar{z}, \bar{t}) = \bar{J}_{y,\text{con}}(\bar{t}; J_{\pm}(\bar{z}), t_{\pm}(\bar{z}), \tau_{\pm}(\bar{z})), \quad (6.13)$$

$$\bar{\rho}(\bar{z}, \bar{t}) = \bar{\rho}_{\text{con}}(\bar{t}; \rho_i(\bar{z}), t_i(\bar{z}), \lambda(\bar{z})). \quad (6.14)$$

#### 6.4 MHD Numerical Simulation

The 3D ideal MHD simulation of the experiment was performed on the Los Alamos Turquoise cluster as part of the Los Alamos COMPUTational Astrophysical Simulation Suite (LA-COMPASS) to reproduce the Caltech solar loop experiment [53, 80, 167]. The simulation follows the evolution of 8 parameters: mass density  $\rho$ , pressure  $p$ , velocity  $\mathbf{v}$ , and magnetic field  $\mathbf{B}$  inside a numerical Cartesian box of size  $32a$ . The initial parameters are set to emulate the experimental setup shown in Fig 5.2a. The initial density consists of two conic-shape density profiles as produced by the gas nozzles at the footpoints when there is a substantial pre-filled uniform background density. The initial magnetic field is the bipolar potential field from the two solenoids behind the electrodes. The pressure is calculated from the isothermal assumption and the plasma is initially at rest. Electric current is injected into the system by adding azimuthal magnetic field corresponding to a group of circular current loops [53, 124, 157] with a sinusoidal time dependence that mimics that in the experiment. Figure 6.3 shows the time dependence of the loop expansion as observed in the experiment (left halves of figures) and as calculated in the simulation (right halves of the figures). The simulation is in reasonable agreement with the laboratory plasma in terms of the loop's evolution and magnetic field. The full diagnostic capability of the simulation allows for more detailed analysis than possible in the experiment of the temporal and spatial dependence of the main current channel (red) and the reverse current layer (blue).

The evolution of the system can be broken down into three stages: formation, driving, and decoupling. Figure 6.5 shows the evolution of the apex, defined as the

$z$  coordinate of local maxima of  $|J_y|$ . Let  $\bar{t} = v_A t/a$  and  $\bar{z} = z/a$ , where  $a$  is the minor radius of the flux rope and the nominal length for normalization and  $v_A$  is the Alfvén speed. In the formation stage ( $\bar{t} < 0.22$ ), a current flowing in the positive  $y$  direction is injected into the system. The curved current channel expands in major radius due to its hoop force and compresses in the positive  $z$  direction, forming a flattened current channel flowing mainly in the positive  $y$  direction. Later in the driving stage ( $0.22 < \bar{t} < 0.40$ ), a reverse current layer is formed above the original expanding current channel; this reverse current is formed to satisfy the magnetic flux conservation condition in the stationary conducting background plasma above the current channel. The increased azimuthal magnetic field in between the main and reverse currents pushes the reverse current layer out radially and leaves behind a region of depleted density (region between red and blue regions in Fig. 5.2a and in Fig. 6.3). The plasma boundary, or contact front (bottom of blue region in Fig. 6.3), acts as a magnetic piston, compressing the swept-out plasma. With sufficiently strong current, the piston expands faster than the magnetosonic speed in the plasma. As a result, a shock is formed ahead of the piston and all the mass swept up by the shock is compressed into a thin layer immediately behind the shock. The current layer and the shock are indistinguishable at this stage. The thin current layer is repelled by the core current and quickly reaches the equilibrium standoff distance as prescribed by Eq. 6.9. The full dynamics of the induced current sheet is governed by the force balance of  $f_e$  and  $f_c$ , described in Section 6.2. At  $\bar{t} \sim 0.40$ , the current injection stops, causing the driver and the contact front to decelerate. With the condition described in Section 6.2, the contact front and the shock separate. The shock remains in motion, while the contact front decelerates with the driver. Thus for  $\bar{t} > 0.40$  the shock is decoupled from the piston and propagates freely.

The analytic theory presented in Section 6.2 used the cylindrical coordinate system shown in Fig. 6.2. In this section we present a result of a numerical simulation where Cartesian coordinates are used instead. The correspondence follows  $\{r \rightarrow z, y \rightarrow y, \theta \rightarrow x\}$ . Since the apex moves in the  $z$  direction, it is convenient to plot the parameters along the  $z$  axis. Figure 6.6a plots contours of  $\bar{J}_y$  as a function of  $\bar{z}$  and  $\bar{t}$ . Recall that  $\bar{J}_y$  is the horizontal component of the current at the apex as shown in Fig. 5.2a. Figure 6.6a shows the main current channel in red and the reverse current in blue slightly to the right of the red. The experimental  $\bar{J}_y$  contour in Fig. 6.4b shows a larger decay of amplitude in  $\bar{z}$  compared to its simulated counterpart in Fig. 6.6a. This is expected due to a higher resistivity in the experiment. The slope,  $d\bar{t}/d\bar{z}$ , of the reverse current layer in Fig. 6.6a implies a propagation speed

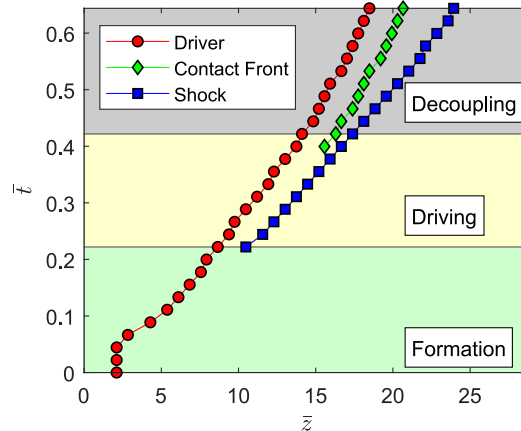


Figure 6.5: Evolution of apex locations of the simulation during the three stages

$\bar{v}_s = d\bar{z}/d\bar{t} = 25$ , which exceeds the local fast magnetosonic speed  $\bar{v}_{ms} = 10$  of the unshocked plasma.

The transition is therefore a fast mode shock and should obey the R-H relations given in Section 6.2. Figure 6.6b plots the temperature  $\bar{T}$ , showing that the loop becomes cooler as its size increases. This is expected from the adiabatic equation of state. The main current channel, however, remains the hottest part even after the shock forms. The density  $\bar{\rho}$ , in Figure 6.6c, shows that the density amplification is largest at the location of the shock front. Behind the shock, the density depletes to a value lower than the background (black region). Contrary to the experiment (Fig. 6.4c), the simulated density contour (Fig. 6.6c) appears to contain a single peak at most times. A two peaks profile can only be observed when the shock is initially formed, i.e.  $\bar{t} \sim 0.56$ . The density peak of the main current decays abruptly, while the density peak of the shock remains more or less constant. As the system expands, the volume increases. However, only the shock acquires the additional material from the background plasma. In the experiment, the plasma behind the electrode most likely supplies material to sustain the density of the main current loop. Lastly, the velocity plot, shown in Figure 6.6d, exhibits the initially fast expanding loop due to the strong flow of material behind the loop. At  $\bar{t} < 0.38$ , the plasma behind the loop experiences a large magnetic force in the positive  $z$  direction from the current injection indicated by its large  $v_z$ . For  $\bar{t} > 0.44$ , the shock front and its plasma flow reach constant terminal speeds.

Figure 6.7 displays the set of quantities, in the frame moving with the shock of speed  $\bar{v}_s$ , on the shock boundaries at time  $\bar{t} = 0.56$  from the simulation; this time is

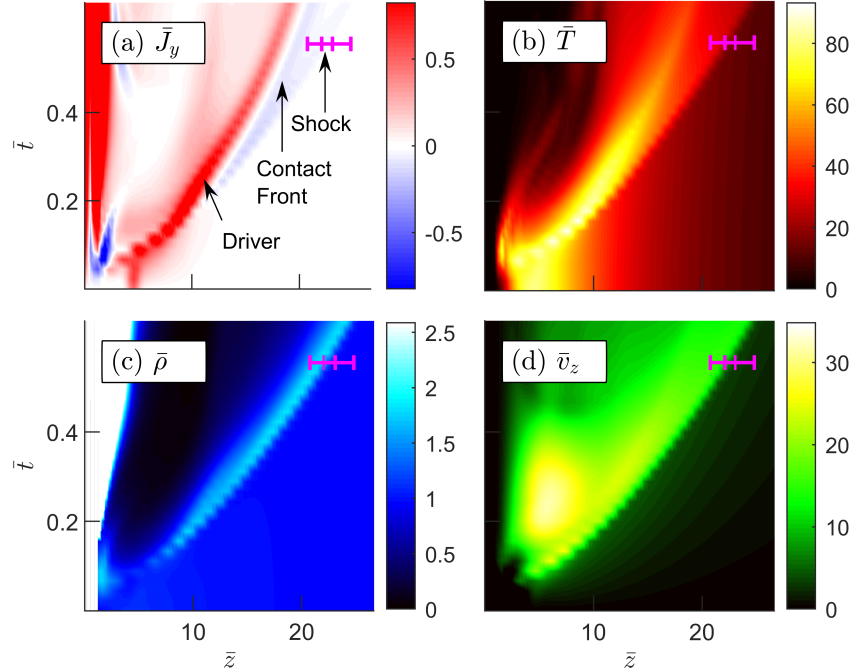


Figure 6.6: Time evolution of 4 quantities from the MHD simulation in  $z$  along the apex. The plots consist of (a) current density, (b) temperature, (c) mass density, and (d) flow speed. For coronal environment, the normalization quantities are  $a = 6.25 \text{ Mm} \sim 0.01 R_{\odot}$ ,  $v_A = 41.7 \text{ km s}^{-1}$ ,  $\tau = a/v_A = 135 \text{ s}$ ,  $\rho_0 = 7.0 \times 10^{-12} \text{ kg m}^{-3}$ ,  $B_0 = 1.2 \text{ G}$ ,  $J_0 = \sqrt{\rho_0/\mu_0}/\tau = 16.7 \text{ } \mu\text{A m}^{-2}$ , and  $T_0 = m_H v_A^2/2k = 9.7 \times 10^4 \text{ K}$  ( $m_H = 1 \text{ u}$ ).

denoted as “shock” in Fig. 6.6.  $\bar{\rho}$  is the plasma density,  $\bar{p}$  is the gas pressure,  $\bar{v}_z$  is the velocity in  $z$  direction, and  $\bar{B}_t$  is the tangential magnetic field in the  $xy$ -plane. The flow speed in the shock frame is defined as  $\bar{v}'_z = \bar{v}_z - \bar{v}_s$ . This relation is obtained by (i) move to shock frame  $\bar{v}_z \rightarrow \bar{v}_z - \bar{v}_s$  and (ii) flip the sign  $\bar{v}_z - \bar{v}_s \rightarrow \bar{v}_s - \bar{v}_z$  to have  $\bar{v}'_z$  be positive in  $-\hat{z}$  direction. The subscripts  $u$  and  $d$  represent the upstream and downstream value of the parameters, which are taken from the boundary of the shocks denoted by the vertical dashed lines in Fig. 6.7. Given that the fast magnetosonic speed is always greater than the Alfvén speed  $v_{ms} = \sqrt{v_A^2 + c_s^2} > v_A$ , the background colors specify three regions in velocity phase space based on  $v'_z$ : (i)  $v'_z > v_{ms}$ , (ii)  $v_{ms} > v'_z > v_A$ , and (iii)  $v'_z < v_A$ . The shock takes the plasma flow from region (i) to (ii), which is the characteristic of the fast magnetosonic type.

Given the characteristic of the background plasma  $\mathcal{M}$  and  $\beta$ , we may now calculate the expected compression ratios  $X$  and  $Y$  using Eqs. 6.5-6.6. For the simulation at the time  $\bar{t} = 0.56$ , the compression ratios can be determined from the upstream parameters  $\bar{\rho}_u = 1$ ,  $\bar{v}'_{z,u} = 1$ ,  $\bar{B}_{t,u} = 1$ ,  $\bar{p}_u = 1$ , which gives  $\mathcal{M} = 1.8$ ,  $\beta = 136$ .

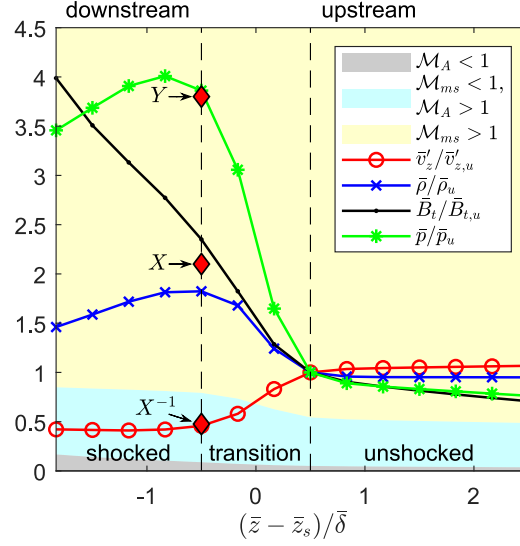


Figure 6.7: The plot tracks the transition of 4 variables in the MHD simulation: flow velocity in shock frame  $\bar{v}'_z = \bar{v}_s - \bar{v}_z$ , mass density  $\bar{\rho}$ , pressure  $\bar{p}$ , and tangential magnetic field  $\bar{B}_t$  across the shock. The  $\bar{z}$  range and time for this plot are shown as the magenta line in Fig. 6.6. The background colors represent the three regions in velocity phase space: (i)  $v'_z > v_{ms}$ , (ii)  $v_{ms} > v'_z > v_A$ , and (iii)  $v'_z < v_A$ . The two vertical dash lines indicate the boundaries of the shock. Each parameter is normalized to their upstream value. The expected compression ratios are labelled as  $Y$ ,  $X$ , and  $X^{-1}$  on the downstream boundary.  $\bar{z}_s$  is the location of shock center and  $\bar{\delta}$  is the shock thickness.

Using these values in Eqs. 6.5 and 6.6 gives  $X = 2.1$  and  $Y = 3.8$  as indicated with diamond markers in Figure 6.7. The simulated compression ratios are  $\bar{\rho}_d/\bar{\rho}_u = 1.8$ ,  $\bar{v}'_{z,u}/\bar{v}'_{z,d} = 2.1$ ,  $\bar{B}_{t,d}/\bar{B}_{t,u} = 1.9$ , and  $\bar{p}_d/\bar{p}_u = 3.9$ , where up and downstream values are measured at the locations of the vertical dashed lines. These compression ratios are also consistent with the analytic expression in Section 6.2. The simulated compression ratios match well with the analytic expression for  $X = \bar{\rho}_d/\bar{\rho}_u$  and  $Y = \bar{p}_d/\bar{p}_u$ , indicating that the perturbation front is a fast magnetosonic shock. For  $\mathcal{M} = 1.8$ ,  $\beta = 136$ , and  $\gamma = 5/3$ , the magnetosonic mach number  $\mathcal{M}_{ms} = \mathcal{M}/\sqrt{1 + 2/\gamma\beta} > 1$ . The normalized entropy,  $\bar{S} = \ln(\bar{p}/\bar{\rho}^\gamma)$ , also increases across the shock ( $\Delta\bar{S} = 0.4$ ).

The simulation shows that a flux rope erupted from the injection of the electrical current induces a layer of reverse current that acts as a magnetic piston. Impulsive expansion of the piston produces a fast mode shock that is also a current layer due to the compression of the background magnetic field. The dynamics of the piston is described in Section 6.2 and is compared to the simulation in Haw et al. [53]. In

the driving phase, the shock and piston are attached. Thus, the shock evolution is governed by the movement of the driver, displaying the characteristic of a pseudo-wave. In the decoupling stage, the shock detaches from the piston because the piston decelerates to a speed below the local fast magnetosonic wave speed. The piston and shock separate and so the shock escapes the driving influence of the piston. The shock is then self-propagating, representing the wave behavior. The presence of both wave and pseudo-wave behavior of the simulated shock supports the hybrid theory of CME-driven EUV wave.

## 6.5 Discussion

Despite the variety of different models to explain EUV waves, the physical manifestation of all proposed models is a propagating, compressive current layer. This current layer is caused by compression of the background magnetic field but in previous models this current has not been identified as being in the reverse direction with respect to the current in the erupting flux rope. Fast mode pulses/shocks are, by definition, compressive current layers. The current layer model in Delannée et al. [32] has been previously characterized purely in terms of the electric current; however, it is also co-spatial with a compressive density pulse. The wake model in Chen et al. [27] identifies the EUV wave as a compressive front but does not take into account that a compressional front must necessarily contain electric current. Finally, the successive magnetic reconnection model in Attrill et al. [5] creates an expanding density enhancement with electric current. This is not implying that all the models are equivalent but highlights the overlap instead of the differences. In some cases, such as the current layer [32] and wake models [27], it is not clear if there is a physical distinction between these two models [86]. Table 1 in Long et al. [86] presented predictions of pulse physical properties from six previous theories and Table 2 of Long et al. [86] showed how these predictions compare to observations. Table 6.1 presented here shows the predictions given by the model presented in this chapter for the properties listed in Long et al. [86].  $v_{\text{CME}_\perp}$  and  $a_{\text{CME}_\perp}$  represents the lateral velocity and acceleration of the erupting CME.  $A_{\text{CME}}$  represent the area bounded by the CME bubble. These predictions are similar to the previous fast mode wave/shock and current shell theory, which are in good agreement with observations. The physical manifestation of the pulse would then be dictated by whether the time of observation is in the driving or decoupling phase of the event.

The hybrid model proposed here is consistent with existing observations. The main observation supporting the fast mode shock model is the strong correlation between

Pulse properties	This Hybrid Model		
	Driving Phase	Decoupling Phase	
		Small amp. linear wave	Large amp. wave/shock
Phase velocity [ $v$ ]	$\gtrsim v_{\text{CME}\perp}$	$v_{ms}$ $> v_{\text{CME}\perp}$	$> v_{ms}$ $> v_{\text{CME}\perp}$
Acceleration [ $a$ ]	$\gtrsim a_{\text{CME}\perp}$	0	$< 0$
Broadening	$f(a_{\text{CME}\perp})$	$\approx 0$	$> 0$
$\Delta B$	$> 0$	$> 0$	$> 0$
$\Delta T$	Adia.+ $Q_{\text{Joule}}$	Adia.	Adia.+ $Q$
$\Delta n_e$	Compression	Compression	Compression
Height	$f(\text{CME bubble})$	$f(B, n_e)$	$f(B, n_e)$
Area bounded	$A_{\text{CME}}$	$> A_{\text{CME}}$	$> A_{\text{CME}}$
Rotation	Possible	Possible	Possible
Reflection	No	Yes	Yes
Refraction	No	Yes	Yes
Transmission	No	Yes	Yes
Stationary fronts	Yes	Yes	Yes
Co-spatial Type II	No	No	Possible
Moreton wave	No	No	Possible

Table 6.1: Prediction from this model for properties listed in Long et al. [86].

the type II radio burst and the EUV waves [18, 71, 146]. Assuming the density profile of the corona, one could deduce the speed of the emitter from the radio signals, which turns out to be faster than the coronal Alfvénic speed, suggesting that the emitter is a coronal shock front. In addition, CMEs are strongly correlated with the observation of EUV waves [18, 143, 149]. Figure 6.8 shows a system of flux rope and shock for both an AIA observation on Jun 13, 2010 and our laboratory experiment in reverse grayscale (i.e., black is maximum value and white is minimum value). We have shown that an erupting flux rope can generate a fast magnetosonic shock. The fast magnetosonic shock generated by an erupting CME should then be able to produce the type II radio burst.

Previously measured compression ratios of the observed global EUV wave, deduced from the intensity ratios of line emission, are 1.05–1.30 [85, 100, 170]. In the numerical MHD simulation shown in Figs. 6.5 – 6.7, we obtain the compression ratio of  $X = 1.9$ , which is different from the observed values due to different  $\mathcal{M}$  and  $\beta$  of each events; Eq. 6.7 shows the relation between  $X$ ,  $\mathcal{M}$ , and  $\beta$ . For example, substituting  $\mathcal{M} = 4.36$  (Note that  $\mathcal{M} = \mathcal{M}_{ms}\sqrt{1 + 2/\gamma\beta}$ ) and  $\beta = 0.1$  into Eq. 6.7 gives  $X = 1.27$  as presented for May 19<sup>th</sup>, 2007 event in Muhr et al. [100]. While a uniform  $\beta = 0.1$  is commonly used at  $z \sim 70\text{--}200$  Mm ( $0.1R_{\odot} - 0.2R_{\odot}$  [85, 88]) above the solar surface as suggested by Gary [40], a more recent simulation [19] proposed that a varying  $\beta = 20 - 200$  is more suitable in that region. This range

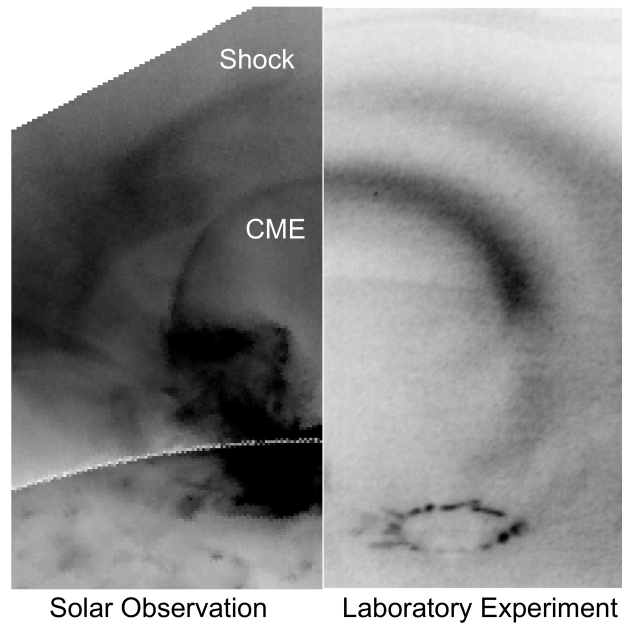


Figure 6.8: Comparison of (left) the low coronal EUV ( $193 \text{ \AA}$ ) shock wave observed with AIA/SDO on 2010 June 13 (adapted from Ma et al. [88]) and (right) visible emission from the Caltech experiment in reverse grayscale.

of  $\beta$  is used in our simulation. If we were to use  $\mathcal{M} = 1.19$  and  $\beta = 136$ , the corresponding  $X$  according to Eq. 6.7 would also be  $X = 1.27$ . Figure 6.9 shows the contour of compression ratio  $X$  in  $(\mathcal{M}, \beta)$ -space.  $X = 1.27$  is drawn with a solid line. The two points  $(\mathcal{M} = 4.36, \beta = 0.1)$  and  $(\mathcal{M} = 1.19, \beta = 136)$  both correspond to  $X=1.27$  and are plotted with green and blue markers respectively. For  $\beta \gg 10$ ,  $X$  is no longer sensitive to  $\beta$  and the shock approaches the hydrodynamic limit. While  $\beta$  and  $v_{ms}$  are the properties of the background plasma, the expanding speed of the structure depends on the internal current of the CME's core as discussed in Section 6.2. Consequently, the observation of the global EUV waves and their measured compression ratios could give us insight into the eruption mechanism of the CME.

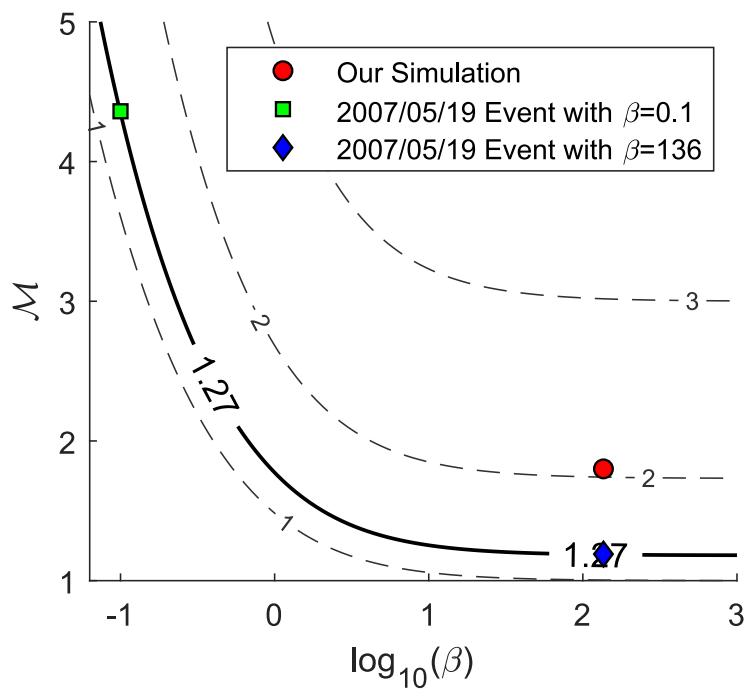


Figure 6.9: Contour of the compression ratio  $X(\mathcal{M}, \beta)$  as determined by Eq. 6.7. The compression ratio of the May 19<sup>th</sup>, 2007 event in Muhr et al. [100]  $X = 1.27$  is plotted as a solid line. The two points corresponding to  $\beta = 0.1$  and 136 along  $X = 1.27$  are plotted with green and blue markers. The value used in the simulation of this work is plotted with a red marker.

## Chapter 7

### MAGNETIC RAYLEIGH-TAYLOR INSTABILITY IN AN EXPERIMENT SIMULATING A SOLAR LOOP

Yang Zhang, Pakorn Wongwaitayakornkul, and Paul M Bellan. “Magnetic Rayleigh-Taylor Instability in an Experiment Simulating a Solar Loop”. In: *The Astrophysical Journal Letters* 889.2 (2020), p. L32. doi: <https://doi.org/10.3847/2041-8213/ab6b2d>.

P.W. and Y.Z. conducted the initial stage of the experiment, obtaining the MRTI. Y.Z. conducted a further characterization showing that the observed MRTI wavelength is consistent with theory. P.W. participated in the discussion. Y.Z. and P.M.B. discussed and wrote the manuscript.

Chapter 7 to 9 discuss MHD instabilities that are observed in the Caltech plasma experiment. Chapter 7 describes an observation from the single loop experiment without prefill gas as mentioned in Section 2.1 and Chapter 4. Chapter 8 and 9 describe the observation from the astrophysical jet experiment, mentioned in Section 2.2.

In this chapter, a hoop force driven Magnetic Rayleigh-Taylor Instability (MRTI) is observed in a laboratory experiment that simulates a solar coronal loop. Increase of axial wavelength  $\lambda$  is observed when the axial magnetic field increases.

#### 7.1 Introduction

The Rayleigh-Taylor Instability (RTI) is an important instability in many astrophysical and laboratory systems, such as supernova explosions [47, 55], solar prominences [14, 56, 117], and inertial confinement fusion [17, 129]. RTI occurs when a heavy fluid is initially on top of a light fluid. If the low-density fluid is vacuum and the interface is planar and there is no magnetic field, the growth rate of this one-dimensional instability is

$$\gamma = \sqrt{gk}, \quad (7.1)$$

where  $g$  is the gravitational acceleration and  $k$  is the spatial wavenumber. The instability grows as  $\exp(\gamma t)$  with a ripple structure initially followed by later development

of plumes and finger-like structures. For a plasma supported above vacuum by a magnetic field parallel to the planar interface [74], the growth rate generalizes to

$$\gamma^2 = gk - \frac{2(\mathbf{k} \cdot \mathbf{B}_0)^2}{\mu_0 \rho}, \quad (7.2)$$

where  $\mathbf{B}_0$  is the unperturbed magnetic field. For a perturbation with  $\mathbf{k} \perp \mathbf{B}_0$ , also known as an interchange mode, the growth rate is the same as the RTI without a magnetic field. However, for a perturbation with  $\mathbf{k} \parallel \mathbf{B}_0$ , known as an undular mode, the growth rate is

$$\gamma^2 = gk - \frac{2(kB_0)^2}{\mu_0 \rho}. \quad (7.3)$$

The undular mode has a critical wavelength

$$\lambda_c = \frac{4\pi B_0^2}{\mu_0 \rho g} \quad (7.4)$$

at which  $\gamma = 0$ . If  $\lambda < \lambda_c$ ,  $\gamma^2 < 0$ , which implies that only perturbations with wavelength  $\lambda > \lambda_c$  can grow. Equation 7.3 also shows that there is a fastest growing wavelength which is given by

$$\lambda_m = 2\lambda_c = \frac{8\pi B_0^2}{\mu_0 \rho g} \quad (7.5)$$

and which corresponds to a maximum growth rate

$$\gamma_m = \sqrt{\frac{gk}{2}}. \quad (7.6)$$

Zhai and Bellan [166] derived the MHD theory of the MRTI on the surface of a magnetically confined cylindrical plasma flux rope. The Rayleigh–Taylor instability is found to couple to the classic current-driven instability, resulting in a new type of hybrid instability. We can see that the instability wavelength  $\lambda_m$  depends on the magnetic field  $B_0$  according to Eq. 7.5. The MRTI is thought to be the mechanism for the formation and dynamics of plumes in solar prominences. Berger et al. [14] observed the upflows from plumes caused by the MRTI. Ryutova et al. [117] described how the theoretically predicted growth rates and behaviors for the MRTI matched observations of quiescent prominence plumes. Hillier et al. [57] verified the MRTI mechanism for upflows from simulations. Keppens, Xia, and Porth [70] found the indications of secondary Kelvin–Helmholtz instabilities due to shear flows at the bubbles. However, the dependence on magnetic field strengths and how this

dependence affects observed differences are still not determined. An example of such differences is that some prominences produce many small plumes while others produce only large plumes [14]. RTI has been observed in the past in astrophysical jet experiment [98], but has never been observed in the solar loop experiment.

## 7.2 Experimental Setup

The single loop experiment (Sec. 2.1) involves several parameters that could be adjusted to produce a flux rope with different dynamics. A specific setting is needed for the production of RTI. Since the flux rope does not involve a helical kink instability as discussed in Chapter 4, a strong lateral acceleration is required for generation of a strong effective gravity. This can be achieved by using

1. Higher voltage applied across the plasma,  $V = 3.1 \rightarrow 4.3$  kV, to create a stronger axial current  $J_z$ .
2. Smaller bias field  $B_z$ , so that the plasma pinches down to a smaller minor radius.
3. Nitrogen gas with pressure 80 psi empirically displays the clearest images.

An observed RTI is shown in Figure 7.1.

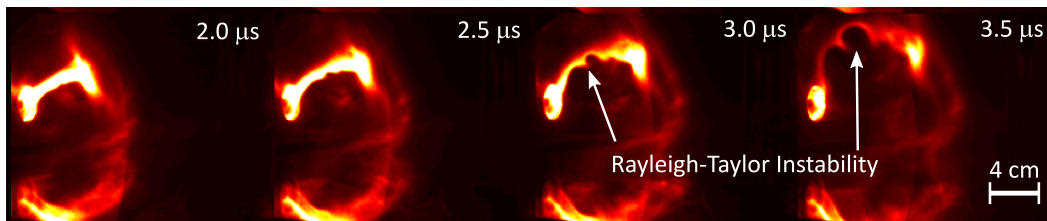


Figure 7.1: MRTI in a time series images of  $N_2$  plasma loop evolution.

## 7.3 Result

An axial magnetic field provided to the flux rope can be adjusted through changing the voltage  $V_b$  across the bias solenoids. An observed wavelength for the MRTI appears to be dependent on this axial magnetic field, as displayed in Figure 7.2.

A further characterization was done by Yang Zhang [168], showing that the observed MRTI wavelength is consistent with both the planar MRTI theory and the more detailed cylindrical MRTI theory.

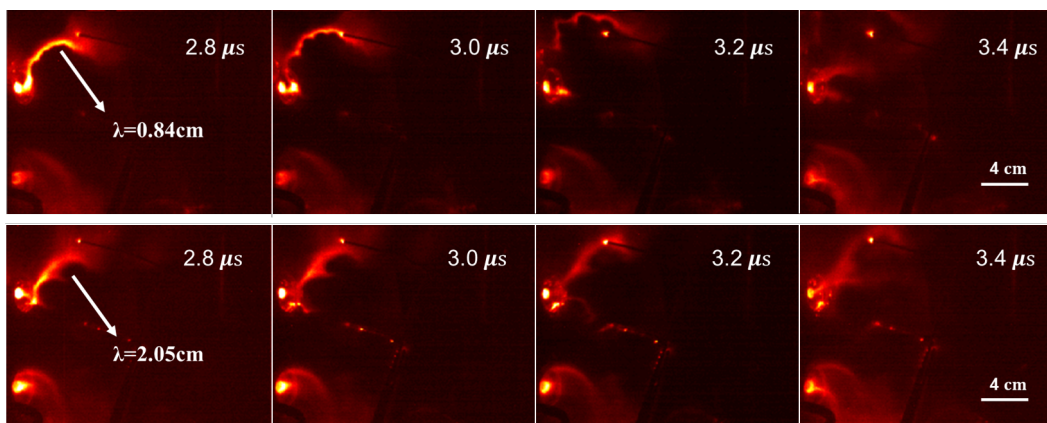


Figure 7.2: Time series images of  $N_2$  plasma loop evolution (upper shot# 7385 and  $V_b = 30$  V, lower shot# 7281 and  $V_b = 60$  V). Images were taken by Yang Zhang.

*Chapter 8***SIMULATION OF A SAUSAGE-LIKE PINCHING TO KINK  
INSTABILITY PROGRESSION LEADING TO A MAGNETIZED  
PLASMA DISRUPTION**

Byonghoon Seo, Pakorn Wongwaitayakornkul, Magnus A Haw, Ryan S Marshall, Hui Li, and Paul M Bellan. “Determination of a macro- to micro-scale progression leading to a magnetized plasma disruption”. In: *Physics of Plasmas* 27.2 (2020), p. 022109. DOI: <https://doi.org/10.1063/1.5140348>.

B.S. conducted the experiment, P.W. performed the simulation, M.A.H. measured whistler wave signal, R.S.M. detected hard x-ray signal, H.L. provided the simulation source code, B.S., P.W., and P.M.B. discussed and wrote the manuscript.

In this chapter, a numerical simulation of an MHD instability cascade is reported. It provides a feasible pathway that connects the MHD and kinetic scale.

We observe a plasma jet evolving through a macro- to micro- scale progression sequence. This leads to a fast magnetic reconnection that results in the jet breaking off from its originating electrode and forming a force-free state. A sausage-like pinching occurs first and squeezes an initially fat, short magnetized jet so that it becomes thin. The thin jet then becomes kink unstable. The lengthening of the jet by the kinking thins the jet even more since the kink is an incompressible instability. When the jet radius becomes comparable to the ion-skin depth, Hall and electron inertial physics become important and establish the environment for fast magnetic reconnection. This fast reconnection occurs, disrupting the jet and establishing a force-free state. X-ray bursts and whistler waves, evidence of magnetic reconnection, are observed when the plasma jet breaks off from the electrode. This experimentally observed sequence of successive thinning from pinching followed by kinking is reproduced in a three-dimensional ideal MHD numerical simulation. The results of the experiment and the numerical simulation together demonstrate a viable path from macro-scale MHD physics to micro-scale non-MHD physics where fast reconnection occurs.

## 8.1 Introduction

Magnetohydrodynamic (MHD) current-driven instabilities [2, 104, 123] have long been known to be fundamental to the behavior of magnetically confined plasmas. Another type of instability, magnetic reconnection, is also fundamental because it enables magnetic field topology-changing events such as spheromak formation [59, 131] and solar eruptions [122, 126]. These instabilities are also associated with tokamak stability [114, 156] and impulsive natural phenomena such as solar quasi-periodic pulsations [33, 136]. While finite resistivity enables reconnection in the MHD framework, resistive MHD reconnection is too slow to explain observations. Instead, in most cases of interest, reconnection is governed by much faster microscopic non-MHD processes involving Hall and electron inertia physics [113] missing from the more macroscopic MHD description. These Hall and electron inertia effects only become important at spatial scales smaller than the ion skin depth  $d_i = c/\omega_{pi}$ , which is microscopic and not resolved by MHD. However, because of the large scale separation it is unclear how MHD instabilities can couple to this Hall and electron inertia physics. One possibility is a cascade of MHD instabilities to successively smaller scales until the ion skin depth is reached [11, 98, 166].

Current-driven MHD instabilities are frequently observed in both laboratory and space plasmas [59, 115, 123] and are known to be associated with magnetic reconnection [98]. While it is unclear how macroscopic current-driven instabilities can couple to microscopic magnetic reconnection, previous theoretical and computational studies have suggested the possibility of a cascade through a transition of successively smaller scale current-driven instabilities. For example, a computational study on current-driven instabilities that used a 3D particle-in-cell code predicted the possibility of a sausage-to-kink cascade in the context of high energy particle production by a dense plasma focus [50]. Similarly, a recent analytic study by von der Linden and You [82] suggested a current-driven instability cascade but in an opposite path, i.e., as a kink-to-sausage cascade. These studies suggest that if an MHD cascade results in progressively finer scales, the ion inertia scale and its associated fast non-MHD reconnection might be accessed.

We report here experimental observations showing a sausage-like pinching-to-kink cascade that progresses to the ion inertia scale and then triggers a mechanism that results in fast magnetic reconnection. The observations show that sausage-like pinching leads to a kink instability and that because of the inherent incompressibility of the kink instability, the kinking leads to further thinning. This thinning attains

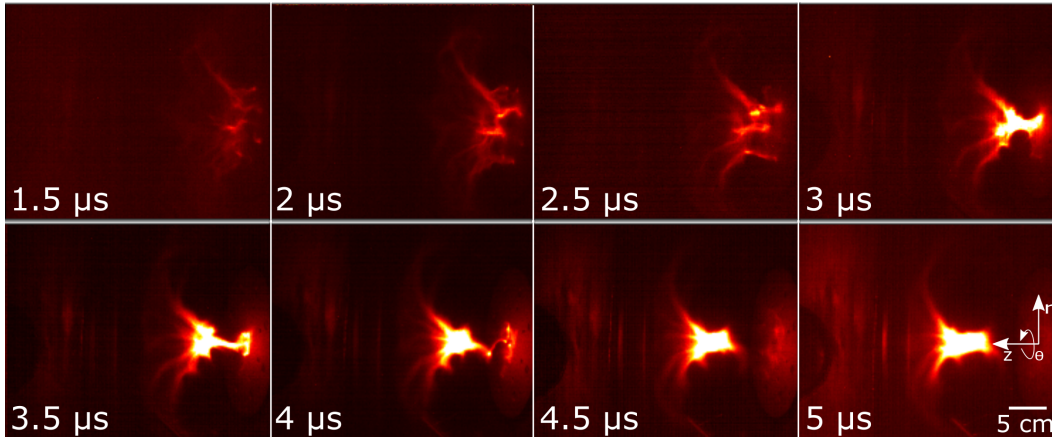


Figure 8.1: Time series of a nitrogen plasma shot taken by the fast movie camera. Images were taken by Byonghoon Seo.

the ion inertia scale and so results in fast magnetic reconnection. The observations of sausage-like pinching to kinking and thinning are reproduced in a 3D numerical MHD simulation.

## 8.2 Experimental Observation of Sausage-like to Kink Instability

The Caltech jet experiment is described in Section 2.2. A cylindrical coordinate system  $\{r, \theta, z\}$  is used in this chapter with the axis defined by the vacuum chamber. The poloidal direction corresponds to  $\{r, z\}$  and the toroidal direction is in  $\theta$ . This electrode setup is topologically identical to that used in spheromak experiments [31, 61, 64, 95, 102] and what is new here is the resolution of the distinct sequence wherein the plasma undergoes sausage-like pinching, then kinks, and then detaches from the originating electrode resulting in magnetic reconnection and, in a sub-microsecond time scale, formation of a force-free state (spheromak). The sausage-like pinch to kink sequence followed by kinking leading to further thinning to attain the ion inertia scale has been reproduced with high space and time resolution in a 3D numerical MHD simulation.

Most of the data reported here was obtained from hydrogen plasma shots except for the visible-light images in Fig. 8.1 which were obtained from nitrogen plasma shots. The reason for using these two gases is that as the plasma is radially compressed, its temperature increases and it becomes fully ionized. Since a hydrogen ion is just a proton and so has no bound electrons, a fully ionized hydrogen plasma emits no line radiation making it difficult to obtain a sharp visible-light image, whereas a nitrogen plasma has a sharp image.

Figure 8.1 shows a sequence of visible-light images of an evolving nitrogen plasma jet obtained using a fast movie camera. A cylindrical coordinate system  $\{r, \theta, z\}$  is used with the electrode plane defined to be  $z = 0$  (see  $5 \mu s$  frame in Fig. 8.1). At  $1.5 \mu s$  eight initial plasma-filled arched flux tubes merge to form a single axially moving current-carrying plasma-filled flux tube, i.e., a jet propagating in the  $z$  direction (to the left in Fig. 8.1). At the time of merging the jet has a large radius  $a$  and a small length  $L$  so at  $1.5 \mu s$  the jet aspect ratio  $L/a$  is small. Initial small perturbations grow exponentially during the time interval from  $1.5 \mu s$  to  $3.0 \mu s$  and pinch the jet so as to reduce  $a$  while maintaining  $L$  constant; this constitutes a sausage-like instability. This observed pinching is denoted sausage-like because strictly speaking it is not a sausage instability since it does not originate from a perturbation of an initial axisymmetric equilibrium as in the textbook analysis of a sausage instability. However, since MHD force-balance is lost as soon as a textbook sausage instability initiates, the evolution of the observed sausage-like pinching is exactly the same as that of a textbook theoretical sausage instability. Moreover, there is by definition no initial steady state plasma in a coaxial gun configuration powered by a capacitor bank because this configuration necessarily involves a ramping up of a current and so cannot provide an initial steady-state equilibrium. This situation is likely occurring in other experiments having an analogous set-up [31, 61, 64, 95, 102], i.e., none start from an initial textbook MHD equilibrium. On the other hand, results of the MHD simulation which will be described below show that although the initial condition is set to be the same as the experiment so that there is no initial steady-state equilibrium, a short-lived equilibrium (i.e., force balance) briefly develops just before onset of the sausage instability.

As a result of the sausage-like pinching decreasing the jet radius  $a$ , the jet becomes a thin flux rope with increased aspect ratio  $L/a$  as seen at  $3.5 \mu s$ . The jet becomes kink-unstable at  $4 \mu s$  and the helical deformation caused by the kinking now substantially increases  $L$ . Moreover, because the kink is an incompressible instability [104], the jet volume remains constant during the kink, so this increase of  $L$  necessitates a further reduction in  $a$  to maintain constant volume  $\sim a^2 L$ . At  $4 \mu s$  the jet length  $L$  is approximately three times longer than at  $3.5 \mu s$  and  $a$  is reduced by approximately a factor of two. At  $4.5 \mu s$  the jet radius  $a$  decreases to be order of the ion-skin depth; at this time the jet disrupts and detaches from the electrode indicating that magnetic reconnection occurs. This disruption is manifested by several distinct simultaneous phenomena, namely, X-ray emission, whistler wave emission, sudden change in the visible-light image indicating the plasma jet has detached from the electrode, and a

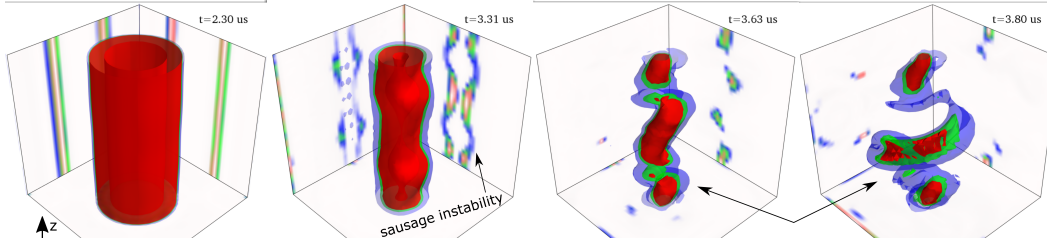


Figure 8.2: Time sequence of current density iso-surfaces obtained from simulation # 471. The two back planes at each time respectively show cross-sections of the current density at  $x = 0$  and at  $y = 0$ . The surface plots contain three iso-surfaces at levels 0.19 (blue), 0.32 (green), and 0.41 (red) of the maximum current density at each time.

change in magnetic topology as indicated by magnetic probes.

The fast magnetic reconnection occurs when  $v_d/v_A \simeq O(1)$  where  $v_d = J/ne$  is the electron drift velocity relative to ions and  $v_A$  is the Alfvén velocity which is comparable to the ion flow velocity; in this limit Hall and electron inertia terms in the electron equation of motion become important [11]. Using  $B_\theta = \mu_0 I/2\pi a$  and  $B_z = \psi/\pi a^2$  gives the  $v_d/v_A$  ratio as  $v_d/v_A = (I/\pi a^2 ne) \left( \sqrt{\mu_0 m_i n} / \sqrt{(\mu_0 I/2\pi a)^2 + (\psi/\pi a^2)^2} \right) = \lambda d_i / \sqrt{(\lambda a/2)^2 + 1}$  where  $d_i$  is the ion skin depth. The numerator  $\lambda d_i \simeq O(1)$  because  $\lambda \sim 100 \text{ m}^{-1}$  and  $d_i \sim 10^{-2} \text{ m}$ . Thus, the regime  $a \gg d_i$  corresponds to  $v_d/v_A \simeq 0$  and the regime  $a \simeq d_i$  corresponds to  $v_d/v_A \simeq O(1)$ ; hence shrinking of the flux rope radius to  $d_i$  satisfies the condition for fast magnetic reconnection to occur. Stark-broadening spectroscopy of the hydrogen plasma jet shows that the electron density is  $5 \times 10^{21} \text{ m}^{-3}$  which implies a 3 mm ion skin depth. The observations show that reconnection indeed occurs when the kink self-thinning reduces  $a$  to be comparable to the ion skin depth. The resistive skin depth  $\sim \sqrt{\eta/(\mu_0 f)}$  is about 15 mm for  $T_e = 2 \text{ eV}$  and 4.6 mm for  $T_e = 10 \text{ eV}$  ( $n_e = 5 \times 10^{21} \text{ m}^{-3}$ ,  $\ln \lambda = 10$ , using  $1/f = 0.5 \mu\text{s}$ ), and so the resistive skin depth is the same order of magnitude as the ion skin depth. However, resistive effects cannot be dominant because the observations of X-rays and whistler waves discussed below are inconsistent with resistive effects being dominant [11].

### 8.3 Simulation

The numerical simulation solves the 3-D ideal MHD equations and traces the evolution of mass density  $\rho$ , pressure  $p$ , velocity  $\vec{v}$ , and magnetic field  $\vec{B}$  in a numerical

Cartesian box of size  $2R_0$  where  $0.7R_0$  is the initial flux tube radius. Initial conditions are based on the experimental jet parameters at  $2 \mu\text{s}$  and are as follows: (i) a uniform skin current with  $I \simeq 90 \text{ kA}$  is introduced at  $r = 5 \text{ cm}$ ; (ii) the plasma mass density in the flux tube is set to be  $\rho_0 = nm_H = 5.0 \times 10^{21} \text{ u/m}^3$  where  $n$  is the density in  $\text{m}^{-3}$  and  $m_H$  is the hydrogen mass in  $\text{u}$  and the temperature is  $2 \text{ eV}$ ; (iii) a  $z$ -directed magnetic field  $B_{z,\text{sim}} = 224 \text{ G}$  is uniformly applied in the simulation domain; (iv) small perturbations are added to the density to induce the instabilities. The total initial density is  $\rho(\mathbf{r}) = \rho_{\text{main}} + \rho_{\text{sausage}} + \rho_{\text{kink}}$ , where the main loop density and the respective perturbations for the kink and sausage modes are

$$\rho_{\text{main}} = \rho_0 \exp\left(\frac{-r^2}{2\sigma_0^2}\right),$$

$$\rho_{\text{sausage}} = 0.1\rho_0 \exp\left(\frac{-r^2}{2(\sigma_0 - \sigma_s \cos(k_{\text{sausage}}z))^2}\right),$$

and

$$\rho_{\text{kink}} = 0.1\rho_0 \exp\left(-(\mathbf{r} - \mathbf{r}')^2/R_0^2\right) \exp\left(-r^2/2\sigma_k^2\right).$$

Here  $\mathbf{r}' = r_0[\cos(k_{\text{kink}}z)\hat{x} + \sin(k_{\text{kink}}z)\hat{y}]$ ,  $\sigma_0 = 3.6 \text{ cm}$ ,  $\sigma_s = 0.36 \text{ cm}$ ,  $\sigma_k = 2.2 \text{ cm}$ , and  $r_0 = 0.7 \text{ cm}$ . Respective wavenumbers  $k_{\text{kink}} = 1.4 \times 10^{-2} \text{ m}^{-1}$  and  $k_{\text{sausage}} = 1.3 \times 10^{-2} \text{ m}^{-1}$  are chosen corresponding to the unstable modes observed in the experiment. The plasma column is initially at rest and a small flow velocity ( $6 \text{ km/s}$  at the top and bottom and linearly decreases on approaching the center ( $z = 0$ )) in the  $\pm z$  directions is initially imposed to simulate the axial motion of the jet; this flow velocity does not play a major role, but provides imbalance between periodic bulged structures to mimic the axial motion of the pressure gradient in  $\pm z$  direction.

Figure 8.2 shows the simulation results as a time sequence of current density iso-surfaces. A flux tube evolves with an initial skin current configuration and initial small aspect ratio  $L/a$ . The initial condition was set to be the same as the experiment so the flux tube is initially not in equilibrium and the inward radial force pinches the flux tube. Since the magnetic and thermal pressure increase by the radial pinching, a radial force balance is established at  $2.7 \mu\text{s}$  and the flux tube becomes stable (see Fig. 8.3). Then, the flux tube develops a sausage instability at  $3.3 \mu\text{s}$ . The sausageing increases  $L/a$  to form a highly collimated current channel. A kink instability spontaneously starts at  $3.6 \mu\text{s}$ . The numerical simulation thus confirms that the flux tube can transition from being sausage unstable to being kink unstable.

In addition, the simulation shows that regions where  $v_d/v_A \sim O(1)$  develop when the jet kinks implying that non-ideal MHD physics and resulting fast reconnection

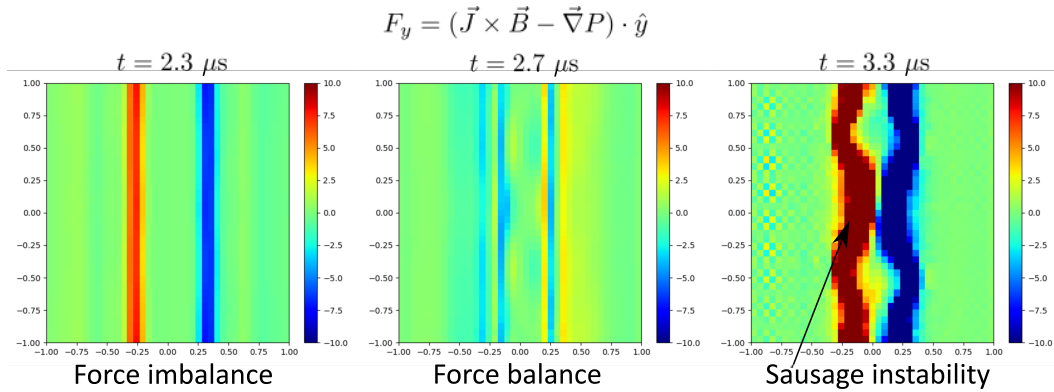


Figure 8.3: Time-dependent radial force obtained from numerical simulation. Initially the flux tube is not in equilibrium so the direction of the radial force at  $2.3 \mu\text{s}$  is inward. By pinching the flux tube, a temporary radial force balance is established at  $2.7 \mu\text{s}$ . Sausage instability occurs at  $3.3 \mu\text{s}$ .

should occur at these locations (see Fig. 8.4). Being MHD, the simulation does not replicate the fast non-MHD physics, but simply indicates when and where the MHD physics has accessed the ion skin depth scale.

In conclusion, we have experimentally observed a plasma jet transition from a sausage-like pinching to a kink instability which then leads to magnetic reconnection. The sausage-like pinching occurs first and pinches a fat, short magnetized jet to become a thin, long magnetized jet. The thin, long jet then becomes kink unstable. The incompressible kinked jet further lengthens and to maintain constant volume, the kinked jet thins even more. Because of this thinning, the jet radius becomes comparable to the ion-skin depth setting off Hall and electron inertial physics that result in fast magnetic reconnection, jet disruption, and establishment of a nearly force-free state. X-ray bursts and whistler waves, evidence of fast magnetic reconnection, are observed during this process validating that non-MHD physics has been accessed. The experimentally observed progression to ion-skin depth scales has been confirmed by a three-dimensional ideal MHD numerical simulation. The experiment and its numerical confirmation together establish a mechanism linking macroscale ideal MHD (no reconnection, scale exceeding ion skin depth) to microscale physics (fast reconnection, scale less than ion skin depth, X-rays, whistler waves).

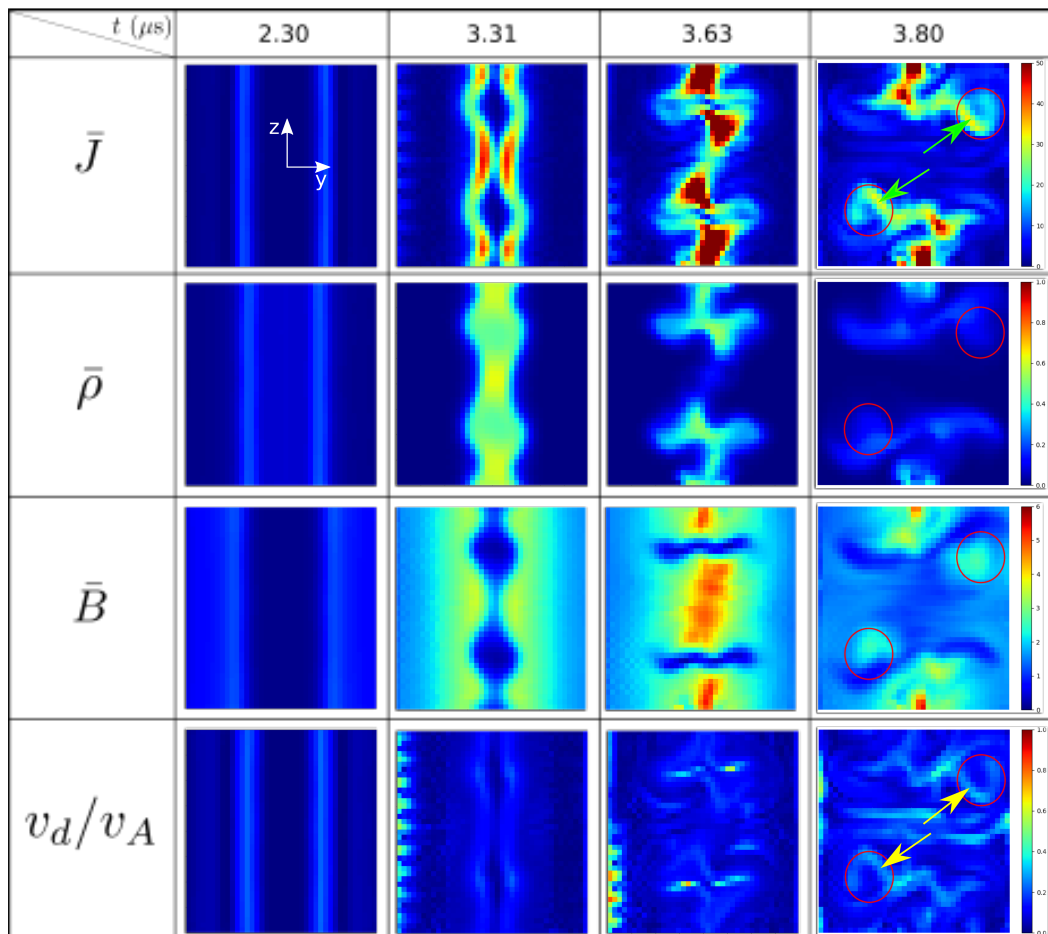


Figure 8.4: Time sequence of  $\bar{J}$ ,  $\bar{\rho}$ ,  $\bar{B}$ , and  $v_d/v_A$  in the  $y$ - $z$  ( $x = 0$ ) plane obtained from simulation # 471. The  $\bar{J}$  plots are the same as the back right planes in Fig. 5 but are shown with continuous color contours. The flux rope becomes sausage unstable at  $3.31 \mu\text{s}$  and then kink unstable so the flux rope kinks into and out of the page after  $3.63 \mu\text{s}$ . The regions where the flux rope passes through this plane are indicated by red circles. The ratio  $v_d/v_A$  becomes large at the locations indicated by yellow arrows at  $3.80 \mu\text{s}$  because  $\bar{J}$  becomes large at these locations as indicated by green arrows.

*Chapter 9***3D NUMERICAL SIMULATION OF KINK-DRIVEN  
RAYLEIGH-TAYLOR INSTABILITY LEADING TO FAST  
MAGNETIC RECONNECTION**

Pakorn Wongwaitayakornkul, Hui Li, and Paul M Bellan. “3D Numerical Simulation of Kink-Driven Rayleigh-Taylor Instability Leading to Fast Magnetic Reconnection”. In: *Under Review* (2020).

P.W. performed the simulation. H.L. provided the simulation source code. P.W. and P.M.B discussed and wrote the manuscript.

In this chapter, we look at the last instability cascade that could provide a pathway to magnetic reconnection. The instability was first observed in 2012 [98]. This is the first numerical simulation for the mechanism.

While fast magnetic reconnection involving non-MHD micro-scale physics is believed to underlie both solar eruptions and laboratory plasma current disruptions, the process by which large-scale MHD couples to the micro-scale physics is not understood. An MHD instability cascade from a kink to a secondary Rayleigh-Taylor instability in the Caltech astrophysical jet laboratory experiment provides new insights into this coupling and motivates a 3D numerical simulation of this transition from large to small scale. A critical finding from the simulation is that the axial magnetic field inside the current-carrying dense plasma must exceed the field outside. In addition, the simulation verifies a theoretical prediction and experimental observation that, depending on the strength of the effective gravity produced by the primary kink instability, the secondary instability can be Rayleigh-Taylor or mini-kink. Finally, it is shown that the kink-driven Rayleigh-Taylor instability generates a localized electric field sufficiently strong to accelerate electrons to very high energy.

**9.1 Introduction**

Plasma stability has long been a subject of great interest in many situations. As notable examples, a stable plasma is essential to achieve nuclear fusion and, in the solar corona, plasma instabilities are considered to be the cause for energetic phenomena. Bernstein et al. [16] were the first to study ideal magnetohydrodynamic

(MHD) stability of plasma via the MHD energy principle which states that if a perturbation lowers the total potential energy of a non-dissipative (ideal) MHD plasma, the perturbation is unstable. The energy principle involves assuming a small displacement from an initial equilibrium, then deriving linearized equations formulated as a normal-mode eigenvalue problem, and finally showing that plasmas governed by ideal MHD are susceptible to two distinct types of instabilities, denoted as pressure-driven and current-driven. A common example of pressure-driven instability, the Rayleigh-Taylor instability (RTI) [75, 112, 130], takes place at the interface between a heavy fluid sitting on top of a light fluid in a gravitational field. A common example of current-driven instability, the kink instability (KI), involves a flux rope with initially straight axis having the axis become helical (writhing of flux rope) so as to lower overall magnetic energy and tend towards a force-free state. Both the KI [115] and the RTI [22] have been observed in the solar corona.

Magnetic reconnection, a microscopic instability involving physics beyond ideal MHD, is thought to be responsible for many solar eruptive events such as flares, and coronal mass ejections. The simplest reconnection model is based on taking into account finite resistivity in MHD and was proposed by Sweet [128], Parker [109], and Furth, Killeen, and Rosenbluth [39]. However, the predicted rate for this “resistive” reconnection is far too slow to describe actual solar eruptive events and many laboratory plasma reconnection observations so a more sophisticated, faster microscopic model is needed. Models for fast reconnection are the subject of much ongoing research [35, 36, 159] and typically involve microscopic physics beyond the scope of resistive MHD. This fast reconnection physics involves finite ion skin depth, finite electron inertia, and Hall terms all of which are small scale and omitted from MHD. However, it is unclear how MHD, a macroscopic description, couples to the microscopic non-MHD scale where fast reconnection occurs.

The Caltech astrophysical jet experiment [9] has provided some insights into this coupling because both the macroscopic MHD scale and the microscopic non-MHD scale can be resolved. An MHD-driven dense plasma jet is created in this experiment by a coaxial magnetized plasma gun located inside a large cylindrical vacuum chamber. The motion is described using a cylindrical coordinate system  $\{r, \theta, z\}$  where the  $z$  axis is along the vacuum chamber axis, the  $r, z$  directions are denoted poloidal, and the  $\theta$  direction denoted toroidal. The sequence of operation starts with establishment of a dipole-shape bias poloidal magnetic field (peak value  $\sim 0.1$  T). Neutral gas is then injected into the vacuum chamber using fast gas valves connected

to discrete nozzles located on coaxial disk and annulus electrodes at  $z = 0$ . After gas injection, a high-voltage (3 kV) is applied across the electrodes from a capacitor bank to breakdown the gas to form plasma. The capacitor discharge ramps up 50 – 150 kA current that flows along poloidal magnetic field flux surfaces and produces an associated toroidal magnetic field. Magnetic forces associated with this current squeeze together poloidal flux surfaces radially and distend these surfaces axially so plasma frozen to these flux surfaces collimates and becomes a  $\sim 40 \text{ km s}^{-1}$  jet that propagates in the  $z$  direction from the electrodes into the chamber. The jet lasts about  $20 \mu\text{s}$  and its flow and collimation agree with predictions based on detailed analytical and numerical consideration of MHD forces [9, 10, 76, 164, 167]. The jet formation, collimation, and axial lengthening have been observed using a fast movie camera. Hsu and Bellan [59] observed a clear KI using the fast movie camera while Moser and Bellan [98] detected a secondary RTI that happened on the inner (trailing) side of the KI. The KI growth means that the plasma jet moves laterally from the  $z$ -axis with exponentially increasing displacement and so undergoes a large lateral acceleration perpendicular to the  $z$ -axis. In the frame of this laterally accelerating plasma, the system of heavy fluid (plasma) and light fluid (vacuum) thus experience a strong effective gravity  $g$  pointing towards the  $z$ -axis. As seen in Figure 9.1 the Kink-Driven Rayleigh-Taylor instability (KDRT) occurs on the trailing side of the KI corresponding to the dense plasma being “on top of” the diffuse external region. The time scale of the RTI is about three times shorter than the KI time scale so the two instabilities are decoupled other than the KI providing  $g$ . The minor radius of the current-carrying flux rope decreases with spatial periodicity as a result of the choking effect of the RTI ripples. Fast reconnection takes place when the flux rope is choked to a radius comparable to the ion skin depth  $d_i = c/\omega_{pi}$ . When this happens several simultaneous phenomena occur, namely: a strong localized EUV emission [23], a strong localized reduction of visible light, a voltage spike, a hard x-ray burst [94], and a whistler wave burst [52]. These non-MHD phenomena indicate that the choking of the jet radius by the KDRT is the macroscopic ideal MHD mechanism that allows the initially MHD-governed plasma to access the microscopic  $d_i$  length scale where fast reconnection occurs.

While extensive numerical studies of both KI [15, 139] and RTI [162, 163] individually exist, no numerical simulation of KDRT has been demonstrated. Since the lab experiments indicate that KDRT provides a cascade path from macroscopic ideal MHD to microscopic fast reconnection, it is likely that KDRT can also explain many energetic events observed in nature. This suggests that a numerical simula-

tion would be extremely valuable and could be checked against the experiment and existing analytic models. For example, Zhai and Bellan [166] proposed a quantitative analytic model for how lateral acceleration of a cylindrical current-carrying plasma could result in either RTI or a mini-kink depending on the ratio of lateral gravitational acceleration to the pinch force resulting from the current. However, this model did not arrange for the lateral acceleration to be from a primary KI and there was no numerical simulation showing the RTI being driven by a KI. Similarly, a statistical model of electron acceleration from a reconnecting electric field was developed [93], but there was no numerical verification using actual geometry.

Simulating the KDRT numerically poses many challenges. First, the code must include finite  $\beta$ , since the equilibrium preceding the RTI involves a balance between magnetic and hydrodynamic pressure. Equally important, there must be a density jump or gradient to have a heavy fluid on top of a light fluid when the effective gravity is developed by the KI. Second, the code has to capture the instability in full 3D at high resolution because multiple length scales are involved and because the KI and RTI are fundamentally three-dimensional as they involve a writhing flux rope. The code also has to resolve three different time scales, namely the jet collimation time scale ( $\tau_{\text{col}}$ ), the KI time scale ( $\tau_{\text{kink}}$ ), and the RTI time scale ( $\tau_{\text{RT}}$ ), where  $\tau_{\text{col}} \gg \tau_{\text{kink}} \gg \tau_{\text{RT}}$ .

We report here 3D numerical simulation of the KDRT. This simulation, achieved using resistive MHD, is in good agreement with the experimental observations and also with the predictions of Zhai and Bellan [166] regarding the secondary instability being either RTI or mini-kink. Section 9.2 describes the simulation model by presenting the system of equations and the initial and boundary conditions. Section 9.3 discusses the circumstances leading to KDRT and specifically shows that spatial localization of the axial magnetic field  $B_z$  is a key requirement. This localization is achieved experimentally via the collimation process and corresponds to the jet being paramagnetic [81]. Section 9.4 numerically validates the analytic results predicted by Zhai and Bellan [166], showing that the secondary instability could be either RTI or mini-kink depending on the dimensionless parameter  $\Phi^2 = ga/v_{A\theta}^2$  where  $v_{A\theta}$ , an Alfvén velocity calculated using  $B_\theta$  only, serves as a measure of the pinch force. Section 9.5 discusses the assumptions made regarding resistivity and the acceleration of test particles injected into a resistive MHD plasma; this section shows that particles will be accelerated to high energy when there is a localized anomalous resistivity imposed as a proxy for the micro-physics associated with

fast magnetic reconnection. Section 9.6 relates the simulation to the laboratory observations and the applicability of the simulation to the solar corona.

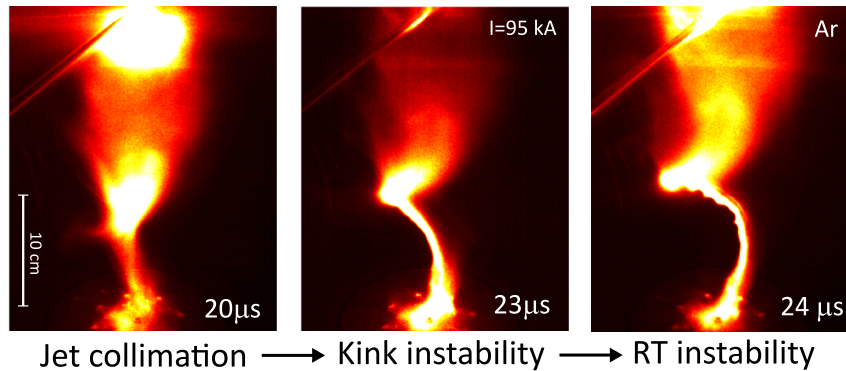


Figure 9.1: The evolution of KDRT instability development on argon plasma jet (shot#11,225) shows an inner ripple RTI on the inner side of a helical kink. The white label indicates the time after the plasma breakdown.

## 9.2 3D Resistive MHD Simulation

The 3D MHD numerical simulation was performed on the Los Alamos Turquoise supercomputer cluster using part of the Los Alamos COMPUTational Astrophysical Simulation Suite [80] which is a collection of several modern, high resolution, Godunov-type, MHD codes. This Suite had been previously used to model the Caltech astrophysical jet and solar loop experiments [158, 167]. An important difference here is that a spatially and temporally dependent finite resistivity is included. The initial situation is a flux rope (finite radius cylinder with helical magnetic field and embedded finite density plasma) surrounded by extremely low density plasma. The code tracks the evolution of 8 dimensionless parameters namely: density  $\rho$ , velocity  $\mathbf{v}$ , magnetic field  $\mathbf{B}$ , and pressure  $P$  inside a Cartesian box of size  $[-L, L]^3$  where  $L = 10a$  and  $a$  is the flux rope initial radius. The dimensionless parameters are obtained by normalizing to associated dimensioned reference parameters. These reference parameters are the azimuthal magnetic field just outside the plasma column  $B_0 = B_\theta(r = a)$ , the initial density on the flux rope axis  $\rho_0 = \rho(r = 0)$ , the domain half-length  $L$ , the Alfvén velocity associated with the azimuthal magnetic field  $v_A = B_0/\sqrt{\mu_0\rho_0}$ , the Alfvén time  $\tau_A = L/v_A$ , the initial on-axis pressure  $p_0 = \rho_0 v_A^2$ , and the initial hydrodynamic energy  $p_0 L^3$ . The Lundquist number is defined as  $S = \mu_0 v_A L/\eta$ .

The dimensionless resistive MHD equations in conservative form are

$$\frac{\partial \rho}{\partial t} + \nabla \cdot (\rho \mathbf{v}) = 0 \quad (9.1)$$

$$\frac{\partial(\rho \mathbf{v})}{\partial t} + \nabla \cdot \left( \rho \mathbf{v} \mathbf{v} + \left( P + \frac{B^2}{2} \right) \overleftrightarrow{\mathbf{I}} - \mathbf{B} \mathbf{B} \right) = 0 \quad (9.2)$$

$$\frac{\partial e}{\partial t} + \nabla \cdot \left[ \left( e + P + \frac{B^2}{2} \right) \mathbf{v} - \mathbf{B}(\mathbf{v} \cdot \mathbf{B}) \right] = 0 \quad (9.3)$$

$$\frac{\partial \mathbf{B}}{\partial t} - \nabla \times (\mathbf{v} \times \mathbf{B}) - \frac{1}{S} \nabla^2 \mathbf{B} = 0, \quad (9.4)$$

where the total energy density is  $e \equiv \rho v^2/2 + P/(\gamma - 1) + B^2/2$  with  $\gamma = 5/3$ . The initial condition is that of an axisymmetric flux rope with uniform axial current density  $J_z = I/(\pi a^2)$  for  $r < a$  and  $J_z = 0$  for  $r > a$ . In one configuration (extreme paramagnetism) a uniform axial magnetic field  $B_z$  exists only inside the current channel ( $r < a$ ) while in another configuration  $B_z$  exists over the entire domain. The code evolves the vector potential  $\mathbf{A} = (A_x, A_y, A_z)$  to maintain the divergenceless condition of the magnetic field,  $\nabla \cdot \mathbf{B} = 0$ . The density is set to have a Gaussian profile that decays radially from the flux rope axis which is located at position  $\mathbf{r}_0$ . A small uniform background density  $\rho_b$  was added to avoid requiring an infinitely small time step. The plasma is initially at rest with a uniform temperature,  $T = P/\rho = 1$ . The initial density, pressure, velocity, and vector potential are specified as

$$\rho = \rho_0 \exp\left(-(\mathbf{r} - \mathbf{r}_0)^2/2\sigma^2\right) + \rho_b \quad (9.5)$$

$$P = \rho, \quad \mathbf{v} = 0, \quad A_x = 0, \quad A_y = B_z x \quad (9.6)$$

$$A_z = \begin{cases} -(I/4\pi)(r/a)^2 & , r < a \\ -(I/4\pi)(1 + 2 \ln(r/a)) & , r > a, \end{cases} \quad (9.7)$$

where  $\rho_0 = 1$ ,  $\mathbf{r}_0 = 0$ ,  $\rho_b = 0.01$ ,  $\sigma = 0.1$ ,  $I = 1$ ,  $a = 0.1$ , and  $B_z = 0.3$ . For the paramagnetic configuration  $B_z$  is finite inside the flux rope ( $r < a$ ) only. The parameters are chosen so that  $P(r = 0) \sim B_\theta(r = a)^2/2$  and the flux rope is in approximate radial equilibrium since  $B_z \ll B_\theta$ . Resistivity is set to zero ( $\eta = 0$ ) in Sections 9.3–9.4 but then is set to be finite and spatially dependent in Section 9.5. Seed perturbations for both KI and RTI are added to the initial state by setting  $\mathbf{r}_0 = \sin(2\pi z/\lambda_{\text{KI}})\hat{i} + \cos(2\pi z/\lambda_{\text{KI}})\hat{j}$  to provide a KI seed, and by setting  $\sigma = a(1 + 0.1 \sin(2\pi z/\lambda_{\text{RTI}}))$  to provide a RTI seed. The seed perturbations have  $\lambda_{\text{RTI}} = 0.1$  and  $\lambda_{\text{KI}} = 1$ . Spatial boundary conditions are current-conserving non-reflecting outflow at the bounding surfaces.

Figure 9.2 shows the time evolution of the numerical simulation. On the left ( $t = 0.3\tau_A$ ), the plasma is initially in a near straight cylinder equilibrium with the small KI and RTI seed perturbations visible. The KI takes place on the Alfvén time scale and so appears at  $t = 0.9\tau_A$  (middle in Figure 9.2). The lateral acceleration of the kink produces the effective gravity that sets off the RTI which grows on a much shorter time scale ( $\sim 0.2\tau_A$ ). The density isosurfaces at  $t = 1.1\tau_A$  show that the RTI has approximately e-folded and has the same short wavelength as the RTI seed perturbation.

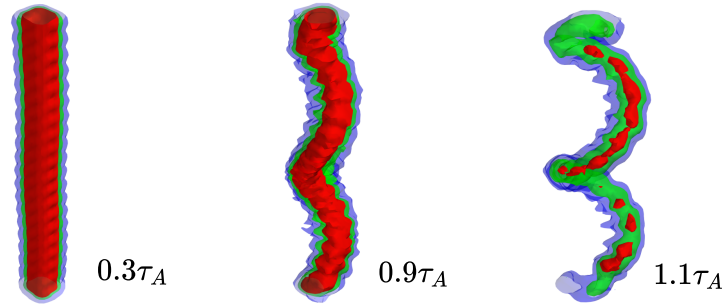


Figure 9.2: Simulated KDRT at three different timesteps.  $\tau_A$  is the Alfvén time of the simulation. The isosurfaces represent  $\{0.2\rho_0, 0.3\rho_0, 0.4\rho_0\}$  with {blue,green,red} respectively.

On using imputed experimental parameters  $n_0 = 10^{23} \text{ m}^{-3}$ ,  $B_0 = 1.9 \text{ T}$ ,  $L = 10 \text{ cm}$ ,  $\kappa T = 2 \text{ eV}$ , and  $m_i = 40 \text{ u (Ar)}$ , it follows that  $v_A = 20 \text{ km s}^{-1}$  and  $\tau_A = 5 \mu\text{s}$ . The predicted time scale for each process matches well with the observed time scale, i.e.,  $\tau_{\text{col}} = 2\tau_A \rightarrow 10 \mu\text{s}$ ,  $\tau_{\text{kink}} = 0.9\tau_A - 0.3\tau_A = 0.6\tau_A \rightarrow 3 \mu\text{s}$ , and  $\tau_{\text{RT}} = 1.1\tau_A - 0.9\tau_A = 0.2\tau_A \rightarrow 1 \mu\text{s}$  where the arrow represents converting the dimensionless quantity to its associated dimensioned value. The word ‘imputed’ is used here because the minor radius of 1 cm is too small for a probe measurement and the kink dynamics is too fast and unpredictable for an interferometer measurement.

### 9.3 Conditions for KDRT

As demonstrated in Figure 9.3, the simulation shows that  $B_z$  must be localized in the flux rope for the kink-driven RTI to develop. Having  $B_z$  much larger inside the flux rope than outside corresponds to the flux rope being highly paramagnetic [81]. Figure 9.3 compares the localized  $B_z$  case (i.e., paramagnetic) to the case where  $B_z$  exists everywhere. In Figure 9.3a,  $B_z$  is applied everywhere in the domain, while in Figure 9.3b,  $B_z$  is finite only inside the flux rope. Even though all other parameters are identical, KDRT is only observed when  $B_z$  is localized to be inside the flux

rope. This paramagnetic situation corresponds to the natural state of the experiment because the jet collimation process squeezes together axial magnetic field lines that were initially spread apart [59]. Since magnetic field strength is just the density of field lines, the squeezed together field lines are by definition paramagnetic. This non-uniformity and paramagnetism is also expected in the solar corona context because the collimation of solar flux ropes similarly requires the gathering together of axial magnetic field lines that were initially spread apart [72].

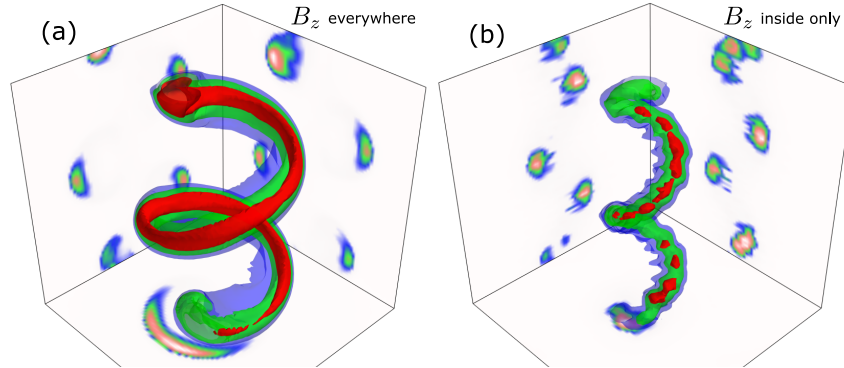


Figure 9.3: Isosurfaces snapshot of density in two cases: (a) with uniform  $B_z = 0.3$  and (b) with  $B_z = 0.3$  only inside the flux rope ( $r < a$ ). Both cases are taken at the same time  $t = 1.1\tau_A$ . The colors {blue,green,red} indicate the levels {0.5,0.7,0.9} of the maximum density of that time frame accordingly. The planes show cross-sectional contour of the density in the midplane.

This requirement for axial magnetic field paramagnetism demonstrated in Figure 9.3 suggests that axial magnetic field outside the flux rope has a stabilizing effect and inhibits the RT ripples from developing. An analytical growth rate of the RTI in a slab geometry on an interface between a plasma with density  $\rho$  and a vacuum is

$$\gamma = gk - \alpha \frac{(\mathbf{k} \cdot \mathbf{B})^2}{\mu_0 \rho}, \quad (9.8)$$

where  $g$  is a gravitational acceleration,  $k$  is the RTI wavenumber, and  $\mathbf{B}$  is a magnetic field parallel to the interface.  $\alpha = 1$  when this magnetic field is present on only one side of the interface and  $\alpha = 2$  when this magnetic field is present on both sides [42, Sec. 6.6.4]. The predicted growth rate is smaller when  $\alpha = 2$ , so the uniform magnetic field across the interface provides a stronger stabilization to the instability. Although the RTI developed here is on a cylindrical geometry, the stabilizing trend should also apply to a RTI developed in a slab geometry.

#### 9.4 Effect on $\Phi^2$

Zhai and Bellan [166] proposed that, under certain conditions, a current-carrying flux rope immersed in a gravitational field should exhibit an instability intermediate between current-driven and pressure-driven. This hybrid instability depended on a cross-coupling between members of the broad spectrum of azimuthal modes required to accommodate both the Cartesian geometry  $\{x, y, z\}$  of lateral gravity and the cylindrical geometry  $\{r, \theta, z\}$  of a flux rope. This situation is both more complicated and more realistic than the traditional Cartesian model of the RTI and the traditional cylindrical model of the KI. Zhai and Bellan [166] defined a dimensionless parameter  $\Phi^2 = ga/v_{A\theta}^2$  where  $v_{A\theta} = B_0/\sqrt{\mu_0\rho_0}$  and showed that if  $\Phi^2 \gg 1$  the flux rope was more susceptible to RTI and if  $\Phi^2 \ll 1$  the flux rope was more susceptible to KI. Figure 9.4 compares the  $\Phi^2$  regimes for the analytic solution, the experiment, and the 3D MHD numerical simulation (the analytic solution and experiment are from Zhai and Bellan [166] and the 3D numerical solution is the new result presented here). In the illustration column, two curved flux ropes are shown. The upper row shows a flux rope with  $\Phi^2 \gg 1$ , the RTI-dominated case, while the lower row shows a flux rope with  $\Phi^2 \ll 1$ , the KI dominated case. The parameter  $\Phi^2$  can be expressed as  $\Phi^2 = ga/v_{A\theta}^2 = \mu_0\rho ga/B_\theta^2 = \mu_0 m_i n_i ga/B_\theta^2$ . In the experiment [166], the two cases ( $\Phi^2 \gg 1$  and  $\Phi^2 \ll 1$ ) have comparable  $g$ ,  $a$ ,  $B_\theta$ , and  $n_i$ . The difference in value of  $\Phi^2$  comes from ion mass: argon ( $m_i = 40$  u) is used in the  $\Phi^2 \gg 1$  case and hydrogen ( $m_i = 1$  u) is used in the  $\Phi^2 \ll 1$  case. In the simulation, the normalization constant for temperature is defined as  $\kappa T_0 = m_i P_0/\rho_0$ . Therefore, lowering  $m_i$  is equivalent to lowering  $T_0$  while keeping the other parameters fixed. Increasing the pressure, while maintaining the plasma density, increases the numerical value of the temperature. Suppose in the experiment the temperature of both argon and hydrogen plasma are the same ( $\kappa T \sim 2$  eV), varying the background pressure  $p_b$  is equivalent to varying  $m_i$  in the experiment. Consequently,  $\Phi^2$  can be tuned by changing  $m_i$  in the experiment and  $p_b$  in the simulation. In the simulation column of Figure 9.4,  $p_b = 10^{-4}$  in the upper row and  $p_b = 1$  in the lower row.

#### 9.5 Electron Acceleration

Numerical and theoretical investigations [20, 65] have shown that microphysical kinetic instabilities are triggered when the electron drift velocity relative to ions, i.e.,  $v_d = J/ne$ , exceeds a threshold value. When this happens, electrons are scattered by the microscopic wave turbulence leading to a reduction in directed electron

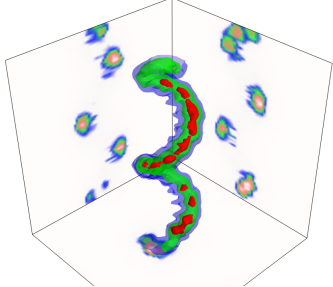
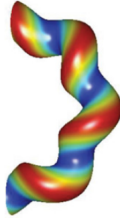
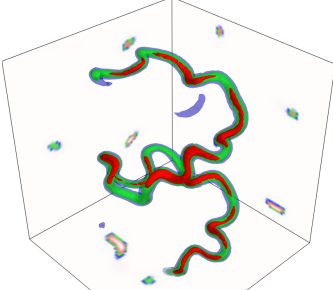
$\Phi^2$	Illustration	Experimental Image	Numerical Simulation
$\gg 1$			
$\ll 1$			

Figure 9.4: The table shows the two limits of the instability: (a)  $\Phi^2 \gg 1$  and (b)  $\Phi^2 \ll 1$ . The instability is shown in the Illustration column, where the shape of the instability is calculated analytically. Secondly, the different regimes are captured with fast camera. The right hand column shows the 3D numerical simulation. The numerical plots are isosurfaces of density. The figures in Illustration and Experimental Image columns are adapted from Zhai and Bellan [166]. The Numerical Simulation column is the result of this work.

momentum and hence an increase in the effective plasma resistivity. This section addresses the effect of this “anomalous” resistivity. Section 9.5 describes how such an anomalous resistivity affects the MHD simulation; the anomalous resistivity  $\eta$  is switched on in the region where  $v_d$  exceeds some threshold. Section 9.5 describes the trajectory of test electrons in the presence of the simulation magnetic field and the electric field created by the anomalous resistivity. Because the test electrons have very fast trajectories, we assume the plasma does not change when calculating these trajectories. The justification for this “frozen plasma” assumption is that the cyclotron period is  $\tau_c = 2\pi m_e / eB_0$  and the electron thermal speed is  $v_T = \sqrt{2kT/m_e}$  so  $\tau_A/\tau_c = eL\sqrt{\mu_0 m_i n_i} / 2\pi m_e = 2.6 \times 10^5$  and  $v_T/v_A = \sqrt{2kT\mu_0 m_i n_i / m_e} / B_0 = 40$ . On defining the test electron transit time  $\tau_T = L/v_T$ , it is seen that  $\tau_A/\tau_T \gg 1$ . Initially, the ion skin depth  $d_i = (c/e)\sqrt{\epsilon_0 m_i / n} = 0.5 \text{ cm} < a$ . Then, KDRT chokes down the current cross-section to be below  $d_i$  prompting fast reconnection.

### Anomalous Resistivity

Fast reconnection occurs at the microscopic  $d_i$  scale when non-MHD kinetic physics becomes important and the concept of resistivity is an oversimplification. Because of the complexity of the micro-scale physics, it is not computationally feasible to describe these effects in correct detail in a code that also describes the 3D MHD physics. However, by making some simplifying physical arguments [152] one can gain insights into the effect of the microphysics. These arguments consist of adding a large ad hoc localized anomalous resistivity to the 3D MHD code. While this addition does not accurately describe the microphysics of the fast magnetic reconnection, it does give insight into the accelerating process of the electrons.

The condition to trigger the ad hoc anomalous localized resistivity  $\eta_a$  is for the current density  $J$  to exceed a certain threshold  $J_c$ . This is quantitatively expressed as

$$\eta(J, t) = \eta_a H(J - J_c) H(t - t_c), \quad (9.9)$$

where  $\eta_a = \mu_0 L v_A / S_a$  is the normalized anomalous resistivity,  $S_a$  is the anomalous Lundquist number,  $J_c$  and  $t_c$  are the critical current density and time at which microphysics kinetic instabilities are triggered, and  $H$  is the Heaviside step function. The normalization constant for  $J_c$  is  $J_0 = B_0 / \mu_0 L = 1.4 \times 10^7 \text{ A m}^{-2}$ . Using the Caltech jet parameters where 6 keV X-rays are observed [94] in association with RTI we assume an electron is accelerated to 6 keV in 1 cm. This implies the existence of a localized parallel electric field  $E_{\parallel} = 6 \times 10^5 \text{ V m}^{-1}$ . We choose  $J_c = 15$  and  $t_c = 1.2$  so that the large resistivity is turned on at the same time and locations as the reconnection event in the experiment. This defines  $\eta_a \equiv E_{\parallel} / J_c$  and implies  $S_a = 1.0$ . In addition to a  $J$ -dependent factor, a time-dependent factor is included to properly trigger the reconnection due to the discrepancy between the boundary conditions in the simulation and experiment.

### Particle Simulation

The trajectory of test electrons is calculated using a snapshot of the MHD simulation with a localized parallel electric field provided by the anomalous resistivity. Figure 9.5 shows the contour of the parallel electric field  $E_{\parallel} = \eta \mathbf{J} \cdot \mathbf{B} / B$ . The guiding center approximation [105] is used to describe the test electron motion.

$$\frac{du_{\parallel}}{dt} = \frac{q}{m}E_{\parallel} - \frac{\mu}{mB}(\mathbf{B} \cdot \nabla)B, \quad (9.10)$$

$$\frac{d\mathbf{r}}{dt} = \frac{u_{\parallel}}{B}\mathbf{B} + \frac{\mathbf{E} \times \mathbf{B}}{B^2} + \frac{\mu}{qB^2}\mathbf{B} \times \nabla B + \frac{mu_{\parallel}^2}{qB^4}\mathbf{B} \times (\mathbf{B} \cdot \nabla)\mathbf{B}, \quad (9.11)$$

where  $\mu = mu_{\perp}^2/2B = \text{constant}$ . The parallel electric field is generated at the location of high current density where the anomalous resistivity is turned on via Equation 9.9. From the simulation, we measure  $E_{\parallel} = 6 \times 10^5 \text{ V m}^{-1}$ . The electrons have initial thermal speed  $v_T = \sqrt{2kT/m_e}$ . For  $\kappa T = 2 \text{ eV}$ ,  $n = 10^{23} \text{ m}^{-3}$ ,  $m_i = 40 \text{ u}$ ,  $B_0 = 1.9 \text{ T}$ ,  $v_T/v_A = \sqrt{2\kappa T\mu_0 m_i n_i/m_e}/B_0 = 40$ . The initial pitch angles are chosen at random and the initial positions are  $(x_p, y_p, z_p)$ . The 1000 particles are randomly placed inside a cube defined by  $-0.2 \leq x_p \leq 0.0$ ,  $-0.4 \leq y_p \leq -0.2$ ,  $-0.5 \leq z_p \leq -0.3$ ; this cube is shown by black lines in Figure 9.5a.

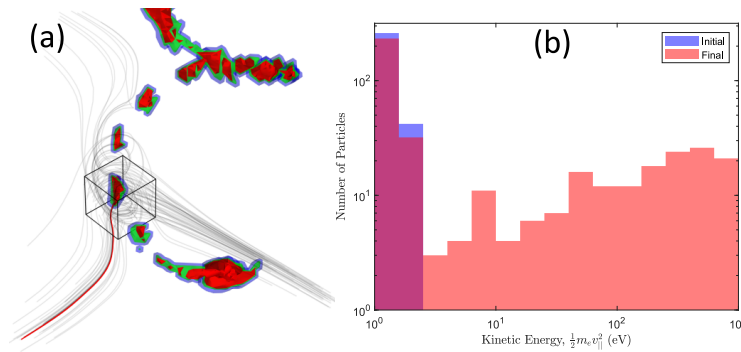


Figure 9.5: (a) Isosurfaces of  $E_{\parallel} = \eta \mathbf{J} \cdot \mathbf{B} / B$ . The color {green, blue, red} represents the level {0.1, 0.4, 0.6} of the maximum value of this time step respectively. The gray lines show 100 random particle trajectories. The red lines show the trajectory of the highly accelerated particles. The cube indicates the domain of the initial position. (b) Distribution of the test particles initial and final energies.

The red lines in Figure 9.5a show the trajectory of particles that are accelerated to high energy on passing through the large resistive region. The other non-accelerated particles are indicated by gray lines. The particle energy distribution, shown in Figure 9.5b, indicates that 10% of the particles are accelerated to energy above 1 keV. The largest energy observed is 2.3 keV. With  $E_{\parallel} = 6 \times 10^5 \text{ V m}^{-1}$  and  $\delta = 0.4 \text{ cm}$ , the observed electron final kinetic energy agrees with our expected energy, i.e.  $\Delta K = E_{\parallel} \delta = 2.4 \text{ keV}$ . While highly simplified, this particle simulation nevertheless indicates that high energy X-rays could come from the electric field generated by the KDRT-induced magnetic reconnection; it thus gives insight into the acceleration

process creating high energy electrons. This description of the electron acceleration process is very simplified and macroscopic; a more physically realistic description that takes into account changes in collisionality of electrons as they accelerate was given in Marshall and Bellan [93].

## 9.6 Discussion

There was an uncertainty regarding the actual jet radius at the time and location of the RTI in the Caltech jet experiment. In the past [167], the actual magnetic radii of the jets are believed to be larger than the visible images shown in Figure 9.1 ( $a \sim 3\text{-}5$  cm). However, the result of the 3D simulation here suggests that the jet radius might be closer to the observed radius from the visible light emission than we previously thought. For a plasma jet with an azimuthal magnetic field  $B_\theta = 1.9$  T and a minor radius  $a = 1$  cm, the corresponding axial current is  $I = 2\pi a B_\theta / \mu_0 = 95$  kA. For this same shot, Moser and Bellan [98] reported a consistent peak current of  $I = 110$  kA. Furthermore, a recent study of magnetic RTI by Zhang, Wongwaitayakornkul, and Bellan [169] on the arched plasma loop experiment with similar parameters ( $a, \lambda_{\text{RT}} = 1$  cm and  $\kappa T = 2$  eV) also supports that the expected minor radius is close to the observation from the images,  $a \sim 1$  cm. In that study, the wavelength of the observed magnetic RTI depends on the axial magnetic field. The RTI from that experiment is driven from a lateral acceleration, which is a special case of KDRT with  $B_z \gg B_\theta$ . The kink instability grows such that  $\mathbf{k} \cdot \mathbf{B} = 0$  and hence the lateral acceleration in Zhang, Wongwaitayakornkul, and Bellan [169] corresponds to the mode with small  $k_z$  or long axial wavelength  $\lambda_{z,\text{kink}}$ . The accurate jet radius will be important for the future study of this phenomenon; conversely, by understanding its physical mechanism, knowing plasma dynamics and density allows us to estimate the plasma jet radius.

Many models of the solar corona are based on the zero- $\beta$  approximation and yet describe the corona in terms of the evolution of reconnecting magnetic fields. A zero- $\beta$  code is only able to capture the current-driven instability but not the pressure-driven one. Although a path to the reconnection scale by only current-driven instability exists, it disregards the possibility of fast reconnection due to pressure-driven instability. For example, Seo et al. [121] observed a cascade progression sequence from sausage-like pinching to KI that leads to fast reconnection in a different regime of the same Caltech jet experiment. In order to take into account the possible role that KDRT might play in fast reconnection and particle energization in the solar corona, it would be necessary to extend the reconnection model to

include finite- $\beta$ , collimation physics with associated paramagnetism, the  $d_i$  scale, and anomalous resistivity associated with localized high current density.

In summary, the experimentally observed cascade of instabilities from KI to RTI was simulated using a resistive MHD code. We found that (1) spatial localization (paramagnetism) of  $B_z$  is crucial to achieve the KDRT, (2) the dependence on  $\Phi^2$  given in Zhai and Bellan [166] was verified, and (3) electrons can be accelerated to high energy through this process.

*Chapter 10*

## SUMMARY

In this thesis, we studied several mechanisms exhibited by an arched plasma-filled magnetically-twisted current-carrying flux rope. The investigation is done with laboratory experiments and numerical simulations. The scalability property of MHD plasmas allow us to compare these phenomenon with observations on the sun. Chapter 2 describes the relevant experiments and the diagnostics. Chapter 3 explains the numerical simulation setup, initial conditions, and the injection routine. Chapter 4 outlines the characterization of the apex dip on the experimental flux rope. Chapter 5 depicts the density cavity from current injection. As a result of cavity formation by the reverse current layer, Chapter 6 shows that this current layer drives a plasma perturbation that could steepen into a shock. In the following few chapters, observations of MHD instabilities are described. Chapter 7 displays the observation of the magnetic Rayleigh-Taylor instability observed on the single loop experiment. Chapter 8 demonstrates the progression of sausage-to-kink instability via the simulation. Chapter 9 reports the simulation of kink-driven Rayleigh-Taylor instability, leading to fast magnetic reconnection.

**10.1 Future Direction**

We have investigated the dynamics of the arched magnetically-twisted flux rope and learned its mechanism for the formation of dip, cavity, shock, and instability. The following sections provide some ideas that could be further examined.

**Deflected Flux Rope**

The single loop experiment is equipped with solenoids inside the vacuum chamber for applying a localized strapping magnetic field. In the past experiment by Ha and Bellan [46], a strapping field is shown to slow down a part of the flux rope. Since the solenoids could be moved around the mounting relatively easily, it would be interesting to see the effect of the localized strapping field on the dynamic and morphology of the flux rope. A preliminary result is briefly described in App. B. The study of rotation and deflection of CMEs is a subject of interest in the solar physics community because incident CMEs play a significant role in the prediction of space weather [66–69].

### **Model for Initial Current Density**

A more detail measurement and numerical simulation gives us a better understanding of the dynamics of the arched flux rope. In Chapter 4, the model for initial neutral density is developed and is supported by observations. The numerical simulation uses an ad-hoc current profile with equal spacing as an initial current density profile. This current profile accurately mimics macro-dynamics of the flux rope, but fails to reproduce micro-dynamics. A more precise approach would be to calculate the initial current density from the plasma breakdown condition, i.e., Paschen's law [79]. Given a known boundary (electrodes' voltage), an electric field could be calculated everywhere inside the chamber. Given the initial neutral density, the current density can then be deduced from the Paschen's law. Accurate knowledge for the initial current path would be useful for understanding the plasma microscopic dynamics and designing future plasma pulse experiments.

### **Numerical Simulation for MHD Instability-Driven Magnetic Reconnection with Extended Physics**

The importance of MHD instabilities on the fast magnetic reconnection mechanism is evident as illustrated in Chapters 7 — 9. However, so far the previous numerical simulations performed in this dissertation are all MHD simulations. The experimentally observed magnetic reconnection event occurs at a much faster timescale than the resistive MHD reconnection theory could predict. To capture the kinetic effect properly, one could extend the physical model to include the Hall term,  $-\mathbf{J} \times \mathbf{B}/n_e e$ , in the MHD equation or use particle-in-cell simulations. The connection between these micro-instabilities and the macro-instabilities (MHD) will give us insight into the magnetic reconnection and mechanism for particle acceleration.

## BIBLIOGRAPHY

- [1] S K Antiochos, P J MacNeice, and D S Spicer. “The Thermal Nonequilibrium of Prominences”. In: *The Astrophysical Journal* 536.1 (2000), p. 494. URL: <http://stacks.iop.org/0004-637X/536/i=1/a=494>.
- [2] NADIR Arber, HANINA Hibshoosh, STEVEN F Moss, THOMAS Sutter, Y Zhang, MELISSA Begg, SHAOBAI Wang, I BERNARD Weinstein, and PETER R Holt. “Increased expression of cyclin D1 is an early event in multistage colorectal carcinogenesis”. In: *Gastroenterology* 110.3 (1996), pp. 669–674.
- [3] L Arnold, J Dreher, R Grauer, H Soltwisch, and H Stein. “Three-dimensional magnetohydrodynamical simulation of expanding magnetic flux ropes”. In: *Physics of Plasmas* 15.4 (2008), p. 42106. DOI: [10.1063/1.2903904](https://doi.org/10.1063/1.2903904).
- [4] I Arregui and R Soler. “Model comparison for the density structure along solar prominence threads”. In: *Astronomy and Astrophysics* 578 (June 2015), A130. DOI: [10.1051/0004-6361/201525720](https://doi.org/10.1051/0004-6361/201525720). arXiv: [1505.03448](https://arxiv.org/abs/1505.03448) [[astro-ph.SR](https://arxiv.org/abs/1505.03448)].
- [5] G. D. R. Attrill, L. K. Harra, L van Driel-Gesztelyi, and P Démoulin. “Coronal “Wave”: Magnetic Footprint of a Coronal Mass Ejection?” In: *The Astrophysical Journal Letters* 656 (Feb. 2007), pp. L101–L104. DOI: [10.1086/512854](https://doi.org/10.1086/512854).
- [6] T. S. Bastian, M Pick, A Kerdraon, D Maia, and A Vourlidas. “The Coronal Mass Ejection of 1998 April 20: Direct Imaging at Radio Wavelengths”. In: *The Astrophysical Journal Letters* 558 (Sept. 2001), pp. L65–L69. DOI: [10.1086/323421](https://doi.org/10.1086/323421).
- [7] P M Bellan. “Why current-carrying magnetic flux tubes gobble up plasma and become thin as a result”. In: *Phys. Plasma* 10.5 (2003), pp. 1999–2008.
- [8] P M Bellan and J F Hansen. “Laboratory simulations of solar prominence eruptions”. In: *Physics of Plasmas* 5.5 (1998), pp. 1991–2000. DOI: [10.1063/1.872870](https://doi.org/10.1063/1.872870).
- [9] Paul M Bellan. “Experiments and models of MHD jets and their relevance to astrophysics and solar physics”. In: *Physics of Plasmas* 25.5 (2018), p. 055601.
- [10] Paul M Bellan. “Experiments relevant to astrophysical jets”. In: *Journal of Plasma Physics* 84.5 (2018).
- [11] Paul M Bellan. “Fast, purely growing collisionless reconnection as an eigenfunction problem related to but not involving linear whistler waves”. In: *Physics of Plasmas* 21.10 (2014), p. 102108.
- [12] Paul M Bellan. *Fundamentals of plasma physics*. Cambridge University Press, 2008.

- [13] Paul M Bellan, Sethivoine You, and Scott C Hsu. “Simulating astrophysical jets in laboratory experiments”. In: *High Energy Density Laboratory Astrophysics*. Springer, 2005, pp. 203–209.
- [14] Thomas E Berger, Gregory Slater, Neal Hurlburt, Richard Shine, Theodore Tarbell, Bruce W Lites, Takenori J Okamoto, Kiyoshi Ichimoto, Yukio Katsukawa, Tetsuya Magara, et al. “Quiescent prominence dynamics observed with the Hinode solar optical telescope. I. Turbulent upflow plumes”. In: *The Astrophysical Journal* 716.2 (2010), p. 1288.
- [15] W F Bergerson, C B Forest, Gennady Fiksel, D A Hannum, R Kendrick, J S Sarff, and Sam Stambler. “Onset and saturation of the kink instability in a current-carrying line-tied plasma”. In: *Physical review letters* 96.1 (2006), p. 15004.
- [16] Ira B Bernstein, E A Frieman, Martin David Kruskal, and R M Kulsrud. “An energy principle for hydromagnetic stability problems”. In: *Proceedings of the Royal Society of London. Series A. Mathematical and Physical Sciences* 244.1236 (1958), pp. 17–40.
- [17] R Betti, VN Goncharov, RL McCrory, and CP Verdon. “Growth rates of the ablative Rayleigh–Taylor instability in inertial confinement fusion”. In: *Physics of Plasmas* 5.5 (1998), pp. 1446–1454.
- [18] D A Biesecker, D C Myers, B J Thompson, D M Hammer, and A Vourlidas. “Solar phenomena associated with “{EIT} waves””. In: *The Astrophysical Journal* 569.2 (2002), p. 1009.
- [19] Philippe-A Bourdin. “Plasma Beta Stratification in the Solar Atmosphere: A Possible Explanation for the Penumbra Formation”. In: *arXiv preprint arXiv:1711.10965* (2017).
- [20] Jörg Büchner and Nina Elkina. “Anomalous resistivity of current-driven isothermal plasmas due to phase space structuring”. In: *Physics of plasmas* 13.8 (2006), p. 82304.
- [21] Eoin P Carley, David M Long, Jason P Byrne, Pietro Zucca, D Shaun Bloomfield, Joseph McCauley, and Peter T Gallagher. “Quasiperiodic acceleration of electrons by a plasmoid-driven shock in the solar atmosphere”. In: *Nature Physics* 9.12 (2013), p. 811.
- [22] Jack Carlyle, David R Williams, Lidia van Driel-Gesztelyi, Davina Innes, Andrew Hillier, and Sarah Matthews. “Investigating the dynamics and density evolution of returning plasma blobs from the 2011 June 7 eruption”. In: *The Astrophysical Journal* 782.2 (2014), p. 87.
- [23] Kil-Byoung Chai, Xiang Zhai, and Paul M Bellan. “Extreme ultra-violet burst, particle heating, and whistler wave emission in fast magnetic reconnection induced by kink-driven Rayleigh-Taylor instability”. In: *Physics of Plasmas* 23.3 (2016), p. 32122.

- [24] J Chen, C Marqué, A Vourlidas, J Krall, and P W Schuck. “The Flux-Rope Scaling of the Acceleration of Coronal Mass Ejections and Eruptive Prominences”. In: *The Astrophysical Journal* 649.1 (2006), p. 452. URL: <http://stacks.iop.org/0004-637X/649/i=1/a=452>.
- [25] James Chen. “Physics of erupting solar flux ropes: Coronal mass ejections (CMEs)—Recent advances in theory and observation”. In: *Physics of Plasmas* 24.9 (2017), p. 90501. DOI: [10.1063/1.4993929](https://doi.org/10.1063/1.4993929).
- [26] P F Chen. “Coronal Mass Ejections: Models and Their Observational Basis”. In: *Living Reviews in Solar Physics* 8.1 (Apr. 2011), p. 1. ISSN: 1614-4961. DOI: [10.12942/lrsp-2011-1](https://doi.org/10.12942/lrsp-2011-1).
- [27] P F Chen, S T Wu, K Shibata, and C Fang. “Evidence of EIT and Moreton waves in numerical simulations”. In: *The Astrophysical Journal Letters* 572.1 (2002), p. L99. DOI: [10.1086/341486](https://doi.org/10.1086/341486).
- [28] P.F. Chen and C Fang. “{EIT} waves and coronal mass ejections”. In: *Astronomical Society of India Conference Series*. Vol. 2. Astronomical Society of India Conference Series. 2011. arXiv: [1108.5274](https://arxiv.org/abs/1108.5274) [astro-ph.SR].
- [29] X Cheng, J Zhang, O Olmedo, A Vourlidas, M D Ding, and Y Liu. “Investigation of the Formation and Separation of an Extreme-ultraviolet Wave from the Expansion of a Coronal Mass Ejection”. In: *The Astrophysical Journal Letters* 745.1 (2012), p. L5. URL: <http://stacks.iop.org/2041-8205/745/i=1/a=L5>.
- [30] Ofer Cohen, Gemma D R Attrill, Ward B Manchester IV, and Meredith J Wills-Davey. “Numerical Simulation of an EUV Coronal Wave Based on the 2009 February 13 CME Event Observed by STEREO”. In: *The Astrophysical Journal* 705.1 (2009), p. 587. URL: <http://stacks.iop.org/0004-637X/705/i=1/a=587>.
- [31] C D Cothran, A Falk, A Fefferman, M Landreman, M R Brown, and M J Schaffer. “Spheromak merging and field reversed configuration formation at the Swarthmore Spheromak Experiment”. In: *Physics of Plasmas* 10.5 (2003), pp. 1748–1754.
- [32] C Delannée, T Török, G Aulanier, and J.-F. Hochedez. “A New Model for Propagating Parts of EIT Waves: A Current Shell in a CME”. In: *Solar Physics* 247.1 (Jan. 2008), pp. 123–150. ISSN: 1573-093X. DOI: [10.1007/s11207-007-9085-4](https://doi.org/10.1007/s11207-007-9085-4).
- [33] Brian R Dennis, Anne K Tolbert, Andrew Inglis, Jack Ireland, Tongjiang Wang, Gordon D Holman, Laura A Hayes, and Peter T Gallagher. “Detection and interpretation of long-lived X-ray quasi-periodic pulsations in the X-class solar flare on 2013 May 14”. In: *The Astrophysical Journal* 836.1 (2017), p. 84.

- [34] Cooper Downs, Ilia I Roussev, Bart van der Holst, Noé Lugaz, Igor V Sokolov, and Tamas I Gombosi. “Studying Extreme Ultraviolet Wave Transients with a Digital Laboratory: Direct Comparison of Extreme Ultraviolet Wave Observations to Global Magnetohydrodynamic Simulations”. In: *The Astrophysical Journal* 728.1 (2011), p. 2. URL: <http://stacks.iop.org/0004-637X/728/i=1/a=2>.
- [35] J F Drake, M A Shay, and M Swisdak. “The Hall fields and fast magnetic reconnection”. In: *Physics of plasmas* 15.4 (2008), p. 42306.
- [36] Gregory L Eyink, Alex Lazarian, and Ethan T Vishniac. “Fast magnetic reconnection and spontaneous stochasticity”. In: *The Astrophysical Journal* 743.1 (2011), p. 51.
- [37] Richard Fitzpatrick. *Plasma physics: an introduction*. Crc Press, 2014.
- [38] T G Forbes, J A Linker, J Chen, C Cid, J Kóta, M A Lee, G Mann, Z Mikić, M S Potgieter, J M Schmidt, G L Siscoe, R Vainio, S K Antiochos, and P Riley. “{CME} Theory and Models”. In: *Space Science Reviews* 123.1 (Mar. 2006), pp. 251–302. ISSN: 1572-9672. DOI: [10.1007/s11214-006-9019-8](https://doi.org/10.1007/s11214-006-9019-8). URL: <https://doi.org/10.1007/s11214-006-9019-8>.
- [39] Harold P Furth, John Killeen, and Marshall N Rosenbluth. “Finite-resistivity instabilities of a sheet pinch”. In: *The physics of Fluids* 6.4 (1963), pp. 459–484.
- [40] G Allen Gary. “Plasma beta above a solar active region: Rethinking the paradigm”. In: *Solar Physics* 203.1 (2001), pp. 71–86.
- [41] Sarah Gibson. “Coronal Cavities: Observations and Implications for the Magnetic Environment of Prominences”. In: *Solar Prominences*. Cham: Springer International Publishing, 2015, pp. 323–353. ISBN: 978-3-319-10416-4. DOI: [10.1007/978-3-319-10416-4\\_13](https://doi.org/10.1007/978-3-319-10416-4_13).
- [42] Hans Goedbloed, Rony Keppens, and Stefaan Poedts. *Magnetohydrodynamics: Of Laboratory and Astrophysical Plasmas*. Cambridge University Press, 2019.
- [43] N Gopalswamy and B J Thompson. “Early life of coronal mass ejections”. In: *Journal of Atmospheric and Solar-Terrestrial Physics* 62.16 (2000), pp. 1457–1469.
- [44] Carl Greifinger and Julian D Cole. “On Cylindrical Magnetohydrodynamic Shock Waves”. In: *The Physics of Fluids* 4.5 (1961), pp. 527–534. DOI: [10.1063/1.1706358](https://doi.org/10.1063/1.1706358).
- [45] S Gunár, D.~H. Mackay, U Anzer, and P Heinzel. “Non-linear force-free magnetic dip models of quiescent prominence fine structures”. In: *Astronomy and Astrophysics* 551 (Mar. 2013), A3. DOI: [10.1051/0004-6361/201220597](https://doi.org/10.1051/0004-6361/201220597).

- [46] Bao N Ha and Paul M Bellan. “Laboratory demonstration of slow rise to fast acceleration of arched magnetic flux ropes”. In: *Geophysical Research Letters* 43.18 (2016), pp. 9390–9396. ISSN: 1944-8007. DOI: [10 . 1002 / 2016GL069744](https://doi.org/10.1002/2016GL069744).
- [47] Izumi Hachisu, Takuya Matsuda, Ken’ichi Nomoto, and Toshikazu Shigeyama. “Mixing in ejecta of supernovae. I-General properties of two-dimensional Rayleigh-Taylor instabilities and mixing width in ejecta of supernovae”. In: *The Astrophysical Journal* 390 (1992), pp. 230–252.
- [48] J F Hansen, S K P Tripathi, and P M Bellan. “Co- and counter-helicity interaction between two adjacent laboratory prominences”. In: *Physics of Plasmas* 11.6 (2004), pp. 3177–3185. DOI: [10 . 1063 / 1 . 1724831](https://doi.org/10.1063/1.1724831). URL: <http://dx.doi.org/10.1063/1.1724831>.
- [49] J Freddy Hansen and Paul M Bellan. “Experimental Demonstration of How Strapping Fields Can Inhibit Solar Prominence Eruptions”. In: *The Astrophysical Journal Letters* 563.2 (2001), p. L183. DOI: [10 . 1086/338736](https://doi.org/10.1086/338736). URL: <http://stacks.iop.org/1538-4357/563/i=2/a=L183>.
- [50] Takayuki Haruki, Hamid Reza Yousefi, Katsumi Masugata, Jun-Ichi Sakai, Yusuke Mizuguchi, Nao Makino, and Hiroaki Ito. “Simulation of high-energy particle production through sausage and kink instabilities in pinched plasma discharges”. In: *Physics of plasmas* 13.8 (2006), p. 82106.
- [51] Magnus A Haw and Paul M Bellan. “MHD Collimation Mechanism in Arched Flux Ropes Characterized Using Volumetric, Time-Dependent B-Vector Measurements”. In: *Geophysical Research Letters* 44.19 (2017), pp. 9525–9531.
- [52] Magnus A Haw, Byonghoon Seo, and Paul M Bellan. “Laboratory measurement of large-amplitude whistler pulses generated by fast magnetic reconnection”. In: *Geophysical Research Letters* 46.13 (2019), pp. 7105–7112.
- [53] Magnus A Haw, Pakorn Wongwaitayakornkul, Hui Li, and Paul M Bellan. “Reverse Current Model for Coronal Mass Ejection Cavity Formation”. In: *The Astrophysical Journal Letters* 862.2 (2018), p. L15.
- [54] P Heinzel and U Anzer. “Magnetic Dips in Prominences”. In: *Solar Physics* 184.1 (1999), pp. 103–111. ISSN: 1573-093X. DOI: [10 . 1023 / A : 1005098704665](https://doi.org/10.1023/A:1005098704665).
- [55] J Jeff Hester, James M Stone, Paul A Scowen, Byung-II Jun, John S Gallagher III, Michael L Norman, Gilda E Ballester, Christopher J Burrows, Stefano Casertano, John T Clarke, et al. “WFPC2 studies of the Crab Nebula. III. Magnetic Rayleigh-Taylor instabilities and the origin of the filaments”. In: *Astrophysical Journal* 456.1 (1996), pp. 225–233.
- [56] Andrew Hillier. “The magnetic Rayleigh–Taylor instability in solar prominences”. In: *Reviews of Modern Plasma Physics* 2.1 (2018), p. 1.

- [57] Andrew Hillier, Thomas Berger, Hiroaki Isobe, and Kazunari Shibata. “Numerical simulations of the magnetic Rayleigh-Taylor instability in the Kippenhahn-Schlüter prominence model. I. Formation of upflows”. In: *The Astrophysical Journal* 746.2 (2012), p. 120.
- [58] Alan Lowell Hoffman. “Magnetohydrodynamic shock production and current sheet diffusion”. PhD thesis. Caltech, 1967. URL: <http://resolver.caltech.edu/CaltechETD:etd-12292005-135853>.
- [59] Scott C Hsu and Paul M Bellan. “Experimental identification of the kink instability as a poloidal flux amplification mechanism for coaxial gun spheromak formation”. In: *Physical review letters* 90.21 (2003), p. 215002.
- [60] Satoshi Inoue. “Magnetohydrodynamics modeling of coronal magnetic field and solar eruptions based on the photospheric magnetic field”. In: *Progress in Earth and Planetary Science* 3.1 (2016), p. 19. ISSN: 2197-4284. DOI: [10.1186/s40645-016-0084-7](https://doi.org/10.1186/s40645-016-0084-7).
- [61] T R Jarboe, I Henins, A R Sherwood, Cris W Barnes, and H W Hoida. “Slow formation and sustainment of spheromaks by a coaxial magnetized plasma source”. In: *Physical review letters* 51.1 (1983), p. 39.
- [62] Chaowei Jiang, S T Wu, Xueshang Feng, and Qiang Hu. “Formation and Eruption of an Active Region Sigmoid. I. A Study by Nonlinear Force-free Field Modeling”. In: *The Astrophysical Journal* 780.1 (2014), p. 55. URL: <http://stacks.iop.org/0004-637X/780/i=1/a=55>.
- [63] M Jin, W B Manchester, B van der Holst, I Sokolov, G Tóth, A Vourlidas, C A de Koning, and T I Gombosi. “Chromosphere to 1 AU Simulation of the 2011 March 7th Event: A Comprehensive Study of Coronal Mass Ejection Propagation”. In: *The Astrophysical Journal* 834.2 (2017), p. 172. DOI: [10.3847/1538-4357/834/2/172](https://doi.org/10.3847/1538-4357/834/2/172).
- [64] A Al-Karkhy, P K Browning, G Cunningham, S J Gee, and M G Rusbridge. “Observations of the magnetohydrodynamic dynamo effect in a spheromak plasma”. In: *Physical review letters* 70.12 (1993), p. 1814.
- [65] M Karlický, M Bárta, M Karlický, and M Bárta. “Fragmentation of the current sheet, anomalous resistivity, and acceleration of particles”. In: *Solar Physics* 247.2 (2008), pp. 335–342.
- [66] C Kay, LFG Dos Santos, and M Opher. “Constraining the masses and the non-radial drag coefficient of a solar coronal mass ejection”. In: *The Astrophysical Journal Letters* 801.2 (2015), p. L21.
- [67] C Kay, M Opher, and RM Evans. “Global trends of CME deflections based on CME and solar parameters”. In: *The Astrophysical Journal* 805.2 (2015), p. 168.

- [68] Christina Kay, Nat Gopalswamy, Hong Xie, and Seiji Yashiro. “Deflection and rotation of CMEs from Active region 11158”. In: *Solar Physics* 292.6 (2017), p. 78.
- [69] Christina Kay, Merav Opher, and Rebekah M Evans. “Forecasting a coronal mass ejection’s altered trajectory: ForeCAT”. In: *The Astrophysical Journal* 775.1 (2013), p. 5.
- [70] Rony Keppens, Chun Xia, and Oliver Porth. “Solar prominences: “Double, Double. . . Boil and Bubble””. In: *The Astrophysical Journal Letters* 806.1 (2015), p. L13.
- [71] A Klassen, H Aurass, G Mann, and B J Thompson. “Catalogue of the 1997 {SOHO–EIT} coronal transient waves and associated type {II} radio burst spectra”. In: *Astronomy and Astrophysics Supplement Series* 141.3 (2000), pp. 357–369.
- [72] J A Klimchuk. “Cross-sectional properties of coronal loops”. In: *Physics of the Solar Corona and Transition Region*. Springer, 2001, pp. 53–75.
- [73] K A Kozarev, K E Korreck, V V Lobzin, M A Weber, and N A Schwadron. “Off-limb Solar Coronal Wavefronts from SDO/AIA Extreme-ultraviolet Observations–Implications for Particle Production”. In: *The Astrophysical Journal Letters* 733.2 (2011), p. L25. URL: <http://stacks.iop.org/2041-8205/733/i=2/a=L25>.
- [74] Martin David Kruskal and Martin Schwarzschild. “Some instabilities of a completely ionized plasma”. In: *Proceedings of the Royal Society of London. Series A. Mathematical and Physical Sciences* 223.1154 (1954), pp. 348–360.
- [75] Martin David Kruskal and Martin Schwarzschild. “Some instabilities of a completely ionized plasma”. In: *Proceedings of the Royal Society of London. Series A. Mathematical and Physical Sciences* 223.1154 (1954), pp. 348–360.
- [76] Deepak Kumar and Paul M Bellan. “Nonequilibrium Alfvénic plasma jets associated with spheromak formation”. In: *Physical review letters* 103.10 (2009), p. 105003.
- [77] N Labrosse, P Heinzel, J.-C. Vial, T Kucera, S Parenti, S Gunár, B Schmieder, and G Kilper. “Physics of Solar Prominences: I- Spectral Diagnostics and Non-LTE Modelling”. In: *Space Science Review* 151 (Apr. 2010), pp. 243–332. DOI: [10.1007/s11214-010-9630-6](https://doi.org/10.1007/s11214-010-9630-6).
- [78] L D Landau and E M Lifshitz. *Course of theoretical physics. vol. 6: Fluid mechanics*. London, 1959.
- [79] Min Uk Lee, Jimo Lee, Jae Koo Lee, and Gunsu S Yun. “Extended scaling and Paschen law for micro-sized radiofrequency plasma breakdown”. In: *Plasma Sources Science and Technology* 26.3 (2017), p. 034003.
- [80] S Li and H Li. *Los Alamos National Lab*. Tech. rep. LA-UR-03-8935, 2003.

- [81] X B Li and R C Cross. “Measurement of plasma diamagnetism by a coil located inside a conducting wall”. In: *Review of scientific instruments* 65.8 (1994), pp. 2623–2626.
- [82] Jens von der Linden and Setthivoine You. “Sausage instabilities on top of kinking lengthening current-carrying magnetic flux tubes”. In: *Physics of Plasmas* 24.5 (2017), p. 52105.
- [83] Wei Liu, Nariaki V Nitta, Carolus J Schrijver, Alan M Title, and Theodore D Tarbell. “First SDO AIA Observations of a Global Coronal EUV “Wave”: Multiple Components and “Ripples””. In: *The Astrophysical Journal Letters* 723.1 (2010), p. L53. URL: <http://stacks.iop.org/2041-8205/723/i=1/a=L53>.
- [84] Keith T K Loebner, Thomas C Underwood, and Mark A Cappelli. “A fast rise-rate, adjustable-mass-bit gas puff valve for energetic pulsed plasma experiments”. In: *Review of Scientific Instruments* 86.6 (2015), p. 63503. DOI: [10.1063/1.4922522](https://doi.org/10.1063/1.4922522).
- [85] David M Long, Deborah Baker, David R Williams, Eoin P Carley, Peter T Gallagher, and Pietro Zucca. “The energetics of a global shock wave in the low solar corona”. In: *The Astrophysical Journal* 799.2 (2015), p. 224.
- [86] D.~M. Long, D.~S. Bloomfield, P.~F. Chen, C Downs, P.~T. Gallagher, R.-Y. Kwon, K Vanninathan, A.~M. Veronig, A Vourlidas, B Vršnak, A Warmuth, and T Žic. “Understanding the Physical Nature of Coronal “EIT Waves””. In: *Solar Physics* 292 (Jan. 2017), p. 7. DOI: [10.1007/s11207-016-1030-y](https://doi.org/10.1007/s11207-016-1030-y).
- [87] B J Lynch, S K Antiochos, P J MacNeice, T H Zurbuchen, and L A Fisk. “Observable Properties of the Breakout Model for Coronal Mass Ejections”. In: *The Astrophysical Journal* 617.1 (2004), p. 589. DOI: [10.1086/424564](https://doi.org/10.1086/424564).
- [88] Suli Ma, John C Raymond, Leon Golub, Jun Lin, Huadong Chen, Paolo Grigis, Paola Testa, and David Long. “Observations and Interpretation of a Low Coronal Shock Wave Observed in the {EUV} by the {SDO/AIA}”. In: *The Astrophysical Journal* 738.2 (2011), p. 160. URL: <http://stacks.iop.org/0004-637X/738/i=2/a=160>.
- [89] Mackel. “Dynamic behaviour of magnetic flux tubes in laboratory simulations of solar flares”. PhD thesis. Ruhr-Universität Bochum, 2014.
- [90] F Mackel, S Ridder, J Tenfelde, T Tacke, and H Soltwisch. “Evolution of plasma loops in a semi-toroidal pinch experiment”. In: *Physics of Plasmas* 22.4 (2015), p. 42502.
- [91] D.~J.~F. Maia, R Gama, C Mercier, M Pick, A Kerdraon, and M Karlický. “The Radio-Coronal Mass Ejection Event on 2001 April 15”. In: *The Astrophysical Journal* 660 (May 2007), pp. 874–881. DOI: [10.1086/508011](https://doi.org/10.1086/508011).
- [92] Gottfried Mann. “Simple magnetohydrodynamic waves”. In: *Journal of plasma physics* 53.1 (1995), pp. 109–125.

- [93] R S Marshall and P M Bellan. “Acceleration of charged particles to extremely large energies by a sub-Dreicer electric field”. In: *Physics of Plasmas* 26.4 (2019), p. 42102.
- [94] R S Marshall, M J Flynn, and P M Bellan. “Hard x-ray bursts observed in association with Rayleigh-Taylor instigated current disruption in a solar-relevant lab experiment”. In: *Physics of Plasmas* 25.11 (2018), p. 112101.
- [95] H S McLean, S Woodruff, E B Hooper, R H Bulmer, D N Hill, C Holcomb, J Moller, B W Stallard, R D Wood, and Z Wang. “Suppression of MHD fluctuations leading to improved confinement in a gun-driven spheromak”. In: *Physical review letters* 88.12 (2002), p. 125004.
- [96] María M Milanese, Jorge O Pouzo, Osvaldo D Cortázar, and Roberto L Moroso. “Fast valve and nozzle for gas-puff operation of dense plasma focus”. In: *Review of Scientific Instruments* 77.3 (2006), p. 36106. DOI: [10.1063/1.2169535](https://doi.org/10.1063/1.2169535).
- [97] Auna L Moser. “Dynamics of magnetically driven plasma jets: An instability of an instability, gas cloud impacts, shocks, and other deformations”. PhD thesis. Caltech, 2012.
- [98] Auna L Moser and Paul M Bellan. “Magnetic reconnection from a multiscale instability cascade”. In: *Nature* 482.7385 (2012), p. 379.
- [99] N Muhr, A M Veronig, I W Kienreich, B Vršnak, M Temmer, and B M Bein. “Statistical Analysis of Large-Scale EUV Waves Observed by STEREO/EUVI”. In: *Solar Physics* 289.12 (Dec. 2014), pp. 4563–4588. ISSN: 1573-093X. DOI: [10.1007/s11207-014-0594-7](https://doi.org/10.1007/s11207-014-0594-7).
- [100] Nicole Muhr, A M Veronig, I W Kienreich, Manuela Temmer, and Bojan Vršnak. “Analysis of characteristic parameters of large-scale coronal waves observed by the Solar-Terrestrial Relations Observatory/Extreme Ultraviolet Imager”. In: *The Astrophysical Journal* 739.2 (2011), p. 89.
- [101] C. E. Myers, M Yamada, H Ji, J Yoo, J Jara-Almonte, and W Fox. “Laboratory study of low- $\beta$  forces in arched, line-tied magnetic flux ropes”. In: *Physics of Plasmas* 23.11 (Nov. 2016), p. 112102. DOI: [10.1063/1.4966691](https://doi.org/10.1063/1.4966691).
- [102] M Nagata, T Kanki, T Masuda, S Naito, H Tatsumi, and T Uyama. “Relaxation oscillations and toroidal-current regeneration in a helicity-driven spheromak”. In: *Physical review letters* 71.26 (1993), p. 4342.
- [103] M Nakamura, Y Uchida, and S Hirose. “Production of wiggled structure of AGN radio jets in the sweeping magnetic twist mechanism”. In: *New Astronomy* 6.2 (2001), pp. 61–78. ISSN: 1384-1076. DOI: [http://dx.doi.org/10.1016/S1384-1076\(01\)00041-0](http://dx.doi.org/10.1016/S1384-1076(01)00041-0).
- [104] William A Newcomb. “Hydromagnetic stability of a diffuse linear pinch”. In: *Annals of Physics* 10.2 (1960), pp. 232–267.

- [105] Theodore G Northrop. “The guiding center approximation to charged particle motion”. In: *Annals of Physics* 15.1 (1961), pp. 79–101.
- [106] Oscar Olmedo, Angelos Vourlidis, Jie Zhang, and Xin Cheng. “Secondary Waves and/or the “Reflection” from and “Transmission” through a Coronal Hole of an Extreme Ultraviolet Wave Associated with the 2011 February 15 X2.2 Flare Observed with SDO/AIA and STEREO/EUVI”. In: *The Astrophysical Journal* 756.2 (2012), p. 143. URL: <http://stacks.iop.org/0004-637X/756/i=2/a=143>.
- [107] T Onchi, D McColl, M Dreval, S Wolfe, C Xiao, and A Hirose. “Design and implementation of fast charging circuit for repetitive compact torus injector”. In: *Fusion Engineering and Design* 89.11 (2014), pp. 2559–2565. ISSN: 0920-3796. DOI: <http://doi.org/10.1016/j.fusengdes.2014.06.019>.
- [108] E Oz, C E Myers, M Yamada, Hantao Ji, R M Kulsrud, and J Xie. “Experimental verification of the Kruskal-Shafranov stability limit in line-tied partial-toroidal plasmas”. In: *Physics of Plasmas* 18.10 (2011), p. 102107.
- [109] Eugene N Parker. “Sweet’s mechanism for merging magnetic fields in conducting fluids”. In: *Journal of Geophysical Research* 62.4 (1957), pp. 509–520.
- [110] Spiros Patsourakos and Jean-Claude Vial. “SOHO Contribution to Prominence Science”. In: *Solar Physics* 208.2 (2002), pp. 253–281. ISSN: 1573-093X. DOI: [10.1023/A:1020510120772](http://dx.doi.org/10.1023/A:1020510120772). URL: <http://dx.doi.org/10.1023/A:1020510120772>.
- [111] R Raman, T R Jarboe, B A Nelson, S P Gerhardt, W.-S. Lay, and G J Plunkett. “Design and operation of a fast electromagnetic inductive massive gas injection valve for NSTX-U”. In: *Review of Scientific Instruments* 85.11 (2014), 11E801. DOI: [10.1063/1.4885545](http://dx.doi.org/10.1063/1.4885545). URL: <http://dx.doi.org/10.1063/1.4885545>.
- [112] J W Rayleigh Strutt. “Investigation of the character of the equilibrium of an incompressible heavy fluid of variable density”. In: *Proceedings of the London mathematical society* 14 (1883), pp. 170–177.
- [113] Yang Ren, Masaaki Yamada, Stefan Gerhardt, Hantao Ji, Russell Kulsrud, and Aleksey Kuritsyn. “Experimental verification of the Hall effect during magnetic reconnection in a laboratory plasma”. In: *Physical review letters* 95.5 (2005), p. 55003.
- [114] Marshall N Rosenbluth, R Y Dagazian, and P H Rutherford. “Nonlinear properties of the internal  $m=1$  kink instability in the cylindrical tokamak”. In: *The Physics of Fluids* 16.11 (1973), pp. 1894–1902.
- [115] D M Rust and B J LaBonte. “Observational evidence of the kink instability in solar filament eruptions and sigmoids”. In: *The Astrophysical Journal Letters* 622.1 (2005), p. L69.

- [116] D D Ryutov, R P Drake, and B A Remington. “Criteria for Scaled Laboratory Simulations of Astrophysical MHD Phenomena”. In: *Astrophysical Journal Supplement* 127 (Apr. 2000), pp. 465–468. DOI: [10.1086/313320](https://doi.org/10.1086/313320).
- [117] M Ryutova, T Berger, Z Frank, T Tarbell, et al. “Observation of plasma instabilities in quiescent prominences”. In: *Solar Physics* 267.1 (2010), pp. 75–94.
- [118] K Saito and C L Hyder. “A Concentric Ellipse Multiple-Arch System in the Solar Corona”. In: *Solar Physics* 5 (Sept. 1968), pp. 61–86. DOI: [10.1007/BF00147121](https://doi.org/10.1007/BF00147121).
- [119] Carolus J Schrijver, Guillaume Aulanier, Alan M Title, Etienne Pariat, and Cecile Delannée. “The 2011 February 15 X2 Flare, Ribbons, Coronal Front, and Mass Ejection: Interpreting the Three-dimensional Views from the Solar Dynamics Observatory and STEREO Guided by Magnetohydrodynamic Flux-rope Modeling”. In: *The Astrophysical Journal* 738.2 (2011), p. 167. URL: <http://stacks.iop.org/0004-637X/738/i=2/a=167>.
- [120] Byonghoon Seo and Paul M Bellan. “Experimental investigation of the compression and heating of an MHD-driven jet impacting a target cloud”. In: *Physics of Plasmas* 25.11 (2018), p. 112703.
- [121] Byonghoon Seo, Pakorn Wongwaitayakornkul, Magnus A Haw, Ryan S Marshall, and Paul M Bellan. “Determination of a macro- to micro-scale progression leading to a magnetized plasma disruption”. In: *Physics of Plasmas* 00 (2020), p. 1.
- [122] Kazunari Shibata, Yoshinori Ishido, Loren W Acton, Keith T Strong, Tadashi Hirayama, Yutaka Uchida, Alan H McAllister, Ryoji Matsumoto, Saku Tsuneta, Toshifumi Shimizu, et al. “Observations of X-ray jets with the YOHKOH soft X-ray telescope”. In: *Publications of the Astronomical Society of Japan* 44 (1992), pp. L173–L179.
- [123] U Shumlak, R P Golingo, B A Nelson, and D J Den Hartog. “Evidence of stabilization in the Z-pinch”. In: *Physical review letters* 87.20 (2001), p. 205005.
- [124] James C Simpson, John E Lane, Christopher D Immer, and Robert C Youngquist. “Simple Analytic Expressions for the Magnetic Field of a Circular Current Loop”. In: *NASA technical documents* (2001). URL: <https://ntrs.nasa.gov/archive/nasa/casi.ntrs.nasa.gov/20010038494.pdf>.
- [125] E V Stenson and P M Bellan. “Magnetically Driven Flows in Arched Plasma Structures”. In: *Phys. Rev. Lett.* 109.7 (Aug. 2012), p. 75001. DOI: [10.1103/PhysRevLett.109.075001](https://doi.org/10.1103/PhysRevLett.109.075001).
- [126] Alphonse C Sterling, Ronald L Moore, David A Falconer, and Mitzi Adams. “Small-scale filament eruptions as the driver of X-ray jets in solar coronal holes”. In: *Nature* 523.7561 (2015), pp. 437–440.

- [127] F Suzuki-Vidal, S V Lebedev, M Krishnan, J Skidmore, G F Swadling, M Bocchi, A J Harvey-Thompson, S Patankar, G C Burdiak, P de Grouchy, L Pickworth, S J P Stafford, L Suttle, M Bennett, S N Bland, J P Chittenden, G N Hall, E Khoory, R A Smith, A Ciardi, A Frank, R E Madden, K Wilson-Elliot, and P Coleman. “Interaction of radiatively cooled plasma jets with neutral gases for laboratory astrophysics studies”. In: *High Energy Density Physics* 9.1 (2013), pp. 141–147. ISSN: 1574-1818. DOI: <http://doi.org/10.1016/j.hedp.2012.11.003>.
- [128] Peter A Sweet. “14. The neutral point theory of solar flares”. In: *Symposium-International Astronomical Union*. Vol. 6. Cambridge University Press. 1958, pp. 123–134.
- [129] H Takabe, K Mima, L Montierth, and RL Morse. “Self-consistent growth rate of the Rayleigh–Taylor instability in an ablatively accelerating plasma”. In: *The Physics of fluids* 28.12 (1985), pp. 3676–3682.
- [130] Geoffrey Ingram Taylor. “The instability of liquid surfaces when accelerated in a direction perpendicular to their planes. I”. In: *Proceedings of the Royal Society of London. Series A. Mathematical and Physical Sciences* 201.1065 (1950), pp. 192–196.
- [131] J B Taylor. “Relaxation and magnetic reconnection in plasmas”. In: *Reviews of Modern Physics* 58.3 (1986), p. 741.
- [132] J Tenfelde, P Kempkes, F Mackel, S Ridder, H Stein, T Tacke, and H Soltwisch. “On the relevance of magnetohydrodynamic pumping in solar coronal loop simulation experiments”. In: *Physics of Plasmas* 19.7 (2012), p. 72513.
- [133] J Tenfelde, F Mackel, S Ridder, T Tacke, P Kempkes, and H Soltwisch. “Apex expansion of magnetized plasma loops in a laboratory experiment”. In: *Plasma Physics and Controlled Fusion* 56.5 (2014), p. 55011. URL: <http://stacks.iop.org/0741-3335/56/i=5/a=055011>.
- [134] B J Thompson and D C Myers. “A catalog of coronal “{EIT} wave” transients”. In: *The Astrophysical Journal Supplement Series* 183.2 (2009), p. 225.
- [135] B J Thompson, S P Plunkett, J B Gurman, J S Newmark, O C St Cyr, and DJz Michels. “SOHO/EIT observations of an Earth-directed coronal mass ejection on May 12, 1997”. In: *Geophysical Research Letters* 25.14 (1998), pp. 2465–2468.
- [136] Hui Tian, Peter R Young, Katharine K Reeves, Tongjiang Wang, Patrick Antolin, Bin Chen, and Jiansen He. “Global sausage oscillation of solar flare loops detected by the interface region imaging spectrograph”. In: *The Astrophysical Journal Letters* 823.1 (2016), p. L16.
- [137] M Tokman and P M Bellan. “Three-dimensional model of the structure and evolution of coronal mass ejections”. In: *The Astrophysical Journal* 567.2 (2002), p. 1202. DOI: [10.1086/338699](http://dx.doi.org/10.1086/338699).

- [138] T Török and B Kliem. “The evolution of twisting coronal magnetic flux tubes”. In: *Astronomy and Astrophysics* 406 (Aug. 2003), pp. 1043–1059. DOI: [10.1051/0004-6361:20030692](https://doi.org/10.1051/0004-6361:20030692).
- [139] T Török and Bernhard Kliem. “Confined and ejective eruptions of kink-unstable flux ropes”. In: *The Astrophysical Journal Letters* 630.1 (2005), p. L97.
- [140] S K P Tripathi, P M Bellan, and G S Yun. “Observation of Kinetic Plasma Jets in a Coronal-Loop Simulation Experiment”. In: *Phys. Rev. Lett.* 98.13 (Mar. 2007), p. 135002. DOI: [10.1103/PhysRevLett.98.135002](https://doi.org/10.1103/PhysRevLett.98.135002).
- [141] S K P Tripathi and W Gekelman. “Dynamics of an Erupting Arched Magnetic Flux Rope in a Laboratory Plasma Experiment”. In: *Solar Physics* 286.2 (Sept. 2013), pp. 479–492. ISSN: 1573-093X. DOI: [10.1007/s11207-013-0257-0](https://doi.org/10.1007/s11207-013-0257-0).
- [142] K Vanninathan, A M Veronig, K Dissauer, M S Madjarska, I G Hannah, and E P Kontar. “Coronal Response to an {EUV} Wave from {DEM} Analysis”. In: *The Astrophysical Journal* 812.2 (2015), p. 173. URL: <http://stacks.iop.org/0004-637X/812/i=2/a=173>.
- [143] Astrid M Veronig, Manuela Temmer, and Bojan Vršnak. “High-cadence observations of a global coronal wave by STEREO EUVI”. In: *The Astrophysical Journal Letters* 681.2 (2008), p. L113.
- [144] George C Vlases. “Experiments in a Cylindrical Magnetic Shock Tube”. PhD thesis. Caltech, 1963. URL: <http://resolver.caltech.edu/CaltechTHESIS:10092012-110749746>.
- [145] A Vourlidas, R A Howard, E Esfandiari, S Patsourakos, S Yashiro, and G Michalek. “Comprehensive Analysis of Coronal Mass Ejection Mass and Energy Properties Over a Full Solar Cycle”. In: *The Astrophysical Journal* 722.2 (2010), p. 1522. DOI: [10.1088/0004-637X/722/2/1522](https://doi.org/10.1088/0004-637X/722/2/1522).
- [146] Bojan Vršnak and Edward W Cliver. “Origin of coronal shock waves”. In: *Solar Physics* 253.1-2 (2008), p. 215.
- [147] Bojan Vršnak and Slaven Lulić. “Formation of coronal MHD shock waves—I. The basic mechanism”. In: *Solar Physics* 196.1 (2000), pp. 157–180.
- [148] M Waldmeier. “The Structure of the Monochromatic Corona in the Surroundings of Prominences”. In: *Solar Physics* 15 (Nov. 1970), pp. 167–175. DOI: [10.1007/BF00149483](https://doi.org/10.1007/BF00149483).
- [149] A Warmuth, G Mann, and H Aurass. “First soft X-ray observations of global coronal waves with the GOES Solar X-ray Imager”. In: *The Astrophysical Journal Letters* 626.2 (2005), p. L121.
- [150] David F Webb and Timothy A Howard. “Coronal Mass Ejections: Observations”. In: *Living Reviews in Solar Physics* 9.1 (June 2012), p. 3. ISSN: 1614-4961. DOI: [10.12942/lrsp-2012-3](https://doi.org/10.12942/lrsp-2012-3).

- [151] Thomas Wiegmann and Takashi Sakurai. “Solar Force-free Magnetic Fields”. In: *Living Reviews in Solar Physics* 9.1 (2012), p. 5. DOI: [10.12942/lrsp-2012-5](https://doi.org/10.12942/lrsp-2012-5).
- [152] Mark L Wilkins. “Use of artificial viscosity in multidimensional fluid dynamic calculations”. In: *Journal of computational physics* 36.3 (1980), pp. 281–303.
- [153] M J Wills-Davey, C E DeForest, and J O Stenflo. “Are “EIT Waves” Fast-Mode MHD Waves?” In: *The Astrophysical Journal* 664.1 (2007), p. 556. URL: <http://stacks.iop.org/0004-637X/664/i=1/a=556>.
- [154] M J Wills-Davey and B J Thompson. “Observations of a propagating disturbance in {TRACE}”. In: *Solar Physics* 190.1-2 (1999), pp. 467–483.
- [155] M. J. Wills-Davey and G. D. R. Attrill. “EIT Waves: A Changing Understanding over a Solar Cycle”. In: *Space Science Reviews* 149 (Dec. 2009), pp. 325–353. DOI: [10.1007/s11214-009-9612-8](https://doi.org/10.1007/s11214-009-9612-8).
- [156] K L Wong, Ming-Sheng Chu, T C Luce, C C Petty, P A Politzer, R Prater, L Chen, R W Harvey, Max E Austin, L C Johnson, et al. “Internal kink instability during off-axis electron cyclotron current drive in the DIII-D tokamak”. In: *Physical review letters* 85.5 (2000), p. 996.
- [157] Pakorn Wongwaitayakornkul, Magnus A Haw, Hui Li, Shengtai Li, and Paul M Bellan. “Apex Dips of Experimental Flux Ropes: Helix or Cusp?” In: *The Astrophysical Journal* 848.2 (2017), p. 89. DOI: <https://doi.org/10.3847/1538-4357/aa8990>.
- [158] Pakorn Wongwaitayakornkul, Magnus A Haw, Hui Li, Shengtai Li, and Paul M Bellan. “Apex Dips of Experimental Flux Ropes: Helix or Cusp?” In: *The Astrophysical Journal* 848.2 (2017), p. 89.
- [159] Masaaki Yamada, Russell Kulsrud, and Hantao Ji. “Magnetic reconnection”. In: *Reviews of Modern Physics* 82.1 (2010), p. 603.
- [160] Jimmy Yee. “Experimental investigations in spheromaks: injection into a tokamak and formation in an unbounded environment”. PhD thesis. Caltech, 1999.
- [161] Setthivoine You, G S Yun, and P M Bellan. “Dynamic and stagnating plasma flow leading to magnetic-flux-tube collimation”. In: *Physical review letters* 95.4 (2005), p. 45002.
- [162] David L Youngs. “Three-dimensional numerical simulation of turbulent mixing by Rayleigh–Taylor instability”. In: *Physics of Fluids A: Fluid Dynamics* 3.1-3 (1984), pp. 1312–1320.
- [163] David L Youngs. “Three-dimensional numerical simulation of turbulent mixing by Rayleigh–Taylor instability”. In: *Physics of Fluids A: Fluid Dynamics* 3.5 (1991), pp. 1312–1320.

- [164] Gunsu S Yun and Paul M Bellan. “Plasma tubes becoming collimated as a result of magnetohydrodynamic pumping”. In: *Physics of Plasmas* 17.6 (2010), p. 62108.
- [165] Gunsu Soonshin Yun. “Dynamics of plasma structures interacting with external and self-generated magnetic fields”. PhD thesis. California Institute of Technology, 2008. URL: <http://resolver.caltech.edu/CaltechETD:etd-07242007-162442>.
- [166] Xiang Zhai and Paul M Bellan. “A hybrid Rayleigh-Taylor-current-driven coupled instability in a magnetohydrodynamically collimated cylindrical plasma with lateral gravity”. In: *Physics of Plasmas* 23.3 (2016), p. 32121.
- [167] Xiang Zhai, Hui Li, Paul M Bellan, and Shengtai Li. “Three-dimensional {MHD} simulation of the Caltech plasma jet experiment: first results”. In: *The Astrophysical Journal* 791.1 (2014), p. 40. DOI: [10.1088/0004-637X/791/1/40](https://doi.org/10.1088/0004-637X/791/1/40).
- [168] Yang Zhang, Pakorn Wongwaitayakornkul, and Paul M Bellan. “Magnetic Rayleigh-Taylor Instability in an Experiment Simulating a Solar Loop”. In: *The Astrophysical Journal Letters* 889.2 (2020), p. L32. DOI: <https://doi.org/10.3847/2041-8213/ab6b2d>.
- [169] Yang Zhang, Pakorn Wongwaitayakornkul, and Paul M Bellan. “Magnetic Rayleigh-Taylor Instability in an Experiment Simulating a Solar Loop”. In: *The Astrophysical Journal Letters* 889.2 (2020), p. L32.
- [170] Andrei N Zhukov. “EIT wave observations and modeling in the STEREO era”. In: *Journal of Atmospheric and Solar-Terrestrial Physics* 73.10 (2011), pp. 1096–1116.
- [171] Tomislav Žic, Bojan Vršnak, Manuela Temmer, and Carla Jacobs. “Cylindrical and spherical pistons as drivers of MHD shocks”. In: *Solar physics* 253.1-2 (2008), pp. 237–247.

## *Appendix A*

### ADDITIONAL MATERIAL ON DIPS ON FLUX ROPE

Let (A|B) denote a situation with injected gas ‘A’ and prefilled gas ‘B’. In addition to the (Ar|H) case shown in Figure 2.3 <sup>1</sup>, the experiment could be conducted using different sets of gas. A choice of gas type affects the shape of the flux rope as demonstrated in Figure A.1.

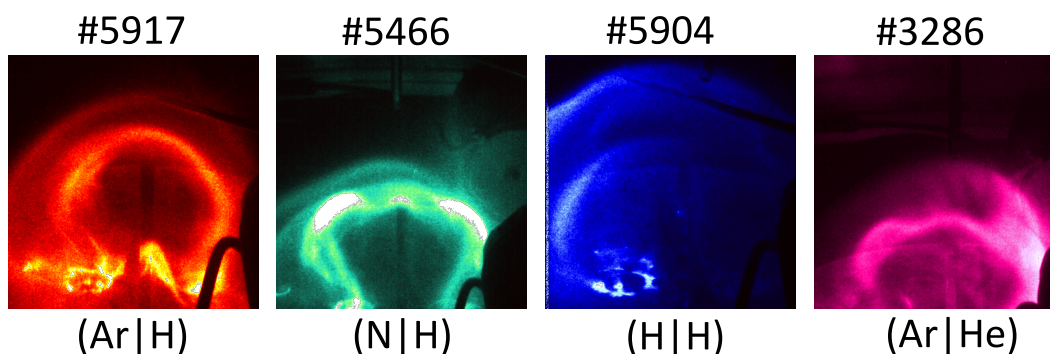


Figure A.1: Shapes of the flux rope with the initially prefilled neutral gas of various types.

The shape depends on the neutral gas interaction (collisional cross-section), a phenomenon described in Chapter 4. The only difference here is that an injected neutral gas interacts with a prefilled neutral, as oppose to a injected gas from the other footpoint. Therefore, a dip location is not necessarily at the top of a flux rope. This effect is illustrated in Figure A.2; locations of a dip shift as we change an amount of gas injection.

Consequently, we can use this technique to create customizable flux ropes with dips at various location. An extra nozzle could be added to generate a localized density pileup. Figure A.3 shows three classes of flux rope with 0, 1, and 2 dips.

<sup>1</sup>#5917 of (Ar|H) has lower hydrogen input and hence looks different than Figure 2.3

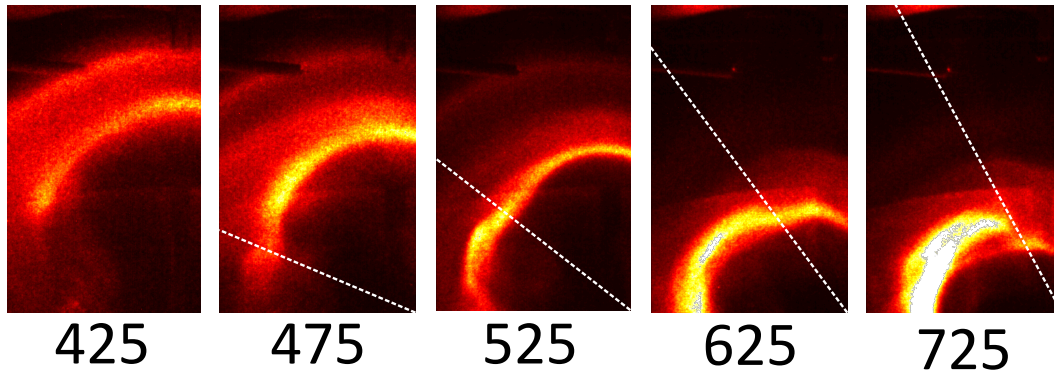


Figure A.2: Images show different shots of (Ar|H) plasma with varying gas injection from the footpoints (#3749-3753). As a result, a dip location on the flux rope is differed. The labels are fast-gas-valve voltages, corresponding to amounts of argon gas injection from the footpoints. White dashed lines indicate the locations of the dip.

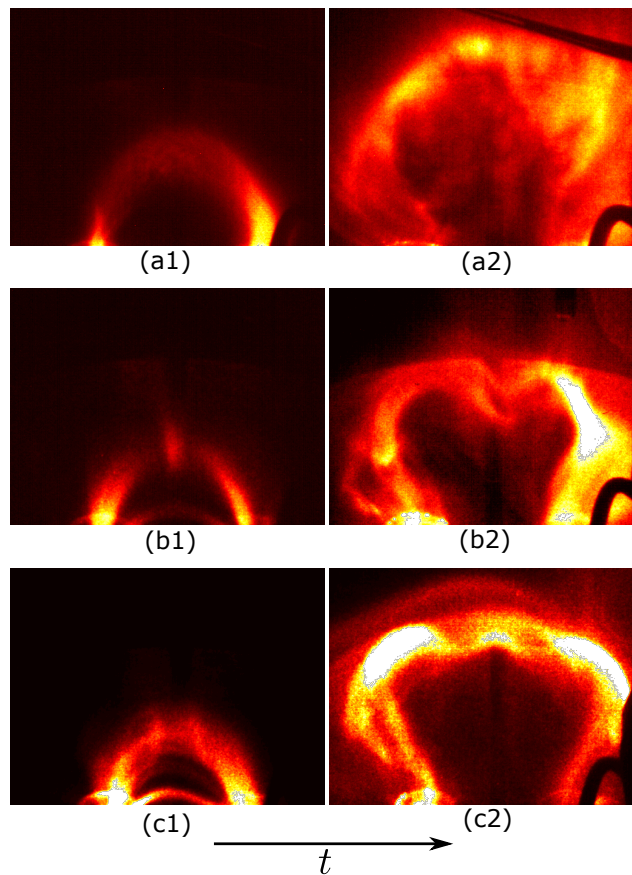


Figure A.3: Time sequences of illuminated neutral pileups and their corresponding flux rope with various number of dipoles: (a) 0, (b) 1, and (c) 2.

*Appendix B*

### ADDITIONAL MATERIAL ON DIAMAGNETIC CAVITY

The strapping coils, described in Ref. [46], are installed to test the effect of strapping magnetic field on the cavity size. The coils are located off-axis with 10 cm offset in the  $y$ -direction. Figure B.1 shows the fast camera images of the cavity with maximum strapping fields  $B_s = 0$  G, 375 G, and 750 G. From Eq. 5.10, the equilibrium cavity size is  $b_{eq} = \mu_0 I / (2\pi B_0 \sqrt{1 + \beta})$ ; a stronger background field results in a smaller cavity size, as depicted in Figure B.1.

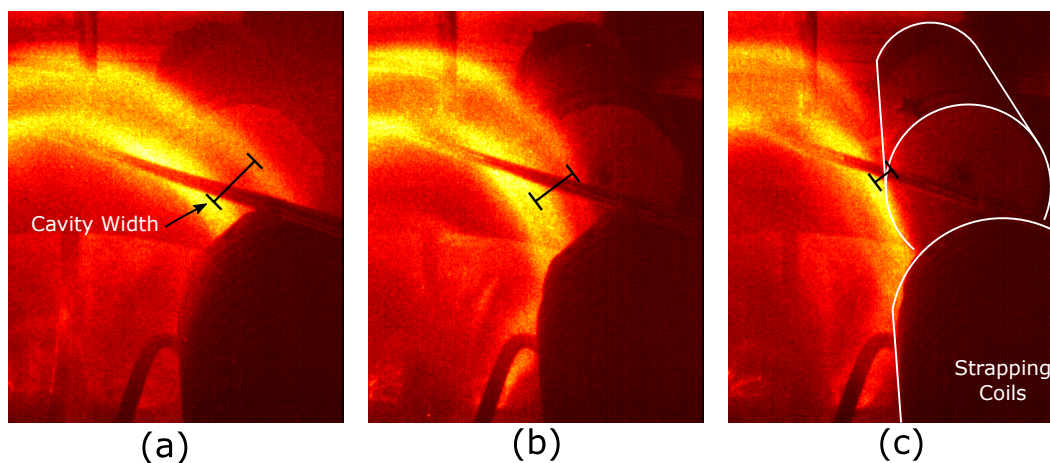


Figure B.1: False color images of three cases with different strength of the strapping fields at  $t = 10.5 \mu s$  after the breakdown: (a)  $B_s = 0$  G, (b)  $B_s = 375$  G, and (c)  $B_s = 750$  G. The cavity widths are labelled with black lines and the strapping coils are contoured with white lines